UNIVERSITAT POLITÈCNICA DE CATALUNYA BARCELONATECH

Analysis of energetic particle-driven Alfvénic instabilities in tokamak and stellarator plasmas using three dimensional numerical tools

Allah Rakha

International Doctoral College in Fusion Science and Engineering

Analysis of energetic particle-driven Alfvénic instabilities in tokamak and stellarator plasmas using three dimensional numerical tools

Allah Rakha (PhD student)

Thesis Supervisors

Prof. Mervi J. Mantsinen (BSC-CNS)

Prof. Jean-Marie Noterdaeme (UGhent)

Thesis Tutor

Prof. Lluís Batet Miracle

Doctoral Program in Nuclear and Ionizing Radiation Engineering (Universitat Politècnica de Catalunya), Department of Physics - Advanced Nuclear Technologies Research Group.

Doctorate in Engineering Physics and Joint International Doctoral College in Fusion Science and Engineering (FUSION-DC), Department of Applied Physics (Ghent University Belgium).

Analysis of energetic particle-driven Alfvénic instabilities in tokamak and stellarator plasmas using three dimensional numerical tools

Allah Rakha (PhD student)

Thesis Supervisors

Prof. Mervi J. Mantsinen (BSC-CNS)

Prof. Jean-Marie Noterdaeme (UGhent)

Thesis Tutor

Prof. Lluís Batet Miracle

Doctoral Program in Nuclear and Ionizing Radiation Engineering (Universitat Politècnica de Catalunya), Department of Physics - Advanced Nuclear Technologies Research Group.

Doctorate in Engineering Physics and Joint International Doctoral College in Fusion Science and Engineering (FUSION-DC), Department of Applied Physics (Ghent University Belgium).

September 2019

I dedicate this PhD work to my parents whose continuous support and hard struggles are always with me.

Declaration

I hereby declare that except where specific reference is made to the work of others, the contents of this dissertation are original and have not been submitted in whole or in part for consideration for any other degree or qualification in this, or any other university. This dissertation is my own work and contains nothing which is the outcome of work done in collaboration with others, except as specified in the text and Acknowledgements.

Allah Rakha
August 2019

Acknowledgements

All praises and thanks are due to ALLAH Almighty, the most merciful and the most beneficent, who enabled me to accomplish this endeavour successfully. All respects and honours for the beloved Holy Prophet MUHAMMAD (Peace Be Upon Him) who urged the importance of education for the human being and forever is the torch of knowledge and guidance for humanity. I wish to express my deepest obligations to my parents and my family for their sacrifices during the pursuance of my dream of higher education. It is indeed prayers of my parents, brothers, wife and friends that I could complete this work. Particularly I am very much obliged for the support of my mother who stood up with me in all circumstances and encouraged me with her kind words, which always wisher in my ears 'You will come back with victory'.

I am highly indebted to my supervisor Prof. Mervi J. Mantsinen for introducing me to this interesting field of research. It has been an honour for me to be her PhD student. Her immense guidance, tireless passion, remarkable suggestions, didactic encouragement, friendly discussion and continuous motivation helped me in all the time of research and writing of this thesis. I do appreciate her phenomenal patience for going through several drafts of my thesis to make my PhD experience productive and stimulating. It is hard to overstate my esteem for her, except that this journey would have been impossible without her.

My cordial gratitude is reserved for the scientists Dr. Donald A. Spong from Oak Ridge National Laboratory (ORNL) and Dr. Sergei Sharapov from Culham Center for Fusion Energy (CCFE), Oxfordshire, UK who provided their computational tools/ codes and actively trained me in mastering them. Especially their trips to Barcelona for hands-on and active training sessions are really admiring. Their couching, invaluable comments and insightful suggestions to helped to widen my research from various perspectives. I really appreciate their intoxicating optimism and social behaviour in conducting these sessions. I remain amazed that despite their busy schedule, they remained available for my questions and reading my journal articles with crucial feedback. They are an inspiration and I am pleased to be their student.

It is imperative to thank Dr. Alexander V. Melnikov from National Research Center 'Kurchatov Institute', Moscow, Russia who helped me understanding this field of research and suggested experimental results for their modelling from TJ-II stellarator plasmas. His support for reading our research articles and providing critical feedback really helped to enhance my understanding in this field of research. It is really important to thank my collaborators Dr. Francisco Castejón and Dr. Antonio López-Fraguas from Fusion National Laboratory (CIEMAT) Madrid, Spain who maintained our collaboration and provided TJ-II experimental data for the modelling of AEs. I am especially thankful to Dr. Antonio López-Fraguas for helping me to master equilibrium reconstruction VMEC code for the 3D toroidal devices. His continuous support through lengthy emails remained always a source of an aspiration and encouragement to diversify my expertise.

Sincere thanks to my Co-Supervisor Prof. Jean-Marie Noterdaeme from Ghent University Belgium, whose efforts helped me to become an active part of the European fusion community through an Erasmus Joint Doctoral Programme, International Doctoral College in Fusion Science and Engineering (FUSION-DC), which is a double doctorate (Cotutelle) between Ghent University, Belgium and Universitat Politécnica de Catalunya, BarcelonaTech (UPC). I am also very much in debt to Dr. Philipp Lauber from Max Planck Institute for Plasma Physics (IPP) Garching, Germany who led me in the field of helical core research for the Asdex-Upgrade (AUG) tokamak during my Erasmus mobility secondment at IPP under the supervision of Prof. Jean-Marie Noterdaeme. I am very much obliged to Dr. Lauber for his memorable enthusiastic support, numerous creative interpretations, and interesting discussions that gave me the impetus to go further during the gruelling work days.

A special mention and gratitude is due for my tutor Prof. Lluís Batet Miracle from UPC, who helped me in the administration of doctoral admission and enrolment and thesis progression. I am very much obliged for his support, guidance and active administration of the UPC requirements for my doctoral thesis.

I am very grateful to all my colleagues at Barcelona Supercomputing Center (BSC) for providing a welcoming stimulating atmosphere. A special mention and gratitude is due for Dr. Xavier Saez Pous and Dr. Albert Gutiérrez for their gracious assistance in installing my codes at Marenostrum supercomputer and helping me to understand the efficient usage of these supercomputing tools. The occasional chats with my fellow Mr. Daniel Gallart Escola PhD student have always been most enjoyable. This group has been a source of friendships as well as good advice and collaboration. All the "BSC-Fusion" members of the group have contributed immensely to my personal and

professional time at Barcelona. Special thanks also goes to Dr. Shimpei Futatani an alumni of our group for the scientific discussions during the initial years of PhD. I also gratefully acknowledge financial support from AGAUR FI predoctoral grant, EUROfusion, and Severo Ochoa Mobility Grant as the funding sources that made my PhD work possible.

I seize this opportunity to also acknowledge and thank my colleagues, friends and seniors back in Pakistan, for contributing to my growth, inspiring me and providing me with invaluable experiences. I am also very much thankful to my Erasmus colleagues, teachers and friends who helped me in believing that a research work of eminence in the field of Magnetic Confinement Fusion (MCF) is a necessary step to meet the future energy needs of this planet. They encouraged me to apply for this PhD program and make an innovative contribution by exploring the physics and engineering challenges in MCF research and development. Special thanks goes to Erasmus program coordinators: Dr. Jose Ramon Martin Solis (UC3M) and Dr. Kieran J. Mc-Carthy (CIEMAT), and Dr. Carsten Lechte (IGVP-Stuttgart).

Last but by no means the least, I would like to pay special thanks to my family members for all their love and encouragement. I wish to express my deepest obligations to my parents for their sacrifices during the pursuance of my education. It is indeed their prayers and well wishes that supported me in all my pursuits. Their encouragement and inspirations have always been with me. I am profoundly grateful to my all brothers who always pray for my success. Special thanks to my brother Mr. Allah Ditta Javed who carried out some of my domestic responsibilities in my absence. And most of all to my lovely bunnies Abdullah Ahmed, Muhammad Bilal Raza and my little prince Muhammad Mustafa Badar, for being my strength and my biggest motivation. Many heart filled thanks to my sincere and caring better half whose faithful support during the final stages of my PhD is so appreciated. I am truly fortunate to have you in my life. I owe it all to your wholehearted prayers and unconditional sacrifices. Thank you for all your patience, trust and confidence in me.

After all these, I wish to express my sincere appreciation to those who have academically, financially, psychologically and emotionally contributed to this work and supported me in one way or the other during this amazing journey.

Abstract

Shear Alfvén instabilities are of the considerable interest in fusion plasma confinement and in future burning plasmas. Mostly, these instabilities are driven by the energetic particles (EPs) in fusion plasmas. Alfvénic instabilities can degrade EPs confinement, heating efficiency by channelizing them, and the ignition margin. They can also cause severe damages to the plasma-facing components (PFCs) through high heat fluxes. Thus the investigations for their control, better performance and comprehensive understanding are of the primary importance in burning plasmas. In this dissertation, a detailed analysis of the experientially observed energetic particle-driven Alfvénic instabilities in tokamak and stellarator plasmas using three dimensional numerical tools based on the reduced MHD model has been carried out. To explain experimental observations of Alfvén modes in TJ-II flexible heliac plasmas, we have compared experimental results with the results obtained through theoretical model of shear Alfvén waves in 3D toroidal geometry. Bifurcated MHD equilibria with 3D helical core surrounded by an axisymmetric 2D mantle has been modelled for the ASDEX-Upgrade (AUG) tokamak plasmas having safety factor around unity in the core region. Modelling of effect of the formation of 3D helical core on Alfvén continuum structures in tokamak plasmas shows continuum splitting and shifting around the frequency accumulation point and the formation of additional frequency gaps.

The investigations presented in this thesis are divided into two parts. In the first part for stellarator plasmas, modelling results for the steady and chirping states Alfvén eigenmodes (AEs) together with the reversed-shear AEs are presented. Additionally, wave particle interaction (WPI) studies are also developed using Monte Carlo transport model based on the 3D equilibria for the TJ-II plasmas. The coexistence of chirping and steady state modes has been assessed on the persistent appearance of the corresponding combination of the toroidal (n) and poloidal (m) mode numbers through the rotational transform sensitivity analysis both in iota lowering and iota rising TJ-II dynamic plasmas. Frequency sweeping phenomenon of the Alfvén modes is modelled using normal and non-monotonic (NM) iota profiles with radially extended low-shear and radially localized strong-shear regions. Simulation results obtained with NM iota

profile are in agreement with the experimentally found frequency sweeping modes by covering a wide range of frequency from 115 to 295 kHz as compared with the normal iota profile for which the modes are centred around 150 kHz. In addition, the modes obtained using strong-shear NM iota profile also cover a wide frequency range starting from more lower values from 36 to 216 kHz. In strong-shear NM iota profile, the persistence of a mode on the variation in ι_{min} with the decrease of its radial width not only increase its own stability but also serves as stable mode through which an iota profile could be extracted using MHD spectroscopy principle. In the WPI calculations the corresponding wave-particle resonance function suggest for low bounce harmonics (p) the possibility of describing the non-linear evolution of the AEs in TJ-II by a sum of two ion populations with different weighting factors, one of which is dominated by drag and the other by diffusion. As the bounce harmonic increases, the resonance region begins to expand and can cover a substantial area of the particle phase space. When the bounce harmonics are further increased, this resonance region moves in the direction of higher energy and pitch angle. This reduces the resonance range in the low energy range of the phase space and further leads to its complete disappearance there. Furthermore the 3D drift orbits have also been calculated for the both drag and diffusion regions of the resonance function, which are qualitatively identical.

In the second part of the dissertation, for the tokamak plasmas a bifurcated MHD equilibrium is reconstructed with formation of 3D helical core as saturated magnetic axis and the remaining torus with an axisymmetric equilibrium. The formation of helical core is associated with the 3D equilibrium in the tokamak 2D fusion device. In the equilibrium calculations we find that the helically distorted MHD equilibria may exist even for the axisymmetric devices if q = 1 rational surfaces are present. The continuum calculations with the bifurcated equilibria lead to the frequency splitting via coupling to adjacent n-1 continuum around an accumulation point. Our modelling including 3D effects correctly reproduces the phenomenon of continuum frequency splitting and provides a possible solution for the differences of few kHz in frequency splitting, which remained unexplained with the 2D kinetic calculations. The pressure scaling confirms the increase of helical excursion of the magnetic axis in equilibrium reconstruction and hence the range of continuum frequency splitting. The existence of low-frequency continua and its splitting around the frequency accumulation point are in agreement with the experimental observations for the low-frequency modes.

This dissertation provides an extensive comparison of the experimental and modelling results for the TJ-II stellarator plasmas along with the effect of the formation of bifurcated MHD equilibria on Alfvén continua in AUG tokamak plasmas. We hope

these findings will contribute to improve the understanding of operational regimes of the 3D toroidal fusion systems in the future burning plasmas.

Abstract

Las inestabilidades de cizallamiento de Alfvén son de considerable interés para el confinamiento de plasmas de fusión y para la combustión de futuros plasmas. En su mayoría, estas inestabilidades son producidas por las partículas energéticas (EP) en los plasmas de fusión. Las inestabilidades de Alfvé pueden degradar el confinamiento de las EP, la eficiencia del calentamiento y el margen de ignición. También pueden causar daños graves a los componentes en contacto con el plasma (PFC) a través de altos flujos de calor. Por lo tanto, las investigaciones para su control, mejor rendimiento y conocimiento son de importancia primordial en la combustión de plasmas. En esta disertación, se llevó a cabo un análisis detallado de las inestabilidades de Alfvén observadas experimentalmente en los plasmas tanto en tokamaks como stellarators utilizando herramientas numéricas 3D basadas en el modelo de MHD reducido. Para explicar las observaciones experimentales de los modos Alfvénicos en plasmas helicoidales flexibles de TJ-II, hemos comparado los resultados experimentales con los resultados obtenidos a través del modelo teórico de ondas de cizallamiento de Alfvén en geometría toroidal 3D. Los equilibrios bifurcados MHD con núcleo helicoidal 3D rodeado por un manto 2D axisimétrico se han modelado para los plasmas del tokamak ASDEX-Upgrade (AUG) que tienen un factor de seguridad alrededor de la unidad en la región central. El modelado del efecto de la formación de núcleo helicoidal 3D en estructuras continuas de Alfvén en plasmas de tokamak muestra la división y el desplazamiento continuos alrededor del punto de acumulación de frecuencia y la formación de espacios de frecuencia adicionales. La investigación presentada en esta tesis se divide en dos partes. En la primera parte para los plasmas de stellarators, se presentan los resultados de modelado para los estados estables y chirping de los Alfvén eigenmodes (AEs) junto con los AEs de cizallamiento invertido. Además, los estudios de interacción onda partícula (WPI) también se desarrollan utilizando el modelo de transporte Monte Carlo basado en los equilibrios 3D para los plasmas de TJ-II. La coexistencia de los modos de chirping y estado estacionario se ha evaluado en la apariencia persistente de la combinación correspondiente de los números de modo toroidal (n) y poloidal (m) a través del análisis de sensibilidad de transformación rotacional tanto en plasmas dinámicos de TJ-II de

disminución de iota como de aumento de iota . El fenómeno de barrido de frecuencia de los modos Alfvénicos se modelan utilizando perfiles iota normales y no monotónicos (NM) con regiones de baja cizalladura radialmente extendidas y de cizalladura fuerte localizadas radialmente. Los resultados de la simulación obtenidos con el perfil de iota NM están de acuerdo con los modos de barrido de frecuencia encontrados experimentalmente al cubrir un amplio rango de frecuencia de 115 a 295 kHz en comparación con el perfil de iota normal para el cual los modos se centran alrededor de 150 kHz. Además, los modos obtenidos usando el perfil de iota NM de fuerte cizalladura también cubren un amplio rango de frecuencia a partir de valores más bajos de 36 a 216 kHz. En el perfil de iota NM de cizallamiento fuerte, la persistencia de un modo en la variación de $iota_{min}$ con la disminución de su ancho radial no solo aumenta su propia estabilidad sino que también sirve como un modo estable a través del cual un perfil de iota podría ser extraído utilizando el principio de espectroscopía de MHD. En los cálculos de WPI, la función de resonancia de onda-partícula correspondiente sugiere para armónicos de bajo rebote (p) la posibilidad de describir la evolución no lineal de los EA en TJ-II por una suma de dos poblaciones de iones con diferentes factores de ponderación, uno de los cuales está dominado por la resistencia y el otro por la difusión. A medida que aumenta el armónico de rebote, la región de resonancia comienza a expandirse y puede cubrir un área sustancial del espacio de fase de partículas. Cuando los armónicos de rebote se incrementan aún más, esta región de resonancia se mueve en la dirección de mayor energía y ángulo de inclinación. Esto reduce el rango de resonancia en el rango de baja energía del espacio de fase y conduce a su completa desaparición allí. Además, las órbitas de deriva 3D también se han calculado para las regiones de arrastre y difusión de la función de resonancia, que son, cualitativamente, idénticas.

En la segunda parte de la disertación, para los plasmas de tokamak se reconstruye un equilibrio MHD bifurcado con la formación de un núcleo helicoidal 3D como eje magnético saturado y el toro restante con un equilibrio axisimétrico. La formación de núcleo helicoidal está asociada con el equilibrio 3D en el dispositivo de fusión de tokamak 2D. En los cálculos de equilibrio encontramos que los equilibrios MHD distorsionados helicoidalmente pueden existir incluso para los dispositivos axisimétricos si q = 1 están presentes superficies racionales. Los cálculos continuos con los equilibrios bifurcados conducen a la división de frecuencia mediante el acoplamiento al continuo n-1 adyacente alrededor de un punto de acumulación. Nuestro modelado que incluye efectos 3D reproduce correctamente el fenómeno de división continua de frecuencia y proporciona una posible solución para las diferencias de pocos kHz en la división de frecuencia, que permaneció sin explicación con los cálculos cinéticos 2D. La escala

de presión confirma el aumento de la excursión helicoidal del eje magnético en la reconstrucción de equilibrio y, por lo tanto, el rango de división de frecuencia continua. La existencia de continuas de baja frecuencia y su división alrededor del punto de acumulación de frecuencia están de acuerdo con las observaciones experimentales para los modos de baja frecuencia. Esta disertación proporciona una comparación exhaustiva de los resultados experimentales y de modelado para los plasmas de stellarator del TJ-II junto con el efecto de la formación de equilibrios bifurcados de MHD en Alfvén continuos en plasmas de tokamak de AUG. Esperamos que estos hallazgos contribuyan a mejorar la comprensión de los regímenes operativos de los sistemas de fusión toroidal 3D en los futuros plasmas de combustión.

Abstract

Afschuif (shear) Alfvén-instabiliteiten zijn van groot belang voor de opsluiting van plasma's in het fusieonderzoek en voor toekomstige brandende plasma's. Meestal worden in deze plasma's, dit type instabiliteiten aangedreven door de energetische deeltjes (EP's). Alfvénic instabiliteiten kunnen de opsluiting van EP's verslechteren door hun verliezen te kanaliseren en bijgevolg de verwarmingsefficiëntie en de ontstekingsmarge reduceren. Ze kunnen ook ernstige schade aan de plasma-gerichte componenten (PFC's) veroorzaken door de resulterende lokale hoge warmtefluxen.

Daarom is het onderzoek naar hun controle voor het bereiken van betere prestaties en in het algemeen een beter begrip van deze instabiliteiten van primair belang voor brandende plasma's. In dit proefschrift is een gedetailleerde analyse gemaakt van de experimenteel waargenomen Alfvéic instabiliteiten aangedreven door energetische deeltjes in stellarator- en tokamakplasma's.

Dit gebeurde met behulp van driedimensionale numerieke hulpmiddelen gebaseerd op het gereduceerde MHD-model. Om experimentele waarnemingen van Alfvén-modi in TJ-II flexibele heliac (stellarator type) plasma's te verklaren, hebben we experimentele resultaten vergeleken met de resultaten die verkregen werden via een theoretisch model van shear Alfvén-golven in 3D toroïdale geometrie. Vertakte (bifurcated) MHD-evenwichten met een 3D-spiraalvormige kern omgeven door een asymmetrische 2D-mantel werd gemodelleerd voor ASDEX Upgrade (AUG) tokamak-plasma's, waarbij de veiligheidsfactor in het kerngebied ongeveer één was. Modellering van het effect van de vorming van een 3D-schroefkern op Alfvén continuümstructuren in tokamak-plasma's toont het opsplitsen en verschuiven van het continuüm rond het frequentieaccumulatiepunt en de vorming van extra openingen in het frequentiespectrum.

Het onderzoek in dit proefschrift is opgedeeld in twee delen.

In het eerste deel worden voor stellarator-plasma's, de modelleringsresultaten voor Alfvén eigenmodes (AE's) van het stabiele (steady-state) en tjilpende (chirping) type gepresenteerd, samen met de omgekeerde-shear AE's. Bovendien worden ook studies van golfdeeltjesinteractie (WPI-wave particle interaction) ontwikkeld met behulp van het Monte Carlo-transportmodel op basis van de 3D-evenwichten voor de TJ-

II-plasma's. De co-existentie van tjilpende en steady-state modi werd vastgesteld op basis van het aanhoudend voorkomen van de overeenkomstige combinatie van de toroïdale (n) en poloidale (m) mode nummers. Deze vaststelling gebeurde via de rotatie-transformatiegevoeligheidsanalyse, zowel in iota-verlagende als iota-verhogende TJ-II dynamische plasma's. Het fenomeen van de variatie/veging van de frequentie (frequency sweeping) van de Alfvén-modi werd gemodelleerd met behulp van normale en niet-monotone (NM) iota-profielen met radiaal uitgebreide regio's van lage afschuiving (low-shear) en radiaal gelokaliseerde regio's van sterke afschuiving (high-shear). Resultaten van de simulaties verkregen met een NM iota-profiel zijn in overeenstemming met de experimenteel gevonden modi met een vegende frequentie die een breed frequentiebereik van 115 tot 295 kHz afdekken in vergelijking met het normale iota-profiel waarvoor de modi gecentreerd zijn rond 150 kHz. Bovendien dekken de modi die zijn verkregen met behulp van een NM iota-profiel met sterke afschuiving (high-shear) ook een breed frequentiebereik eerder vanaf lagere waarden van 36 tot 216 kHz. Tijdens een variatie in ι_{min} van een NM iota-profiel met sterke afschuiving (high-shear) blijft een bepaalde mode aanhouden. De afname van de radiale breedte van deze mode verhoogt de eigen stabiliteit. Op basis van deze stabiele mode kan ook een iota-profiel worden geëxtraheerd met behulp van het MHD-spectroscopie principe. In de berekeningen van de golfdeeltjesinteractie (WPI-wave particle interaction) suggereert de overeenkomstige golfdeeltjesresonantiefunctie voor lage bounce-harmonischen (p) de mogelijkheid om de niet-lineaire evolutie van de AE's in TJ-II te beschrijven door een som van twee ionenpopulaties met verschillende wegingsfactoren, één waarvan wordt gedomineerd door de sleep (drag) en de andere door diffusie. Naarmate de bounce-harmonische toeneemt, begint het resonantiegebied uit te zetten en kan het een aanzienlijk gebied van de deeltjesfaseruimte bedekken totdat dit resonantiegebied bij hoge bounce-harmonischen verdwijnt. Verder zijn de 3D-driftbanen ook berekend voor de beide sleep- en diffusiegebieden van de resonantiefunctie, die kwalitatief identiek zijn.

In het tweede deel van het proefschrift wordt voor de tokamak-plasma's een vertakt MHD-evenwicht gereconstrueerd met de vorming van een 3D-spiraalvormige kern als verzadigde magnetische as en de resterende torus met een asymmetrisch evenwicht. De vorming van een spiraalvormige kern wordt geassocieerd met het 3D-evenwicht in het tokamak 2D-fusie-apparaat. In de evenwichtsberekeningen vinden we dat de schroefvormig vervormde MHD-evenwichten kunnen bestaan, zelfs voor de asymmetrische apparaten als er q = 1 rationale oppervlakken aanwezig zijn. De continuümberekeningen met de vertakte evenwichten leiden tot de frequentiesplitsing via koppeling met

een aangrenzend n-1 continuüm rond een accumulatiepunt. Onze modellering inclusief 3D-effecten reproduceert correct het fenomeen frequentiesplitsing van het continuüm en biedt een mogelijke oplossing voor de verschillen van enkele kHz in de splitsing in frequentie, die bij de 2D kinetische berekeningen onverklaard bleven. De scalering met de druk bevestigt de toename van de schroefvormige uitslag van de magnetische as bij evenwichtsreconstructie en daarmee het bereik van continuumfrequentiesplitsing. Het bestaan van laagfrequente continua en de splitsing ervan rond het frequentieaccumulatiepunt zijn in overeenstemming met de experimentele waarnemingen voor de laagfrequentiemodi.

Dit proefschrift biedt een uitgebreide vergelijking van de experimentele en modelleringsresultaten voor de TJ-II stellarator plasma's, samen met het effect van de vorming van vertakte MHD-evenwichten op Alfvén continua in AUG tokamak-plasma's. We hopen dat deze bevindingen zullen bijdragen tot een beter begrip van de operationele regimes van de 3D torusvormige fusiesystemen in de toekomstige brandende plasma's. Het zal helpen om een beter begrip te ontwikkelen van de afschuif (shear) Alfvén-instabiliteiten in 3D-fusiesystemen.

Table of contents

List of figures

List of tables

Chapter 1

Introduction

This chapter provides a brief introduction to thermonuclear fusion and prominent plasma confinement schemes. After that, motivations of this research work are provided to highlight the importance and key issues of plasma confinement in the current 3D fusion devices. Later this chapter also lists the research contributions and entails the published work in peer reviews journals and work presented in leading conferences. Finally it provides the thesis layout which describes the brief contents of the following chapters.

1.1 Thermonuclear fusion

Thermonuclear fusion is process which produces enormous amount of the energy after fusing light nuclei such as hydrogen isotopes. In nature this process works well in stars and illuminate them for hundreds of years in a sustained manner. This process produces energy with the difference of mass of fusion products from the fusing nuclei as described by famous Einstein's energy Equation (1.1). The prominent fusion reaction is between the hydrogen isotopes Deuterium (D) and Tritium (T) which produces a large amount of energy as given in Equation (1.2).

$$E = mc^2/ \tag{1.1}$$

$$D + T \rightarrow {}^4He\,(3.5MeV) + n\,(14.1MeV) \tag{1.2}$$

Energy is an important aspect in our lives and the industrialization of the planet demands increasing level of energy day by day. The current available energy sources,

which rely on fossil fuel such as oil, gas and coal that are not only getting depleted but are also seriously harming this living planet. To meet the world's increasing energy demands and safety of the planet, newer discoveries of the efficient alternative energy sources are the burning questions of century. Mankind always has learned though the nature and therefore the human being has started to make an identical sun on the earth through the controlled thermonuclear fusion reaction.

Different approaches have been investigated for the controlled fusion studies. On earth the controlled fusion has been successfully achieved with two major approaches termed as inertial confinement fusion (ICF) and magnetic confinement fusion (MCF). In this thesis, the focus is on magnetic confinement fusion. The aim of magnetic confinement fusion is to confine a mixture of hydrogen-isotope gas at temperatures in the order of 10 keV ($\approx$ 100 million K). If the density is high enough and the confinement time is long enough then it would lead to net energy producing fusion reactions. The hydrogen gas is ionized at this temperature, it is in the plasma state. A strong magnetic field traps the charged particles of the plasma. Due to the Lorentz force, the particles move circularly around the field lines, and this way they are not allowed to stream freely in the direction perpendicular to the magnetic field. But along the field lines they can move without restriction (apart from some very infrequent collisions). In order to confine the particles in a finite space, the magnetic field lines are bent into a shape of a torus (Figure 1.1).

This magnetic field can be realized by simple circular coils arranged along the torus as shown in Figure 1.1. This figure shows the main coordinates and directions: the toroidal direction is along the field lines, the poloidal direction is perpendicular to the field lines.

One problem with this toroidal arrangement is that the magnetic field is not homogeneous, and it causes the particles to drift in a way that polarizes the plasma and degrades the confinement. More precisely, due to the inhomogeneity and the curvature of the magnetic field, the positive and negative particles drift in opposite directions, and this creates an electric field that drives both the electrons and the ions out of the torus [7]. To circumvent this effect, the plasma has to have a helical field structure, as shown in Figure 1.2. The helical field short-circuits plasma and thus prevents, the formation of a strong electric field which then expels the particles from the container.

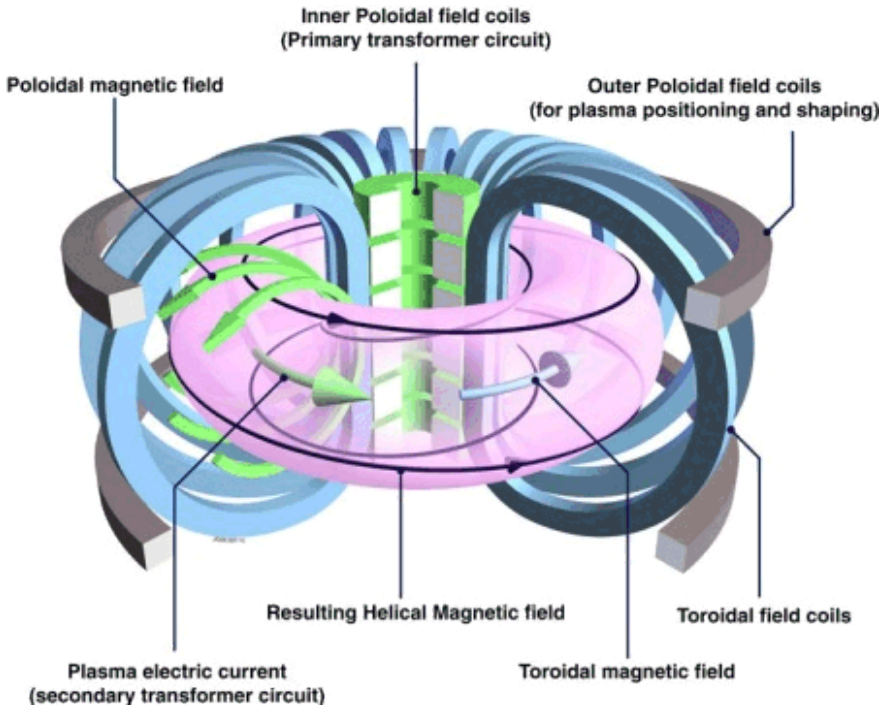

Fig. 1.1 Schematic diagram of the Tokamak, with toroidal and poloidal filed coils. (Image from CCFE - http://www.ccfe.ac.uk)

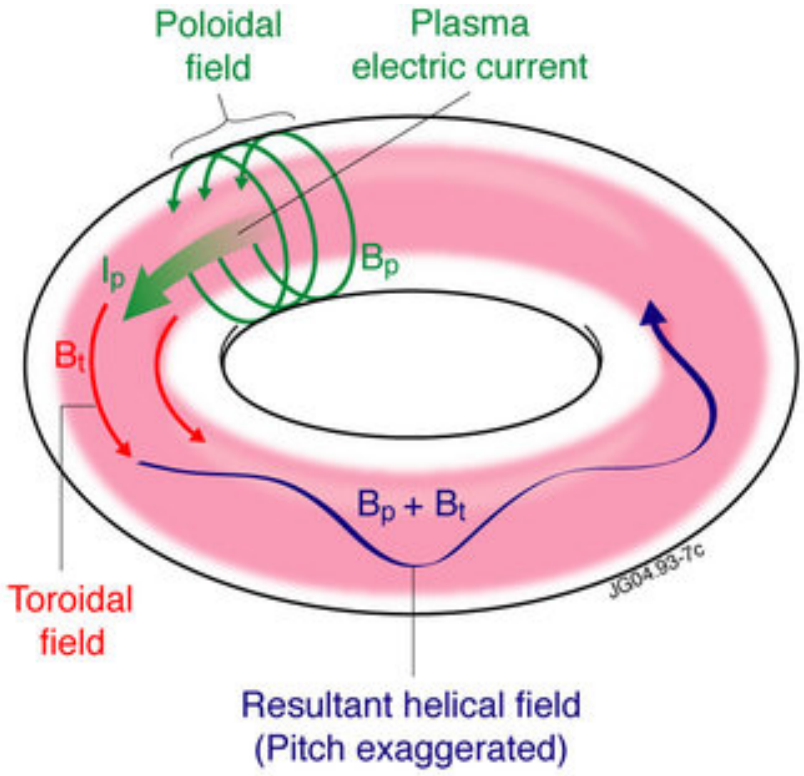

Fig. 1.2 A schematic diagram representing the helical resultant field from summing the toroidal and poloidal fields. (Image from - www.efda.org)

In helical magnetic configuration, both the toroidal and poloidal coordinates change along a field line. After traversing a number of poloidal turns, a field line reconnects on rational surfaces with its tail by forming a toroidal surface called as flux surface. A typical flux surface is shown in Figure 1.3.

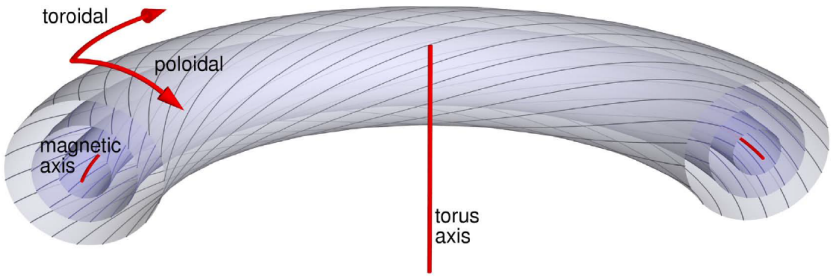

Fig. 1.3 Some of the nested magnetic flux surfaces and the magnetic field lines that wind helically around the torus on these surfaces are depicted [1].

Toroidal magnetic fusion devices construct flux surfaces in order to define plasma parameters. Characterization of the field lines traversing behavior is performed by introducing the rotational transform. It is denoted by iota-bar, ι and defined as follows: let $\Delta\theta_n$ be the change of the poloidal angle after n toroidal turns, then, the rotational transform is defined as

$$\iota = \lim_{n\to\infty} \frac{1}{n}\Delta\theta_n \tag{1.3}$$

which is the average change of the poloidal angle after a toroidal turn [8]. In tokamak plasmas, the inverse of the rotational transform is used, which is called safety factor, and denoted by symbol (q)

$$q = 2\pi/\iota \tag{1.4}$$

Stellarators [9] are capable of steady-state operation and they confine a plasma using helical coils that rotate around the plasma torus. The stellarator configurations generally lack axisymmetry because of the helicity of the external coil system. There are variety of stellarator configurations such as the classical stellarator, the torsatron, the heliac and the optimized stellarator. The basic difference among them is in the magnetic parameters and the symmetry of the magnetic field strength $\mathbf{B}$ on the magnetic surfaces. The classical stellerators as shown in Figure 1.4a consist of toroidal coils and helical windings which are problematic from an engineering point of view, such as being difficult to manufacture, assemble and repair. This design was modified in the modular stellarators, where the toroidal coils and helical windings are combined together, as shown in Figure 1.4b, which allows for optimization of the magnetic field.

An example of such a configuration is Wendelstein 7-X in Germany. The advantage of the stellarators comes from the capability of steady state operation. Their negligible toroidal current diminishes current driven instabilities, such as disruptions and resistive wall modes as compared to tokamaks.

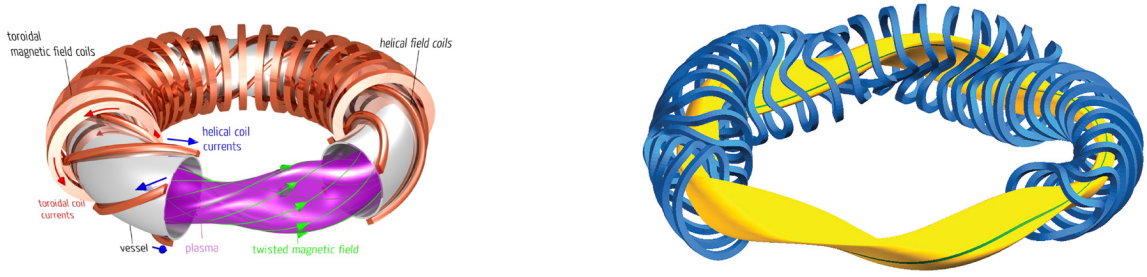

(a) Classical stellarator (b) Modular stellarator

Fig. 1.4 Difference between stellarators

1.2 Motivation

In the development of fusion plasma physics, plasma heating is an important aspect. Without proper heating level the achievement of fusion reactions becomes impossible. In present-day fusion devices the plasma is heated by a number of external means such as ion/electron resonance waves and neutral beams. Plasma heating through self-generated fusion products is called as self-heating and it is of the primary importance for any viable device which could achieve a sustained level in its performance. Only a fraction of the power from fusion products remains available for plasma heating. In a viable fusion device, extracting more energy than the injection remains primary goal and reaching this point is termed as ignition condition in fusion physics. Fusion products, such as Alpha particles which normally appear after fusing the hydrogen isotopes can help to achieve ignition margins if their sufficient energy gets efficiently absorbed into the background plasma. However, it is not easy to maintain enough energy within the fusion chamber which can approach to ignition margins.

There can be many potential factors for the limited availability of fusion power for the self-heating of background plasma in current fusion devices such as fewer fusion reactions, pulsed operation scenarios and the lower density of Alpha particles due to excluded Tritium (T) use. Besides of these operational limits, the MHD instabilities in the range of Alfvén velocity also called Alfvénic instabilities are also responsible for the limited fusion power available for self-heating. Alfvénic instabilities resonate

with the energetic particles/ fast ions and channel out them from the device before their release of energy to the background plasma and make them unavailable for the heating purpose. Power balance calculations suggest that nearly the 20% of fusion product power is necessarily required in order to achieve ignition margins in the fusion devices [10]. Scientific aspects which inhibit to approach ignition margins and the severe impact of channelled fast ions on the plasma facing components (PFCs) demand state-of-the-art investigations of Alfvénic instabilities in fusion systems. The ultimate goal of the sustained fusion reaction is possible with the comprehensive understanding of the scientific aspects of energetic particle driven Alfvénic instabilities.

In this thesis, energetic particle driven Alfvénic instabilities are investigated for the TJ-II Stellarator and ASDEX-Upgrade (AUG) tokamak using state-of-the-art three dimensional (3D) numerical tools. In TJ-II stellarator the chirping, steady and Reversed shear Alfvén modes have been observed experimentally, their analysis though ab initio modelling have been required for better understanding of the physics behind such instabilities in stellarator plasmas. In AUG tokamak and similar devices, the helical core structures have been measured with the appearance of strong sawteeth modes that can drive fast ions. Their impact on shear Alfvén modes has been considered an important scientific problem which demands for the modelling of such phenomena in order to better understand its physics. The outcome of these investigations can be important for the future upcoming fusion devices such as the ITER and DEMO, since 3D physics is pertinent in these devices [11]. In stellarator fusion devices which are inherently disruption free, the fast ions mostly face interactions with the helical Alfvén eigenmodes (HAEs) [12–14] and Global Alfvén eigenmodes (GAEs) [15]. Their investigations are of the paramount importance in such helical plasmas. In fusion systems besides the HAEs and GAEs, Reversed Shear Alfvén eigenmodes (RSAEs) [16] also equally called Alfvén cascades (ACs) [17] are also of primary importance because of their role in active MHD spectroscopy [18–20] to measure the rotational transform (iota) [21] in stellarators and/or the safety factor (q) profile in tokamaks. RSAEs are observed in most of the fusion devices as frequency sweeping modes and their finite variations with time lead to the investigations of iota or q-profile.

In tokamaks which are inherently axisymmetric (2D) fusion devices since the toroidal coordinate is considered invariant, however in optimized designs currently the 3D internal and external effects have been experimentally observed/ added to achieve the required level performance. Resonant magnetic perturbations are added externally in tokamak plasmas to control and suppress the Alfvénic instabilities [22] which transform the magnetic field structure of torus into 3D format by removing

the axisymmetry of magnetic field. Saturated internal ideal kink-modes are present in tokamak plasmas for the steep plasma pressure forming 3D helical core structures as an equilibrium state, which perturbs field axisymmetry and transforms into 3D field structure [23]. For the first time in this thesis, effect of such spontaneously triggered helical core structures [24] on the Alfvénic instabilities is investigated for the understanding of the low-frequency Alfvén eigenmodes (AEs).

It is believed that work developed in this thesis would certainly help to improve the comprehensive understanding of burning plasma Alfvénic instabilities in fusion science.

1.3 List of publications

The following list of publications are the articles which are published or submitted for the publication during this doctoral work carried out in this thesis.

- **Allah Rakha**, et al., *Modelling of beam-driven Alfvén modes in TJ-II plasmas*, Nucl. Fusion **59** (2019) 056002.
- **Allah Rakha**, et al., *Shear Alfvén wave continuum spectrum with bifurcated helical core equilibria*, Accepted in Nuclear Fusion August 2019.
- **Allah Rakha**, et al., *Modelling of Alfvén cascade modes in stellarator plasmas*, Submitted to Nuclear Fusion 2019.
- **Allah Rakha**, et al., *Modelling of Alfvén cascades in NBI heated stellarator plasmas*, Europhysics Conference Abstracts vol **42A** P4.1004 (http://ocs.ciemat.es/EPS2018PAP/pdf/P4.1004.pdf), 2018.

1.4 Conference poster and oral presentations

Throughout the thesis I had the opportunity to present my work on the leading conferences, this is the list of oral talks and posters which I have presented during the course of my PhD studies.

- **Poster**, Modelling of reversed shear Alfvén modes in NBI heated stellarator plasmas using reduced MHD model, *6th FuseNet PhD Event hosted by the ITER Organisation, 07-09 November, 2018 Cadarache, France.*

- **Poster**, Modelling of Alfvén cascades in NBI heated stellarator plasmas, *13th Carolus Magnus Summer School on Plasma and Fusion Energy Physics, September 03-14, 2018, DIFFER Eindhoven, The Netherlands.*

- **Poster**, Modelling of Alfvén cascades in NBI heated stellarator plasmas, *45th European Physical Society (EPS) Conference on Plasma Physics, July 02-06, 2018, Prague Czech Republic.*

- **Oral**, Modelling of Alfvénic instabilities in complex toroidal geometries for fusion, *5th International BSC Doctoral Symposium, April 24-25, 2018 Barcelona, Spain.*

- **Oral**, Modelling of Energetic Particle-Driven Alfvénic instabilities in TJ-II plasmas, *Workshop on Fast Ion Physics, Jan 22-23, 2018 at IPP Greifswald, Germany.*

- **Poster**, Modelling of Alfvén modes properties in TJ-II plasmas, *17th European Fusion Theory Conference (EFTC), October 09-12, 2017 Athens, Greece.*

- **Poster**, Simulations of Alfvénic modes in TJ-II Stellarator, *4th International BSC Doctoral Symposium, May 02-04, 2017 Barcelona, Spain.*

- **Poster**, Modelling of Alfvén Eigenmodes in TJ-II Plasmas, *Joint iCTP-IAEA College on Plasma Physics, November 07-18, 2016 Trieste, Italy.*

1.5 Dissertation structure

In this thesis, the modelling and simulation results using 3D numerical tools of the experimentally observed Alfvén eigenmodes (AEs) in TJ-II Stellarator and AUG tokamak are discussed. The logical approach employed to develop this thesis is presented as follows. In chapter 1, the basic introduction of fusion science, motivation of this specific research topic and list of contributions during my PhD studies are provided. Introduction to the Alfvén waves and Alfvén eigenmodes (AEs) in cylindrical and toroidal geometries along with the brief description of AEs both in tokamak and stellarator plasmas is provided in chapter 2. The description of the reduced MHD model for the investigation of AEs in 3D toroidal devices along with the MHD equilibrium reconstruction numerical tool (VMEC) for the 3D toroidal devices with closed flux-surfaces is provided in chapter 3. It also briefly discusses the numerical tools for the Alfvén continuum calculations (STELLGAP) and modes structures (AE3D).

Modelling and simulation of steady and chirping AEs are discussed in chapter 4 for the both iota rising and lowering TJ-II dynamic plasmas. The research findings for the Alfvén cascade modes in TJ-II plasmas and possible recommendations for the MHD spectroscopy usage for active and accurate finding of iota values are discussed in chapter 5. The non-linear wave-particle interaction (WPI) modelled using Monte Carlo transport model for the TJ-II plasmas is detailed in chapter 6. This chapter also provides a brief description of the DELTA5D code used for the WPI modelling. In the first part of chapter 7, a methodology for the reconstruction of bifurcated MHD equilibria with the formation of 3D helical core in tokamak plasmas is provided. In the second part, the effect of 3D helical core Alfvén continuum structures is described and compared with 2D the kinetic calculations. Lastly, the chapter 8 provides the overall summary of the research findings discussed in this thesis and also provides brief recommendations for the future outlook in this field of research.

Chapter 2

Alfvén waves and Alfvén eigenmodes

This chapter serves as an introduction to ideal MHD Alfvén waves and Alfvén eigenmodes (AEs) in toroidal geometry. It is intended to give the reader a basic notion of these MHD waves and the formation of such coherent structures/modes in toroidal plasmas.

2.1 Alfvén waves in ideal MHD model

Ideal MHD model describes low-frequency electromagnetic transverse waves with an analogy of transverse waves in a stretched string. These waves are called Alfvén waves named after H. Alfvén who defined them for the first time in 1942 [25]. These waves appear due to tension in magnetic ropes because of the frozen in flux property of the conducting fluid (plasma) and propagate parallel to the magnetic field lines with an Alfvénic speed.

The description of the MHD waves is provided with the ideal MHD model under these limitations.

1. Electron inertia is neglected due to the MHD frequency being lower than electron cyclotron and plasma frequencies

2. Debye length is small so plasma is considered quasi-neutral.

3. Electron motion is very fast than the time scales of interest and leads to eliminate displacement current, therefore permittivity $\epsilon \rightarrow 0$ in Maxwell equations.

4. Plasma pressure is considered isotropic because of the adiabatic behaviour as heat flow is slower than the MHD time scales
5. Plasma is treated as conducting fluid
6. Ideal Ohm law is employed

The moments of the ideal MHD model and Maxwell equations which describes MHD waves are provided below.

$$\frac{\partial \rho_m}{\partial t} + \nabla \cdot (\rho_m \vec{v}) = 0 \qquad \text{[Continuity equation]} \tag{2.1}$$

$$\rho_m \frac{d\vec{v}}{dt} + \nabla P - \vec{J} \times \vec{B} = 0 \qquad \text{[Momentum equation]} \tag{2.2}$$

$$\frac{d}{dt}\left(\frac{P}{\rho^\gamma}\right) = 0 \qquad \text{[Equation of state]} \tag{2.3}$$

$$\vec{E} + \vec{V} \times \vec{B} = 0 \qquad \text{[Ideal Ohm's law]} \tag{2.4}$$

$$\nabla \cdot \vec{B} = 0 \qquad \text{[No magnetic monopoles]} \tag{2.5}$$

$$\nabla \times \vec{B} - \mu_0 \vec{J} = 0 \qquad \text{[Ampere's law]} \tag{2.6}$$

$$\frac{\partial \vec{B}}{\partial t} + \nabla \times \vec{E} = 0 \qquad \text{[Faraday's law]} \tag{2.7}$$

where ρ_m is the mass density of the plasma, $\vec{v}$ is the fluid velocity, $\vec{J}$ is the plasma current density, P is the plasma pressure, $\vec{E}$ and $\vec{B}$ are the electric field and magnetic field respectively, the γ is a ratio of specific heats C_p/C_v and $\frac{d}{dt} = \frac{\partial}{\partial t} + \vec{v} \cdot \nabla$ is the convective derivative.

The MHD model is considered important for the reconstruction of the plasma equilibrium configuration and for determining the stability of the reconstructed equilibrium. It also provides a possibility of investigating the plasma waves and their limitations which can support the stabilized plasma equilibrium. The investigations of the plasma stability with the plasma waves is an active field of research in fusion plasmas since it provides a basic understanding of the active plasma heating and diagnostic by launching externally plasma waves.

These equations are linearised by introducing an equilibrium time-independent part and a small first-order time-dependent perturbation for the given quantities. Plasma motion is neglected by considering $V_0 = 0$, higher order perturbations are ignored and fluid displacement vector $\vec{\xi}(\vec{r}, t)$ is defined as $v_1 = \partial\vec{\xi}/\partial t$. After transforming the perturbed quantities in terms of the $\vec{\xi}$, this system of equations is solved in an eigenvalue equation for $\vec{\xi}$ in terms of the equilibrium quantities as follows,

$$\rho_0 \frac{\partial^2 \vec{\xi}}{\partial t^2} = F(\vec{\xi}) \qquad \text{with} \tag{2.8}$$

$$F(\vec{\xi}) = \frac{1}{\mu_0}\left[\left(\nabla \times \vec{B}\right) \times \left[\nabla \times (\vec{\xi} \times \vec{B})\right] + \left(\nabla \times \left\{\nabla \times (\vec{\xi} \times \vec{B})\right\}\right) \times \vec{B}\right] + \nabla\left(\vec{\xi} \cdot \nabla p + \gamma p \nabla \cdot \vec{\xi}\right) \tag{2.9}$$

A normal mode approach is used to reformulate the Equation 2.8 into an eigenvalue equation to study the perturbations and waves of the plasma. In this approach the time variation of all the perturbed quantities is considered as of the form $\tilde{Q}((r), t) = Q(\mathbf{r})e^{-\iota\omega t}$. This formulation translates Equation 2.8 as follows,

$$-\omega^2 \vec{\xi} = \frac{1}{\rho_0} F(\vec{\xi}) \tag{2.10}$$

where $\vec{\xi}$ is no more a function of time. Equation 2.10 represents an eigenvalue system with ω^2 an eigenvalue with suitable boundary conditions of the $\vec{\xi}$. Solution of this system obtained though ideal MHD formulation may result in either exponentially growing modes for $(\omega^2 < 0)$ or oscillatory waves for $(\omega^2 > 0)$. Before diving into the geometrical dependencies for the explanation of the MHD waves, it is worth to briefly discuss MHD stable normal modes for the homogenous plasma.

2.2 MHD Waves in the homogeneous plasma

In an infinite homogenous plasma with straight magnetic field defined as $\mathbf{B} = B_0\mathbf{e_z}$ with wave vector $\mathbf{k} = k_\perp \mathbf{e_y} + k_\parallel \mathbf{e_z}$ and normal mode represented as $\tilde{\xi} = \xi e^{\iota(\mathbf{k}\cdot\mathbf{r} - \omega t)}$ the

ideal MHD eigenvalue equation becomes as,

$$\begin{bmatrix} \omega^2 - k_\parallel^2 v_A^2 & 0 & 0 \\ 0 & \omega^2 - k_\perp^2 v_S^2 - k^2 v_A^2 & -k_\perp k_\parallel v_S^2 \\ 0 & -k_\perp k_\parallel v_S^2 & \omega^2 - k_\parallel^2 v_S^2 \end{bmatrix} \begin{bmatrix} \xi_x \\ \xi_y \\ \xi_z \end{bmatrix} = 0 \tag{2.11}$$

where $v_A = \sqrt{B^2/\mu_0\rho}$ is the Alfvén speed and $v_S = \sqrt{\gamma p/\rho}$ is the adiabatic sound speed. Non-trivial solutions of these equations are the roots of the determinant of the matrix are the dispersion relations given in the following quadratic equation,

$$\left(\omega^2 - k_\parallel^2 v_A^2\right)\left[\omega^4 - (v_S^2 + v_A^2)k^2\omega^2 + (kk_\parallel v_S v_A)^2\right] = 0 \tag{2.12}$$

In ideal MHD model while considering plasma compressibility three different types of the waves are obtained because of the cubic polynomial in ω^2 which describe the plasma perturbations and modes of oscillation. Each solution represents a normal MHD mode of the homogenous magnetized plasma. These are the fast magnetosonic (or compressional Alfvén), slow magnetosonic and shear Alfvén (or torsional) waves. The graphical representation of these three different types of waves in plasma displacements ξ is shown in Figure 2.1 below. Brief description of the each of these MHD waves is

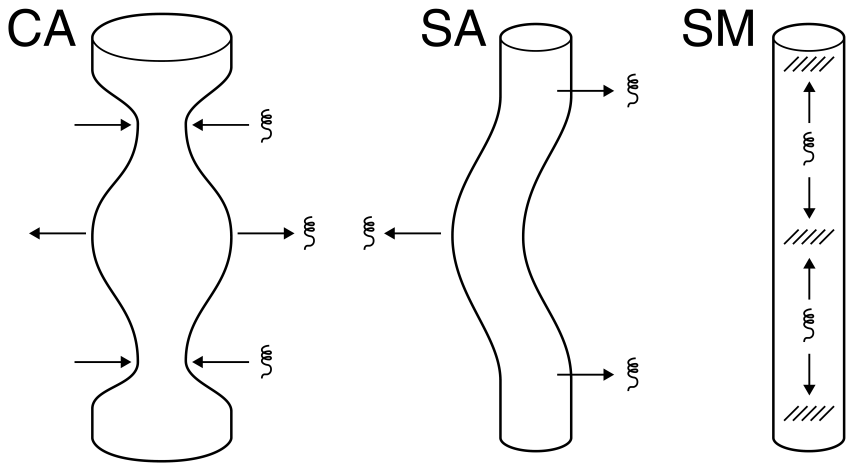

Fig. 2.1 Plasma displacement ξ in three types of MHD waves: Compressional Alfvén (CA), Shear Alfvén (SA), and Slow Magnetosonic (SM) [2]

provided below.

2.2.1 Shear Alfvén waves

The first root of the dispersion relation of Equation 2.12 corresponds to the shear Alfvén wave that is completely independent of the $k_\perp$ even when the $k_\perp \gg k_\parallel$. The dispersion relation for these shear Alfvén waves is given below,

$$\omega^2 = k_\parallel^2 v_A^2 \tag{2.13}$$

These are incompressible transverse waves with both perturbed velocity and magnetic field perpendicular to background magnetic field. They represent a balance between plasma inertia and field line tension appearing due to the stretched magnetic field lines frozen in flux. The group velocity of the Alfvén wave is always parallel to the magnetic field and there is no communication across field lines. This allows adjacent lines of force to shear across each other, lending the descriptive name shear to the Alfvén wave.

2.2.2 Fast magnetosonic waves

Two further branches of waves are obtained from the Equation 2.12 for the fast and slow magnetosonic waves which appear due to the coupling of sound-waves with the Alfvén waves. The fast magnetotactic waves appear due to the magnetic compression of the waves and their phase speed is relatively higher than the shear Alfvén waves, their dispersion relation comes together with the slow-magnetosonic waves as given below,

$$\omega^2 = \frac{1}{2}k^2\left(v_S^2 + v_A^2\right)\left[1 \pm \sqrt{1 - 4\frac{k_\parallel^2}{k^2}\frac{v_S^2 v_A^2}{(v_S^2 + v_A^2)^2}}\right] \tag{2.14}$$

The equation with the positive sign of Equation 2.14 corresponds to the fast magnetosonic or magneto-acoustic wave. This is a compressional wave, and so $\nabla \cdot v1$ remains non-zero and the perturbed magnetic field has components both parallel and perpendicular to the equilibrium field. A useful parameter characterising the equilibrium is the plasma beta β. The plasma is considered in an equilibrium state when the force balance condition $J \times B = \nabla P$ holds everywhere in the system. Plasma beta is defined as the ratio of the plasma pressure to the magnetic pressure, $\beta = 2\mu_0^2 P/B^2$.

In the low beta limit defined as $\beta \sim v_S^2/v_A^2 \ll 1$, the fast magnetosonic wave transforms into compressional Alfvén wave or the fast wave and it propagates isotropically with the Alfvén speed v_A. Its dispersion relation is given as,

$$\omega^2 = \left(k_\parallel^2 + k_\perp^2\right) v_A^2 = k^2 v_A^2 \tag{2.15}$$

2.2.3 Slow magnetosonic waves

The smaller frequency branch from the second term in Equation 2.14 describes the slow magneto-acoustic wave, this wave always oscillating at frequencies below that of the Alfvén wave. It appears due to the coupling of the fluid compression with the sound waves. Likewise the fast wave branch, the slow-wave is also polarized so that the plasma pressure and the magnetic field are compressed. In the low beta limit the slow wave reduces to the familiar ion sound wave in the parallel direction, $\omega^2 \approx k_{\parallel}^2 v_S^2$, it does not propagate in the perpendicular direction. In this case the mode is almost longitudinal because $k_{\perp} \cdot v1 \approx 0$. The sound wave describes a basic oscillation between the parallel plasma kinetic energy and the plasma internal energy.

An important difference between these waves is that the shear Alfvén waves have no magnetic field induced parallel to the toroidal magnetic field, whereas the compressional Alfvén waves do have a magnetic component parallel to B. In cylindrical plasmas the compressional modes have a lower cutoff frequency below which these modes do not exist. This is not a characteristic of the shear Alfvén waves, making these more easily excited and studied in laboratory plasmas.

2.3 Alfvén waves in cylindrical geometry

It is important to discuss Alfvén waves in the cylindrical geometry because of its practical similarities with the toroidal geometry and the formation of cylindrical modes equally called Global Alfvén eigenmodes (GAEs). Cylinder is considered a simplified form of the torus with radius R and length $2\pi R$ in which bending on the edges is ignored however periodicity along the z-direction with period $2\pi R$ is retained. The resulting plasma configuration is very similar to the screw pinch.

In a cylindrical screw pinch the magnetic field has two components, namely axial and azimuthal and it remains non-uniform because of its curved geometry. The inverse pitch of the magnetic field describing the winding ratio of the toroidal axial field to the poloidal field, known as the safety factor, q is an important factor in the stability of the screw pinch. In toroidal geometry, it measures the number of toroidal turns of the field line for traversing one poloidal turn and is defined as,

$$q = \frac{rB_z}{RB_\theta} \tag{2.16}$$

where r is the local minor radius, B_z is the axial magnetic field, and B_θ is the azimuthal field. It is important to notice that q remains finite at magnetic axis (r = 0) since the

poloidal field is proportional to r near the magnetic axis. A Taylor expansion of the current density near magnetic axis, $J_z(r) \approx J_{0z} + rJ'_{0z}$ approximates the poloidal field as $B_\theta \approx \frac{1}{2} r\mu_0 \left(J_{0z} + \frac{2}{3} rJ'_{0z}\right)$. At limit $r \to 0$, q at the magnetic axis (q_0) becomes,

$$q_0 = \frac{2B_z}{\mu_0 R J_{0z}} \tag{2.17}$$

In the toroidal geometry the axial and azimuthal magnetic fields will be toroidal B_Φ and poloidal B_θ fields respectively. q will be properly defined as a flux surface averaged quantity instead of normal radial coordinate because in toroidal geometry radial coordinate is translated into flux function as $\rho = \sqrt{\psi}$, where ψ is the radial flux enclosed.

The eigenmodes of the periodic cylinder are defined by a radial eigenfunction $\xi(\psi)$ with frequency ω and the integer toroidal and poloidal wavenumbers, n and m, respectively. The parallel wavevector is defined as,

$$k_\parallel = \frac{\mathbf{k} \cdot \mathbf{B}}{B} = \frac{B_\Phi}{BR} (n + m/q)$$

Since $B = B_\Phi + B_\theta$ and $B_\Phi \gg B_\theta$ in periodic cylinder then the parallel wavevector becomes,

$$k_\parallel \approx \frac{1}{R} (n + m/q) \tag{2.18}$$

In cylindrical plasmas the Alfvén speed, v_A is a function of the radial flux and varies continuously along the radius from the magnetic axis to the plasma edge. The continuous variation of the Alfvén frequency ω_A for a particular wavevector k is called the Alfvén continuum defined as,

$$\omega^2(r) = k_\parallel^2 v_A^2(r) \tag{2.19}$$

2.3.1 Cylindrical shear Alfvén waves - Continuum modes

Shear Alfvén waves radially propagating in a cylindrical geometry form continuum modes. Their propagation in an arbitrary cylindrical geometry is shown in Figure 2.2. It shows the continuum waves traverse in the radial extent and cross each other. In cylindrical geometry these waves accommodate eigenmodes around their extrema points or otherwise modes face strong continuum damping as shown in Figure 2.3.

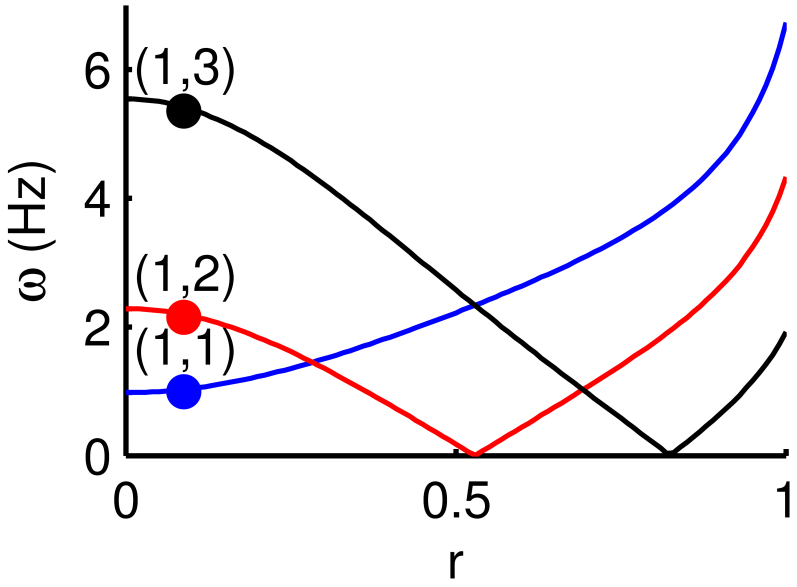

Fig. 2.2 Alfvén continuum structures for the discrete set of modes (m, n) in an arbitrary cylindrical geometry [3]

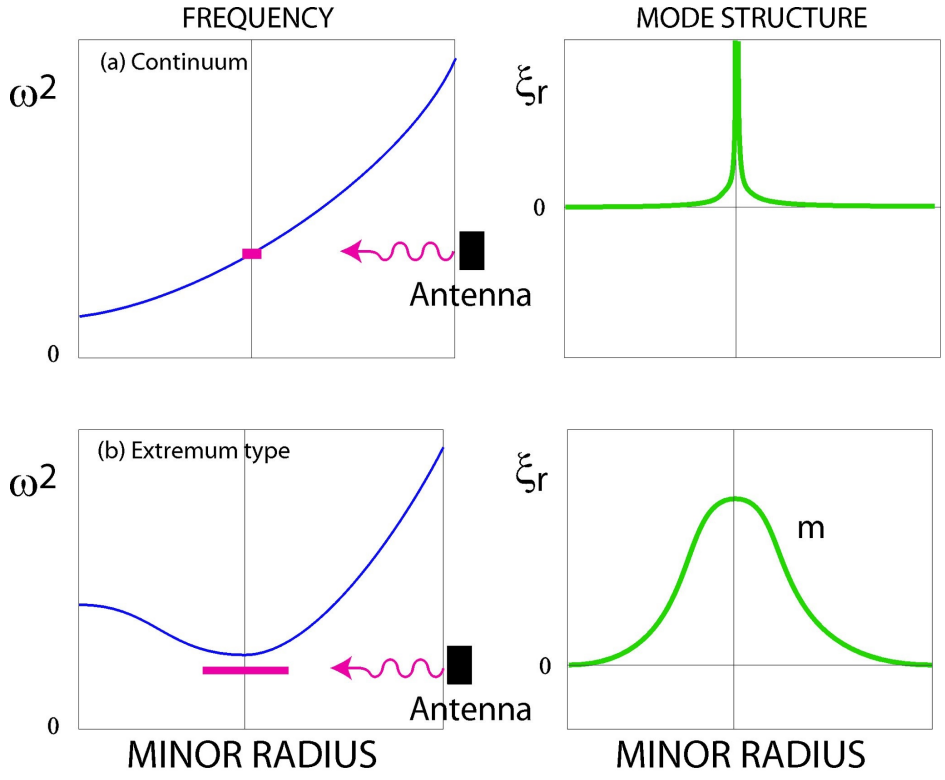

Fig. 2.3 Alfvén continuum (left) and mode structures (right). (a) Mode with continuum damping (b) mode lying beneath the continuum extrema [4]

.

2.4 Alfvén waves in toroidal geometry

In an arbitrary cylindrical geometry the end losses become significant, therefore bending a cylinder into a circular cross-section gives a torus of finite aspect ratio. This gives an unavoidable 1/R dependence of the toroidal magnetic field. This dependence results in the poloidal variation of magnetic field over a flux surface, which demands safety factor computation as an average over the flux surface,

$$q = \frac{1}{2\pi} \oint \frac{r}{R} \frac{B_\Phi}{B_\theta} d\theta \approx \frac{r B_\Phi}{R B_\theta}$$

The 1/R dependence of the **B** acts as periodic index of refraction for the variations in poloidal magnetic field which leads to coupling of the continuum of different poloidal harmonics at their degenerate localizations. For the lower values of a/R_0 and identical toroidal mode number (n), a poloidal harmonics ξ_m couples to its adjacent side band $\xi_{m\pm1}$. This coupling at the degeneracy forms forbidden gaps in the Alfvén continuum [26]. The formation of continuum gaps is a generic wave phenomenon analogous to the Bragg reflection in a crystal lattice and the electron band gaps in semiconductors. Frequency gaps in Alfvén continuum accommodate discrete modes which do not encounter with continuum damping.

Two counter-propagating Alfvén waves with different poloidal mode numbers while crossing rational surface of q lead to generate frequency gaps as shown in Figure 2.4 because of the dependence of parallel wave vectors $k_\parallel$ on poloidal harmonics m and periodicity θ. For specific plasma profiles, the frequency gap in the continuum may extend along the whole plasma column. The frequency satisfied at the degeneracy of the two counter-propagating poloidal harmonics m and $m+1$ is given as,

$$k_{\parallel m} v_A = -k_{\parallel m+1} v_A$$

$$\frac{1}{R}\left(n + \frac{m}{q}\right) = -\frac{1}{R}\left(n + \frac{m+1}{q}\right)$$

which leads to the safety factor for the degeneracy of two wave vectors,

$$|q| = \frac{m + \frac{1}{2}}{n}$$

Because of the toroidicity induced gaps, the modes residing there are called Toroidal Alfvén eigenmodes (TAEs). As TAEs lie in the gaps and they do not experience heavy

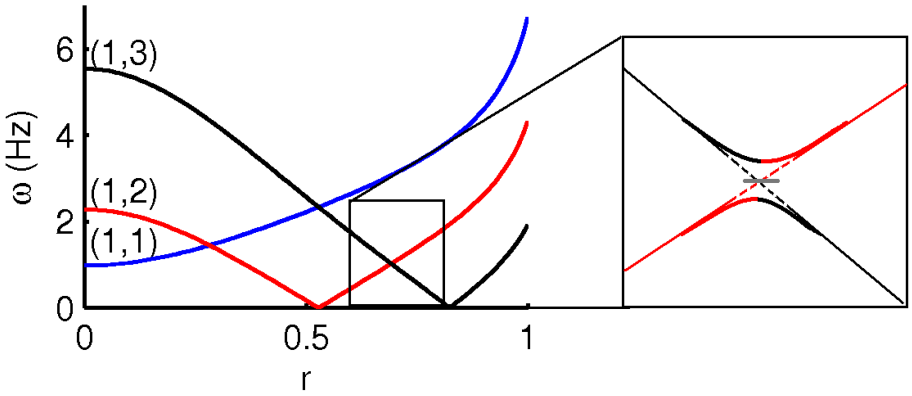

Fig. 2.4 Generation of the frequency gap by the coupling of two different poloidal harmonics [3].

continuum damping therefore, they are weakly damped modes. In a typical way, the gap generation and the existence of the TAE gap are shown in Figure 2.5.

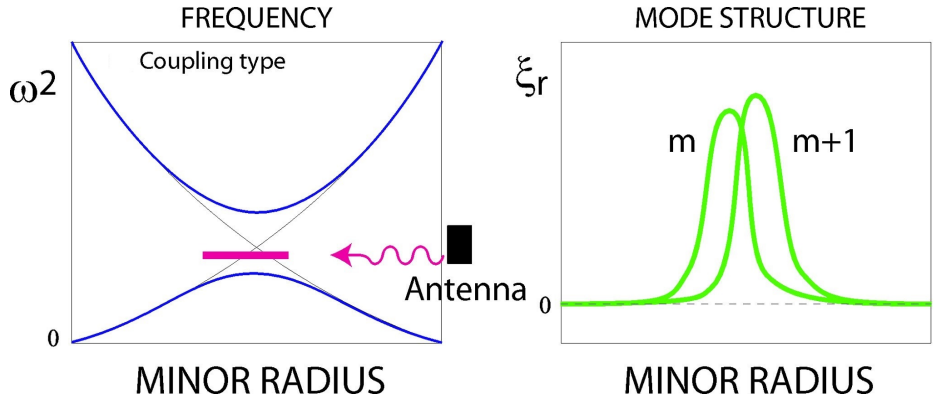

Fig. 2.5 Coupling of two different poloidal harmonics in a torus and the corresponding TAE [4].

TAEs are both core and edge localized modes in the toroidal plasmas with an estimated gap frequency of $\omega^2 = (v_A/2qR)^2$ and parallel wave vector $|k_\parallel| = 1/2qR$. In the plasma core, the TAEs can avoid continuum damping if their amplitudes remain lower while crossing the continuum. The dispersion relation of TAEs shows the two branches of the poloidal harmonics arise near top and bottom of the frequency gap. The higher frequency branch has higher amplitude and lower one has smaller amplitude in the mode structure of TAE formed by the two prominent poloidal harmonics.

2.5 Alfvén eigenmodes in tokamak and stellarator plasmas

The basic phenomenon of Alfvén modes is similar in tokamak and stellarator plasma due to the fact that both devices have toroidal topology. Experiments have shown that the TAEs and Elliptic Alfvén eigenmodes (EAEs), where the gaps are generated by poloidal coupling, can be found in both types of devices. The extremum modes which appear below or above an extrema of the Alfvén continuum are GAEs or Reverse Shear Alfvén eigenmodes (RSAEs). They are also present both in tokamak and stellarator plasmas. Three-dimensionality of stellarators can allow additional Alfvén modes to appear. The modes induced due to the helicity of the stellarators are defined as Helical Alfvén eigenmodes (HAEs) which normally appear at higher frequencies. In tokamaks three-dimensional (3D) effects are present due to the saturated internal-kink modes and external resonant magnetic perturbations which distort their axial symmetry, therefore the investigations of 3D effects become important also for the tokamak plasmas.

In stellarators the lack of axial symmetry and strong shaping result in extended Fourier harmonics of the magnetic field by giving birth to a variety of additional modes. The extended set of Fourier harmonics in magnetic field makes an Alfvén continuum more populated. Additional gaps may open and some may merge into each other in Alfvén spectrum [27]. There can be global modes induced by helical coupling, where both the toroidal and poloidal harmonics coupling are significant. These helical Alfvén eigenmodes were first predicted theoretically [12], and later shown experimentally both in W7-AS [28] and LHD [14].

Experiments have shown that Alfvén modes in TJ-II stellarator appear with multiple poloidal and toroidal couplings in a wide frequency range over a wide set of plasma parameters [29]. Upon excitation by energetic particles, these modes can become the most relevant MHD activities in the plasma. Confinement of those energetic particles which may excite AEs is an important optimization criterion in the 3D fusion devices. In this thesis, the modelling and simulation are considered strong methodologies because of their direct association with ab initio theories to investigate observed MHD instabilities and their impact on the energetic particles confinement in fusion burning plasmas.

Chapter 3

Reduced MHD Model and Numerical Tools

This chapter briefly describes reduced MHD model followed by an explanation of the employed numerical tools based on it, in order to investigate the MHD stability in 3D toroidal fusion systems. Numerical tools include the STELLGAP code which is explained in this chapter both for the compressible and incompressible limits used for the Alfvén continuum computation and AE3D code used to search for discrete Alfvén eigenmodes (AEs). Prior to discuss these codes, a numerical model which calculates an equilibrium for 3D fusion devices i.e. VMEC is discussed with its extension to reconstruct the helical core equilibria for tokamak plasmas.

3.1 Reduced MHD model for the toroidal devices

The detailed derivations of the reduced MHD (RMHD) equations are provided in [30] which are beyond the scope of this thesis, the starting equations for AEs in a 3D equilibrium are the ideal MHD Ohm's law and the vorticity equation written in terms of the electrostatic potential ϕ,

$$\frac{\partial \delta\psi}{\partial t} = \frac{1}{B}\left(\mathbf{B}\cdot\nabla\phi\right) \tag{3.1}$$

$$\nabla\cdot\left[\frac{\rho}{B}\frac{d}{dt}\left(\frac{\nabla\phi}{B}\right)\right] = \mathbf{B}\cdot\nabla\frac{\delta J_{\parallel}}{B} + \delta\mathbf{B}\cdot\nabla\frac{J_{\parallel}}{B} \tag{3.2}$$

where $\delta\psi$ is a perturbed poloidal magnetic flux. Inserting Equation (3.1) into Equation (3.2) and defining perturbed quantities, $\delta J_{\parallel} = \nabla^2\delta\psi$ and $\delta\mathbf{B} = \nabla\zeta\times\nabla\delta\psi$

leads to the following eigenvalue equation,

$$\omega^2 \nabla \cdot \left(\frac{1}{v_A^2} \nabla \phi \right) + \mathbf{B} \cdot \nabla \left[\frac{1}{B} \nabla^2 \left(\frac{\mathbf{B}}{B} \cdot \nabla \phi \right) \right] + \nabla \zeta \times \nabla \left(\frac{\mathbf{B}}{B} \cdot \nabla \phi \right) \cdot \nabla \frac{J_\parallel}{B} = 0. \quad (3.3)$$

First term in this equation provides the inertia and the second provides the field-line bending. Both of these terms are available in the continuum equations. However, an additional third ballooning term in this equation describes the discrete AEs which are not present in the continuum wave equations. The eigenmode solutions of ϕ for this equation represent the discrete Alfvén modes and eigenvalues ω^2 as the mode frequencies.

In reduced MHD model, full MHD equations are transformed into a reduced set of MHD equations by using wavelength ordering. In wavelength ordering, the perpendicular wavelength of a perturbation is considered smaller than its parallel wavelength i.e. $\lambda_\perp / \lambda_\parallel \sim \epsilon$ and $\epsilon \ll 1$ which serves an expansion parameter. This wavelength ordering is defined for directions relative to a large-scale magnetic field. Since this set of reduced MHD equations is independent of the aspect ratio ordering, it can be applied on any general toroidal configuration. In this model the zeroth-order quantities satisfy an equilibrium equation and do not vary with time. This is because the expansion parameter (ϵ) has been defined by the anisotropy of the perturbed response. Consequently no assumptions are made on the zeroth-order quantities. Manifesting the MHD equilibrium and setting constraints to eliminate the fast time-scale perpendicular waves, the reduced MHD equations have been formulated for the evolution of scalar potential quantities on the time scales associated with the parallel wave vector (shear-Alfvén wave time scale), which are important for the plasma stability studies [30]. Energy conservation and divergence-free magnetic fields at the higher orders of expansion parameter have also been maintained in this formulation.

3.2 Three dimensional MHD equilibrium solver (VMEC)

The Variational Moments Equilibrium Code (VMEC) [31] is a numerical tool for computing three-dimensional MHD plasma equilibrium. It is the workhorse equilibrium reconstruction code for the stellarator devices. It obtains an equilibrium by using a variational method to find a minimum of the system energy [31, 32]. It solves the ideal MHD wave equations by iteratively minimising the energy functional over a toroidal

domain, using a steepest descent moment method. It computes a MHD equilibrium for a static and an isotropic plasma. Moreover, it assumes the plasma is characterised by nested and conserved magnetic flux surfaces. Therefore an equilibrium reconstruction for the configurations with magnetic islands and chaotic magnetic structures is beyond its scope. The equations solved iteratively in VMEC are the force-balance equation, and Ampére's and Gauss laws.

$$\mathbf{F} = \mathbf{J} \times \mathbf{B} - \nabla p = 0 \qquad \text{[MHD force balance]} \tag{3.4}$$

$$\nabla \times \mathbf{B} = \mu_0 \mathbf{J} \qquad \text{[Ampére's Law]} \tag{3.5}$$

$$\nabla \cdot \mathbf{B} = 0 \qquad \text{[Gauss Law]} \tag{3.6}$$

where $\mathbf{F}$ is a 'residual MHD force', which should vanish in the successful equilibrium reconstruction.

The volume-averaged total plasma energy is given by

$$W = \int \left(\frac{B^2}{2\mu_0} + \frac{p}{\gamma - 1} \right) dV. \tag{3.7}$$

Here first term corresponds to the magnetic energy, second is the kinetic energy, γ is an adiabatic index and the integration covers the full plasma volume.

To satisfy the conditions $\mathbf{B} \cdot \nabla p = 0$ and $\nabla \cdot \mathbf{B} = 0$ of MHD equilibrium, the magnetic field is written in the contravariant form as,

$$\mathbf{B} = \nabla\zeta \times \nabla\Psi + \nabla\Phi \times \nabla\theta^* \tag{3.8}$$

where Ψ corresponds to the poloidal flux as radial parameter in tokamaks and Φ to the toroidal flux as radial parameters in stellarators. The poloidal-like angle θ^* is $\theta^* = \theta + \lambda(\Psi, \theta, \zeta)$, with λ a poloidal periodic stream-function of θ and ζ with zero average over magnetic surface used to make the field lines straight. It is considered for the numerical reasons; the λ is used to normalize poloidal coordinate which allows the truncation of its Fourier series at a finite number of harmonics. In VMEC coordinates (s, u, v), where $s = \Psi/\Psi_{edge}$ is the normalized flux, $u = \theta$, and $v = \zeta$, the position of a guiding center (R, φ, Z) in terms of magnetic flux surfaces using Fourier series is

represented as,

$$R = \sum_{m,n} R_{m,n}(s)\, cos(mu - nN_{fp}v) \tag{3.9}$$

$$\varphi = v \tag{3.10}$$

$$Z = \sum_{m,n} Z_{m,n}(s)\, sin(mu - nN_{fp}v) \tag{3.11}$$

where N_{fp} the number of field periods of the configuration and m and n are Fourier harmonics of MHD modes. VMEC computes $R_{m,n}(s)$ and $Z_{m,n}(s)$ Fourier harmonics on a finite number of magnetic surfaces S_i where $i = l \cdots N_s$ and $R_{m,n}(s)$ and $Z_{m,n}(s)$ are only discrete functions of s. The Fourier harmonics for λ function which compute $N_s\lambda_{m,n}$ to transform VMEC coordinates into straight field line coordinates for the desired number of flux surfaces are given by,

$$\lambda = \sum_{m,n} \lambda_{m,n}(s)\, sin(mu - nN_{fp}v). \tag{3.12}$$

In the energy minimization process, VMEC looks for the set of flux surfaces with possible the lowest energy state. On the realization of the minimum energy state a stable ideal MHD equilibrium reconstruction is achieved. Important inputs in VMEC are the pressure profile, safety factor/iota profile, or the plasma current density profile and total enclosed magnetic flux edge. In addition, information regarding the initial magnetic flux geometry regarded as magnetic configuration is also added as an input. In order to specify magnetic boundary conditions, two different approaches are applied as per desired physics: fixed boundary and free boundary. In free boundary cases, the code is fed with specific locations and currents of the external coils. In such calculations, the last closed flux surface (LCFS) is permitted to evolve. For fixed boundary equilibrium reconstruction the $R_{m,n}(s)$ and $Z_{m,n}(s)$ Fourier components of the LCFS are specified as inputs, and the plasma boundary remains intact throughout the energy minimization process. In practice, free boundary calculations are set initially by providing specific current coil configuration and then the resulting edge flux and LCFS are generally employed as a starting point in the fixed boundary cases, which are relatively faster and more compact than the free boundary calculations.

3.2.1 MHD equilibrium solver VMEC for the helical core

In axisymmetric tokamak-like devices, the reconstruction of MHD equilibrium is usually performed in 2D formulation of the Grad-Shafranov equation. The 2D MHD

equilibrium reconstruction sufficiently provides a basis for MHD stability studies unless the 3D structures are introduced in the calculations. External 3D perturbations in the magnetic field are introduced in tokamak plasmas to achieve optimized plasma performance [22]. In contrast to external perturbations, the internal 3D perturbations referred to as helical or snake equilibria, have also been studied for different tokamak devices i.e TCV [23], MAST [33], ASDEX Upgrade [34], JET [24] and ITER [35]. These perturbations arise as the plasma self-organise to the lowest MHD energy state.

The mathematical description of the 3D MHD equilibrium reconstruction with a helical core using the 3D MHD equilibrium code VMEC [31] is based on the minimization of the plasma energy W given by Equation (3.7). It solves an inverse equilibrium problem in cylindrical coordinates to determine the distance from the major axis $R = R(s, u, v)$ and height above the mid-plane $Z = Z(s, u, v)$, where $0 \leq s \leq 1$ is the radial variable corresponding to the normalized enclosed toroidal magnetic flux, $0 \leq u \leq 2\pi$ denotes the poloidal angle and $0 \leq v \leq 2\pi/N_{fp}$ is the toroidal angle where N_{fp} is number of field periods around the torus.

The variation of energy with respect to time is given as

$$\frac{dW}{dt} = -\iiint ds\, du\, dv \left[F_R \frac{\partial R}{\partial t} + F_Z \frac{\partial Z}{\partial t} + F_\lambda \frac{\partial \lambda}{\partial t} \right] - \iint_{s=1} du\, dv \left[R \left(p_\perp + \frac{B^2}{2\mu_0} \right) \left(\frac{\partial R}{\partial u} \frac{\partial Z}{\partial t} - \frac{\partial Z}{\partial u} \frac{\partial R}{\partial t} \right) \right] \quad (3.13)$$

The last integral in Equation (3.13) defines the forces responsible for the movement of the plasma boundary. In fixed boundary calculations, the plasma-vacuum interface remains fixed. Therefore, by definition these forces vanish. The R and Z components of the MHD force are given $F_R = \sqrt{g}\, \nabla v \times \nabla Z \cdot F$ and $F_Z = \sqrt{g}\, \nabla R \times \nabla v \cdot F$ corresponding to the projection of the full force $\mathbf{F} = \mathbf{j} \times \mathbf{B}$ - $\nabla \cdot \mathbf{P}$. The λ force term is binormal (normal to the field line on a flux surface) force projection given as $F_\lambda = -\left(\sqrt{g} B \times \nabla s \cdot F / B^2 \right)$, where λ is poloidal angle re-normalization parameter, $\sqrt{g}$ is Jacobian and $p = p_\parallel = p_\perp$ is the isotropic pressure.

This system of MHD equations is solved iteratively by applying an accelerated steepest descent energy minimization scheme in VMEC. Fourier decomposition in the periodic angular variables u and v is used and a finite difference scheme is incorporated for the radial discretization. The radial force balance averaged over a flux surface is considered as diagnostic for the convergence of the reconstructed equilibrium state. It

is given by,

$$\left\langle \frac{F_s}{\Phi'(s)} \right\rangle = -\left\langle \frac{1}{\Phi'(s)} \frac{\partial p_\parallel}{\partial s}|_B \right\rangle - \frac{\partial}{\partial s}\left\langle \frac{\sigma B_v}{\sqrt{g}} \right\rangle - \iota(s)\frac{\partial}{\partial s}\left\langle \frac{\sigma B_u}{\sqrt{g}} \right\rangle \tag{3.14}$$

where Φ is toroidal magnetic flux function, prime ($\prime$) denotes the derivative with respect to s, $\sigma = 1/\mu_0$, B_u and B_v are poloidal and toroidal magnetic field covariant components respectively and F_s is covariant representation of the radial force, while $\iota(s) = 1/q$ the rotational transform of the magnetic field.

3.3 Numerical tools for Alfvénic instabilities

Based on the RMHD model, a set of numerical tools for the modelling of Alfvénic instabilities in 3D toroidal fusion systems has been developed. These specific tools are the Alfvén continuum solver (STELLGAP) [36] and AE3D [37] code for the modes analysis. Their brief description along with important mathematical formulation is provided in this section.

3.3.1 Alfvén continuum solver (STELLGAP) for 3D toroidal systems

The calculation of the shear Alfvén continua for 3D toroidal systems over a range of shapes and aspect ratios as a first step toward understanding Alfvénic instabilities are performed using STELLGAP code. In 3D toroidal systems strong poloidal/toroidal couplings of magnetic field introduce new continuum gap structures which are not present in axisymmetric tokamaks. Low field period (N_{fp}) and low aspect ratio devices result in strongly coupled toroidal mode families. The coupling of toroidal and poloidal mode harmonics in shear Alfvén waves lead to open helical induced Alfvén gaps in 3D fusion systems.

Compressible limit (STELLGAP)

For the analysis of shear Alfvén continuum and relevant gap structures, a specific tool i.e. STELLGAP [36] in the incompressible and low β limit is employed in these investigations. The detailed derivations used in STELLGAP are provided in [38]. The governing equation of STELLGAP for the computation of the continuum structures is

given as,

$$\mu_0 \rho_m \omega^2 \frac{|\nabla\psi|^2}{B^2} E_\psi + \vec{B} \cdot \vec{\nabla} \left\{ \frac{|\nabla\psi|^2}{B^2} \left(\vec{B} \cdot \vec{\nabla} \right) E_\psi \right\} = 0 \tag{3.15}$$

where ψ is the poloidal flux and E_ψ is the covariant component of the electric field, ρ_m is the mass density. In this equation the first term describes the wave's inertia and the second-term provides a restoring force (tension) via field-line bending. This equation is valid for three-dimensional toroidal geometry in the incompressible limit. This equation is solved using Boozer coordinates which are a special case of straight field-line coordinates and preserve zeros of the $(\mathbf{B} \cdot \nabla)$ operator [39, 40]. Equation 3.15 is represented in Boozer coordinates using the parallel gradient operator $(\mathbf{B} \cdot \nabla)$ and $|\nabla\psi|^2$ as follows,

$$\mathbf{B} \cdot \nabla = \frac{1}{\sqrt{g}} \left(\frac{\iota}{2\pi} \frac{\partial}{\partial\theta} + \frac{\partial}{\partial\zeta} \right), \tag{3.16}$$

$$|\nabla\psi|^2 = g^{\rho\rho} \left(\frac{d\psi}{d\rho} \right)^2. \tag{3.17}$$

Where ρ is the normalized flux surface label, θ and ζ are the poloidal and toroidal angles respectively, $g^{\rho\rho}$ is the contravariant $\rho\rho$ metric element and $\iota/2\pi$ is the rotational transform. Fourier series representation of electric field E_ψ, as $E_\psi = \sum_{m,n} E_\psi^{m,n} cos(m\theta - n\zeta)$ suggests that only an even parity of E_ψ would be sufficient for the devices with stellarator symmetry while preserving the zero frequency crossings of $(\mathbf{B} \cdot \nabla)$ parallel gradient operator. Equation (3.15) can be represented for different poloidal (m) and toroidal (n) mode numbers as a symmetric matrix eigenvalue equation after using defined $\mathbf{B} \cdot \nabla$, $|\nabla\psi|^2$, E_ψ, and multiplying by $\sqrt{g}\,\cos(m\theta - n\zeta)$ and finally averaging over flux surface.

$$\omega^2 \overleftrightarrow{A}\, \vec{x} \;=\; \overleftrightarrow{B}\, \vec{x} \tag{3.18}$$

where $\vec{x}$ is a vector having different components of E_ψ and $\mathbf{A}$, $\mathbf{B}$ both are symmetric matrices. Equation (3.18) provides the Alfvén continuum structures by finding $\vec{x} = \left[E_\psi^{m1,n1}, E_\psi^{m2,n2}, E_\psi^{m3,n3}, \cdots \right]^T$ and ω^2 eigenfrequency. In STELLGAP, Equation (3.18) is computed for all the relevant modes numbers (m, n) using the DGEGV routine from the IBM ESSL library.

Incompressible limit (Extended STELLGAP)

This section describes the mathematical model used for the calculation of Alfvén and Alfvén-acoustic continuum structures for the three dimensional systems. In this section

a mathematical description and procedure to solve these equations for a general 3D toroidal system is elaborated.

To investigate the full continuum spectrum of ideal MHD, an extension of the STELLGAP solver [36] with slow-sound wave coupling [41] has been used. Computation of the Alfvén continua with the coupling of slow-sound and Alfvén waves is viewed as obligatory due to the low frequency oscillations in the experimental observations. Three dimensional reduced MHD equations with the inclusion of parallel compressibility and coupling Alfvén and magneto-acoustic waves for low beta toroidal plasmas have been derived [42] for finite geodesic curvature of the magnetic field lines. The curvature K_s of field lines is responsible for coupling between these two waves, since at vanishing K_s the two waves decouple.

The inclusion of parallel compressibility into the system of equations allows us to investigate, in addition to the shear Alfvén mode, the acoustic, geodesic acoustic and coupled acoustic-shear Alfvén modes. These effects of compressibility are expected to set a minimum frequency range at rational surfaces ($k_\parallel = 0$) for the continuum. Following the approach of [43], the derived system of equations [42] is transformed into an eigenvalue system in the extended STELLGAP code [44, 45]. This eigenvalue system can be written as,

$$\left(\mu_0\rho_m\omega^2\frac{|\vec{\nabla}\psi|^2}{B^2} + \vec{B}\cdot\vec{\nabla}\left[\frac{|\vec{\nabla}\psi|^2(\vec{B}\cdot\vec{\nabla})}{B^2}\right]\right)\xi_s + \gamma p K_s(\vec{\nabla}\cdot\vec{\xi}) = 0 \tag{3.19}$$

$$K_s\xi_s + \left[\frac{\gamma p + B^2}{B^2} + \frac{1}{\mu_0\rho_m\omega^2}\gamma p(\vec{B}\cdot\vec{\nabla})\frac{(\vec{B}\cdot\vec{\nabla})}{B^2}\right](\vec{\nabla}\cdot\vec{\xi}) = 0 \tag{3.20}$$

In both equations, $(\vec{\nabla}\cdot\vec{\xi})$ is the plasma compressibility, magnetic surface displacement is $\xi_s = \vec{\xi}\cdot(\vec{B}\times\vec{\nabla}\psi)/|\nabla\psi|^2$ and $\vec{\nabla}\psi = N_{fp}F'_p/2\pi\vec{\nabla}s$, where ψ is the toroidal flux, N_{fp} is field-period and F'_p is derivative of the poloidal flux with respect to normalized toroidal flux s per period. K_s is the geodesic curvature of the background magnetic field given by,

$$K_s = 2\vec{\kappa}\cdot\left(\vec{B}\times\frac{\vec{\nabla}\psi}{B^2}\right) \text{ with } \quad \vec{\kappa} = \left(\vec{b}\cdot\vec{\nabla}\right)\vec{b} \quad \text{and} \quad \vec{b} = \frac{\vec{B}}{B} \tag{3.21}$$

Equations (3.19) and (3.20) are solved as a coupled system, expanding the unknowns in a Fourier series in poloidal (m) and toroidal (n) mode numbers. This leads to a matrix eigenvalue equation:

$$\omega^2 \overleftrightarrow{A}\,\vec{x} \;=\; \overleftrightarrow{B}\,\vec{x} \tag{3.22}$$

where $\vec{x}$ is a vector containing the Fourier components of ξ_s and $\vec{\nabla}\cdot\vec{\xi}$. With this set of equations, the Alfvén and Alfvén-sound continuum is computed by STELLGAP for all relevant mode numbers (m, n) using the DGEGV routine from the LAPACK library.

Equation (3.22) is solved in straight field line Boozer coordinates. The use of straight field line coordinates preserves the zeros of the $\mathbf{B}\cdot\nabla$ operator when coupled with a Fourier series representation of $\vec{\nabla}\cdot\vec{\xi}$ to avoid the presence of singularities due to the compressibility effects. The unknowns ξ_s and $\vec{\nabla}\cdot\vec{\xi}$ are expanded in a Fourier series over poloidal and toroidal angles, along with the coefficients in Equations (3.19) and (3.20). Series resulting from the convolution of these product series is multiplied by the individual Fourier test functions and integrated over each flux surface. This results in block tridiagonal matrices with the block size equal to the number of Fourier modes. An eigenvalue problem is then solved for each flux surface. A wide range of the Fourier modes is implemented to cover the extended spectrum of shear Alfvén, acoustic and coupled acoustic-shear Alfvén continua.

3.3.2 Alfvén eigenmode solver (AE3D) for 3D toroidal systems

For the discrete modes structures with radial extent investigations, a clustered frequency model [37], i.e. the AE3D code in low β limit has been employed. AE3D is an eigenvalue code, which computes Alfvén eigenmodes of finite radial extent along with their eigenfrequencies in 3D equilibria using reduced MHD model for the shear Alfvén waves in toroidal plasmas. As discussed in section 3.1, the basic equations in reduced MHD model are the two fundamental laws, i.e. the ideal MHD Ohm's law and the 3D vorticity equations which lead to an eigenvalue problem given below,

$$\omega^2\nabla\cdot\left(\frac{1}{{V^2}_A}\nabla\phi\right)+\left(\vec{B}\cdot\vec{\nabla}\right)\left[\frac{1}{B}\nabla^2\left(\frac{\vec{B}}{B}\cdot\nabla\phi\right)\right]+\nabla\zeta\times\nabla\left(\frac{\vec{B}}{B}\cdot\nabla\phi\right)\cdot\nabla\frac{J_{\|0}}{B}=0. \quad (3.23)$$

Where all perturbed quantities and ϕ are considered time-dependent as normal modes $e^{-i\omega t}$. AE3D solves this equation for the electrostatic potential ϕ of the eigenmodes. It is an identical expression to the Equation (3.3), here first term provides an inertia and second term is about the field-line bending. A large numbers of different types of the modes are possible because of the different poloidal and toroidal couplings instead of their singular radial structures therefore, a third ballooning term also becomes important in this formulation. To simplify Equation (3.23), it is multiplied by a trial function $\tilde{\phi}$ and integrated over the plasma volume. The resulting equation is solved

using a Galerkin approach, where ϕ and $\tilde{\phi}$ are expanded in a finite element (in radius) and Fourier series (in poloidal/toroidal angles) representation. This mathematical exercise results in a generalized matrix eigenvalue equation as,

$$\mathbf{F}\mathbf{y} = \lambda \mathbf{G}\mathbf{y} \tag{3.24}$$

where $\lambda = \omega^2$ is an eigenvalue and $\mathbf{F}$ and $\mathbf{G}$ are the block tridiagonal matrices. The eigenvector $\mathbf{y}$ is a column vector composed of the Fourier components of potential for each flux surface as, $\mathbf{y} = \left[{\phi_{\rho 1}}^{m1,n1}, {\phi_{\rho 1}}^{m2,n2}, \cdots, {\phi_{\rho 2}}^{m1,n1}, {\phi_{\rho 2}}^{m2,n2}, \cdots\right]^T$. AE3D can solve the eigenvalue equation (3.24) fully or partially. While it is time consuming to solve for the full spectrum of modes, a partial solution can be invoked by providing a seed gap frequency around which a cluster of the modes can be found. AE3D achieves faster performance for the partial solution by pre-specifying an eigenvalue (frequency) for the eigenmodes search as a subset of all eigenvalues using a Jacobi-Davidson style QZ (JDQZ) algorithm [46]. Instead of computing all the eigenvalues, JDQZ computes just a subset, allowing for much faster run times. The target frequency is generally chosen to be a gap frequency of interest from STELLGAP simulations.

Relationship among different parameters

The surface displacement ξ_s used in Chapter 2, the electric field E_ψ and the potential ϕ used in STELLGAP and AE3D codes respectively are all closely related to one another. There are all perturbed wave quantities. The electric field and potential are related through a spatial gradient operator as $E_\psi = -\nabla\phi$. In terms of the flux coordinates ψ, θ, and ζ, the electric field is related as,

$$E = -\left(\frac{\partial\phi}{\partial\psi}\nabla\psi + \frac{\partial\phi}{\partial\theta}\nabla\theta + \frac{\partial\phi}{\partial\zeta}\nabla\zeta\right). \tag{3.25}$$

The plasma displacement and electric field are related through the ideal MHD Ohm's law,

$$\mathbf{E} = -\frac{\partial\xi}{\partial t} \times \mathbf{B}. \tag{3.26}$$

Assuming time dependence and searching for the covariant component of electric field the Equation (3.26) gives, $E_\psi = i\omega\xi_s$, where we have used $\xi_s = \xi \cdot (\mathbf{B} \times \nabla\psi)/|\nabla\psi|^2$. Thus the relationship between the three different representations of the eigenmodes is as follows,

$$E_\psi \sim -\frac{\partial\phi}{\partial\psi} \sim i\omega\xi_s. \tag{3.27}$$

Chapter 4

Modelling of Steady and Chirping Alfvén eigenmodes in TJ-II plasmas

The properties of hydrogen Neutral Beam Injection (NBI) driven Alfvén eigenmodes (AEs) in the TJ-II flexible heliac are investigated using a reduced MHD model coupled to a realistic MHD equilibrium. The simulation results of AEs frequency and radial localization are found to be broadly consistent with experimental observations. The simulation results show that an AE with the same poloidal and toroidal harmonics persists under small variations in on-axis iota values, which is consistent with the experimental observations.

This work has been published in:

[47] **A. Rakha** et al., Modelling of beam-driven Alfvén modes in TJ-II plasmas, *Nuclear Fusion* **59** 056002, 2019.

4.1 Overview of Alfvén modes in TJ-II plasmas

Fast particle driven Alfvénic instabilities can have a crucial impact on the efficient heating of burning fusion plasmas. Stellarators are disruption-free steady-state helical devices aiming at sustained magnetic fusion power. To solve the problem of plasma self-heating with fusion-born alpha particles, the transport properties of the alpha particles must be known with a high level of confidence. Alfvén eigenmodes (AEs) driven unstable by fast particles represent a significant uncertainty in predicting the transport of alpha particles. They must be investigated in detail in present-day experiments since they may lead to losses of fast ions on plasma-facing components (PFCs) and decrease the ignition margin. Modelling studies of AEs in three-dimensional (3D) magnetic fusion systems are of primary importance due to observed 3D effects such

as coupling effects across different toroidal mode numbers in both tokamaks [22] and stellarators [48]. The calculation of Alfvén continuum and eigenmode structures are the first steps to take in order to compare theory and experiment for the Alfvén stability and confinement of energetic particles (EPs), enabling comparisons of modelling and experimental results to assess the validity of the AE physics models. Among the 3D magnetic fusion devices, the physics of AEs in stellarators is quite different from toroidally axisymmetric devices such as tokamaks due to different mode couplings and mode families corresponding to the number of field period (N_{fp}) in the toroidal direction of stellarators.

A number of numerical tools of varying complexity and approaches have been developed to investigate Alfvénic instabilities and wave-particle interaction in 3D geometries. For 3D linear ideal MHD continuum studies, the COBRA code [13] solves linear ideal MHD in Boozer coordinates and CONTI code [49] computes the coupling between Alfvén and sound waves in stellarator plasmas. For the investigations of properties of AEs and interaction with EPs in 3D magnetic fusion systems the CKA code [50] based on reduced MHD and finite Larmor radius effects and the BOA code [13] also based on a reduced-MHD model solving an eigenvalue problem with symmetric matrices have been developed. In this chapter, for 3D flexible heliac TJ-II plasmas, the shear Alfvén continuum calculations are performed with the STELLGAP code [36] based on the theoretical description given in [38]. The analysis of AEs is carried out with the AE3D code [37], a clustered frequency solver for the computation of eigenmodes centered on a specified target frequency. The centered frequency algorithm of the AE3D code is based on application of the Jacobi-Davidson method to a reduced MHD model [30]. This tool is more efficient by a factor of 10^2-10^3 in finding a subset of eigenmodes around a unique input frequency as compared with conventional methods. The 3D numerical tools employed for the investigation of AE instabilities have been successfully applied previously to investigate such instabilities in MST[51], LHD[52] and TJ-II [53, 54].

In the present work, the experimental findings in [5] have motivated the investigation of AE properties in a dynamic configuration scan (iota varies during discharge) of TJ-II stellarator. The iota, also known as rotational transform, in stellarators is proportional to the inverse of the safety factor q, where q is equal to the number of toroidal transits per single poloidal transit of a field line on a toroidal magnetic flux surface. During the iota scan obtained by changing an external coil current, non-linear evolution of the beam-driven AEs changed from bursting amplitude-sweeping frequency to steady amplitude-steady frequency, and then back. The understanding of this behaviour is

of importance because it would have direct implications on the type of alpha-particle losses (pulsating or steady-state) in future 3D magnetic fusion systems.

This chapter is organized as follows: Experimental observations for the modelling of modes are given in section 4.2. Section 4.3 explains the equilibrium calculation for TJ-II dynamic discharges. Furthermore, the section 4.4 presents the simulation results for both iota ramp-down and ramp-up cases. Finally, section 4.5 includes a summary and concluding remarks.

4.2 Experimental Observations

TJ-II is a four field period (N_{fp}) = 4 flexible heliac with a low magnetic shear, equilibrium magnetic field $B_0 = 0.95$ T, major radius $R_0 = 1.5$ m and averaged minor radius $\bar{a} \leq 0.22$ m. The flexibility of TJ-II allows the investigation of the properties of AEs by setting-up static discharges, i.e. discharges with a magnetic configuration [55], as well as dynamic discharges, i.e. discharges with a time-varying configuration scan that shows a changing rotational transform profile [6]. In the TJ-II experiments considered here, fast hydrogen ions are introduced in hydrogen plasmas by neutral beam co-injection, tangential to plasma axis (zero tangential radius) with a beam energy $E_{NBI} = 30$ keV and injected power $P_{NBI} = 0.56$ MW. In both discharges, the NBI operates from 1100 to 1195 ms. These beam particles have a velocity of $V_{NBI} \sim 2.5 \times 10^6$ m/s satisfying $V_{NBI} \geq V_A/3$ where V_A is the Alfvén velocity. In these experimental conditions, the slowing time of fast protons on electrons is of the order of 30 - 40 ms and the characteristic time for pitch angle scattering is of the order of a few ms. The critical energy below which pitch angle scattering becomes dominant is about 10 keV.

In our investigations of AE properties in TJ-II, we focus on two low density ($\bar{n}_e = 1.0 \times 10^{19}\, m^{-3}$) L-mode discharges 29834 and 29839, for which $V_A = 5.12 \times 10^6$ m/s. In both discharges, coexisting chirping and steady Alfvénic modes are observed. The observed Alfvénic activity is shown in the corresponding spectrograms in figure 4.1 together with the zoom of observed modes revealing both chirping and steady modes. In discharges #29834 and #29839, the magnetic configuration was scanned dynamically, including iota profile, by varying the currents in the external coils during the discharges, keeping all the other experimental settings unchanged. In discharge #29839, the iota was ramped up, while in discharge #29834 the iota was ramped down. A heavy ion beam probe (HIBP) [53] was used to investigate AEs. The HIBP data show that modes are located around $\rho = 0.55$ and the frequencies of modes are around 295 kHz, where

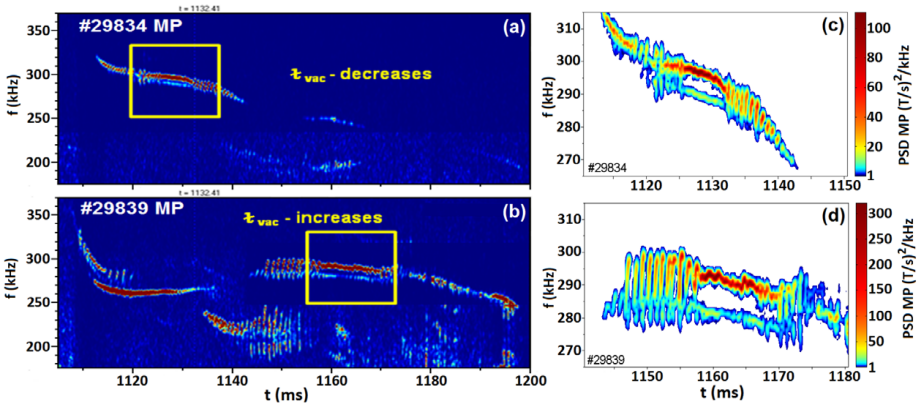

Fig. 4.1 Time evolution of AE modes with iota variation. (a) Poloidal field (B_{pol}) spectrograms, measured by a Mirnov Probe (MP) in shot #29834 with iota ramp-down. (b) Poloidal field (B_{pol}) spectrograms, measured by MP in shot #29839 with iota ramp-up. Figures (c) and (d) show zooms of (a) and (b), respectively, focusing in the time period of the mode transformation [5].

ρ is a normalized radial parameter defined as $\rho = \sqrt{\psi_{tor}}$ and ψ_{tor} is the normalized toroidal flux. The frequencies of these modes are confirmed with magnetic diagnostics and by using cross coherence between different signals.

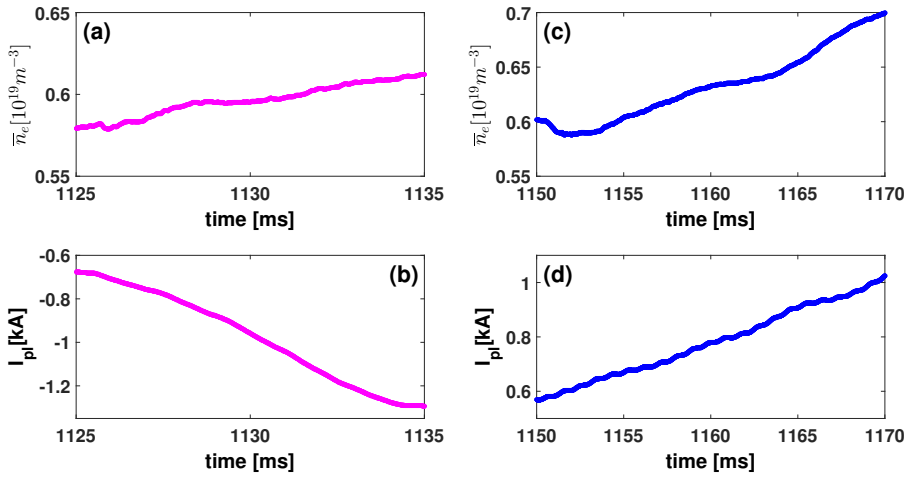

Fig. 4.2 The temporal evolution of plasma density averaged over the central chord line and plasma current. (a) central chord line averaged plasma density and (b) total plasma current for the discharge #29834 and (c) central chord line averaged plasma density and (d) total plasma current for the discharge #29839.

The temporal evolution of the central plasma density and current shows small variations during the time windows of mode transformation as shown in figure 4.2.

While these variations are small, they can contribute to the details of the mode behaviour. Their effects have been studied in detail in other TJ-II experiments [6]. In the numerical modelling presented in this chapter, we have only retained the dominant iota variation in time as described later in section 4.3 while assuming that the variation in the plasma density and current in time has a negligible effect on the mode behaviour. As an extension of this work, we are investigating the effect of plasma current on the iota profile and thereby on AEs. Preliminary results with monotonic and non-monotonic iota profiles caused by finite plasma current are presented [56].

4.3 Equilibrium for TJ-II dynamic plasmas

We start our investigations with equilibrium reconstructions for TJ-II discharges #29834 and #29839. We perform the equilibrium reconstruction calculations using the VMEC code [31] by taking into account the appropriate TJ-II magnetic geometries. VMEC constructs an equilibrium by employing a variational method to find a minimum of the system energy.

Since the experimental findings show a time evolution between chirping and steady types of AEs and back in both cases, we focus our analysis on a number of time slices that exhibit different mode activity in both discharges. The main part of our simulations is carried out for time slices t = 1130 and 1135 ms in discharge #29834, corresponding to steady and chirping modes, respectively, and for time slices t = 1150 and 1160 ms in discharge #29839, corresponding to chirping and steady modes, respectively. In the rest of the chapter, our discussion relates to the results for these time slices unless otherwise noted. However, we have also considered additional time slices to check whether the trends emerging from the modelling hold in general. In the following sections, we will clearly indicate when we are discussing the results of these additional time slices instead the time slices given above.

The TJ-II fixed-boundary equilibria have been reconstructed under experimental constraints for both discharges at the chosen times. The vacuum rotational transform ($\iota/2\pi$) profiles for the VMEC reconstructed equilibria based on experimentally selected magnetic configuration for both discharges at the selected times are shown in figure 4.3. Here, for each modelled equilibrium time slice, the input data has been averaged over a short 1 ms long time window. The resulting iota profiles increase monotonically in radius and range between $1.63 \geq \iota/2\pi \leq 1.76$.

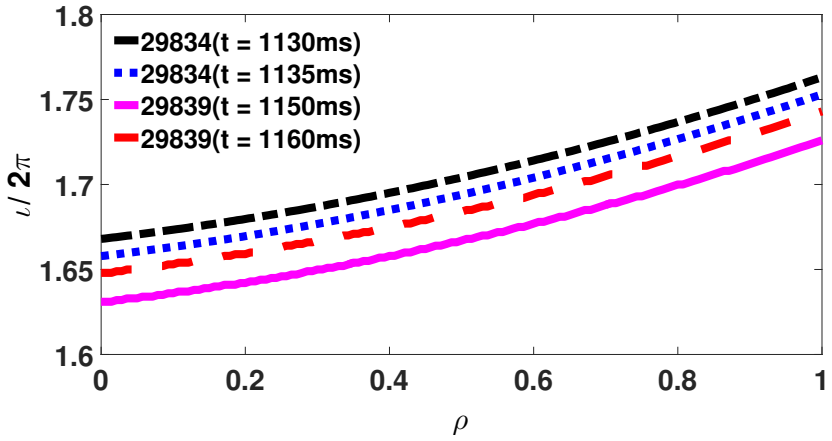

Fig. 4.3 Iota profiles for the four selected time slices for both iota ramp-up and ramp-down discharges. These iota profiles are calculated with the VMEC converged equilibrium.

4.4 Simulation results and discussions

After setting-up the plasma equilibrium using VMEC, the STELLGAP simulations were performed to compute the Alfvén continuum. For the dominant toroidal mode number (n), the results of shear Alfvén spectra are plotted for both discharges at the selected times. To illustrate the computed Alfvén eigenmode properties, the simulated electrostatic potential versus normalized radius from AE3D code are presented case by case.

4.4.1 Simulation results for the ramp-down of iota in TJ-II

Alfvén continua calculated by the STELLGAP code for the discharge #29834 at t = 1130 and 1135 ms are presented in figure 4.4, where the dominant toroidal mode number (n) is highlighted by colour coding. In both shear Alfvén spectra, there are clear gaps visible about 250-350 kHz, which are considered as an initial frequency target for the search of AEs. The AEs are computed with the AE3D code, and it is found that two prominent modes with m = 11 and n = 19 and m = 9 and n = 15 appear with different frequencies of 276 kHz shown in figure (4.5a) and 256 kHz figure (4.5b) at similar radial location $\rho = 0.65$ in the steady AE-frequency case. Likewise, in the chirping AE-frequency case, AEs with same mode numbers and higher frequencies of 292 and 287 kHz are found at radial location $\rho = 0.75$ as shown in figure 4.6. Comparison of results in the iota ramp-down case shows that there is a small increase in frequencies from the steady to chirping mode transition and the modes are also displaced radially

outwards. The observed frequency increase is explained by the decrease of the density at the outer radial positions.

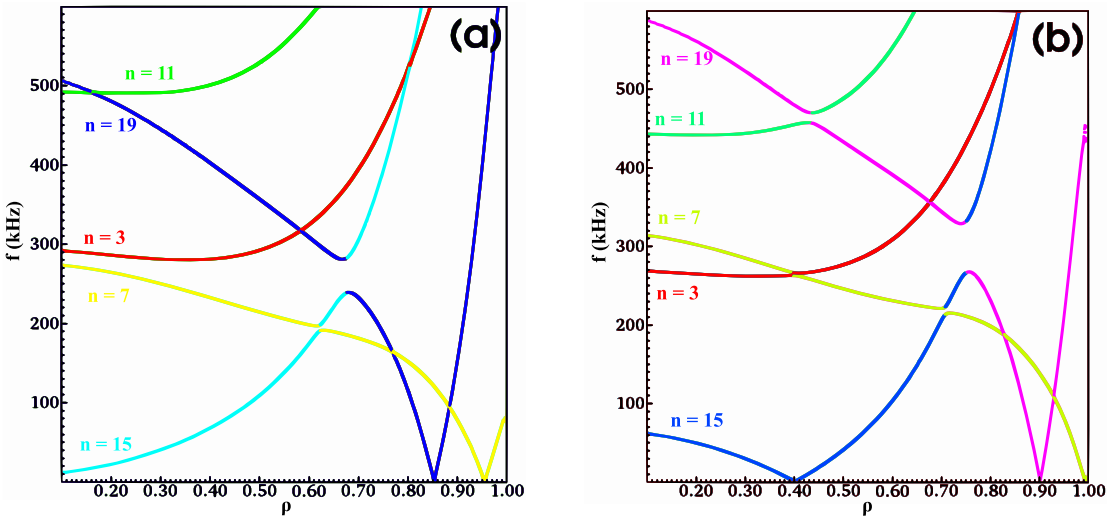

Fig. 4.4 Shear Alfvén spectra for discharge #29834. (a) Alfvén continuum structures for steady mode and (b) Alfvén continuum structures for the chirping mode.

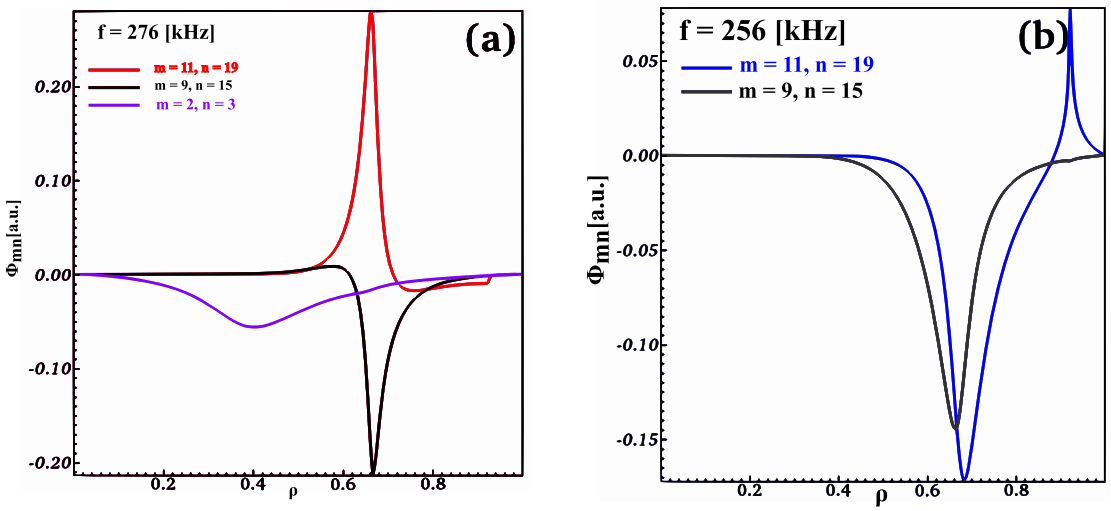

Fig. 4.5 Alfvén eigenmodes for the steady mode in discharge #29834. (a) An AE with three different sets of prominent mode numbers (m, n) having single dominant frequency 276 kHz and (b) AE with two different sets of prominent mode numbers (m, n) having single dominant frequency of 256 kHz.

The radial extent $\delta\rho$ of AEs was calculated as the Full Width at Half Maximum (FWHM) of the simulated potential structures. For both discharges, our results show that the radial extent of AEs shrinks from $\delta\rho = 0.11$ in the chirping phase to a

minimum of $\delta\rho = 0.04$ during the steady phase. Thus, it can be suggested that the modes calculated during steady phase are relatively more peaked than those in the chirping phase, however for some modes, $\delta\rho$ has no significant difference between the steady phase and the chirping phase. Simulations for an additional earlier time slice t

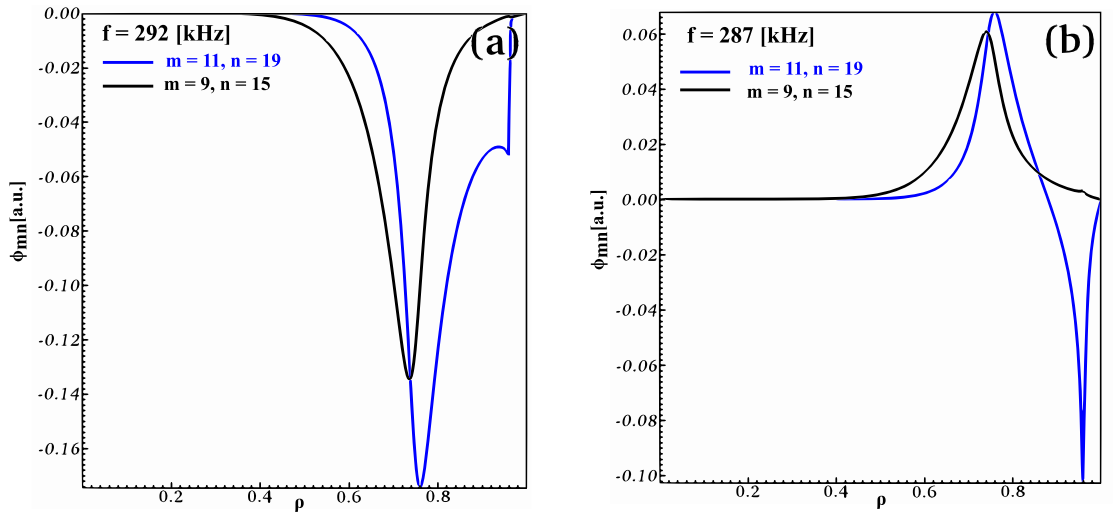

Fig. 4.6 Alfvén eigenmodes for the chirping mode in discharge #29834. (a) An AE with two different sets of prominent mode numbers (m, n) having single dominant frequency 292 kHz and (b) AE with two different sets of prominent mode numbers (m, n) having single dominant frequency of 287 kHz.

= 1125 ms show the same prominent modes as for the time slices t = 1130 and 1135 ms. At t = 1125 ms, the mode frequencies are 246 and 232 kHz and the mode is radially located at $\rho = 0.6$. In conclusion, according to our modelling results, when the iota is ramped down in discharge #29834 the prominent AE remains the same while its frequency increases slightly and it moves to larger ρ. The modelled evolution of the mode frequency is in agreement with experimental observations.

4.4.2 Simulation results for the ramp up of iota in TJ-II

In section 4.4.1, we have shown the results of ur modelling for the TJ-II discharge #29834 with the ramp down of the iota. In this section we consider TJ-II discharge #29839 with the opposite time variation in iota, i.e. iota ramp-up. Similar to discharge #29834, here we also compute the Alfvén continuum for discharge #29839 using STELLGAP at t = 1150 and 1160 ms exhibiting a chirping and steady mode, respectively. Figure 4.7 displays the calculated continua with different colours representing the different dominant toroidal mode numbers. The clear open gaps in the continuum

structures at the cross coupling of n = 17 and 13 can be seen in both cases ranging in the frequencies of 300 to 220 kHz with radial localization of $\rho = 0.7$ to $\rho = 0.6$. Again, the frequency change is explained by the lower densities at outer positions.

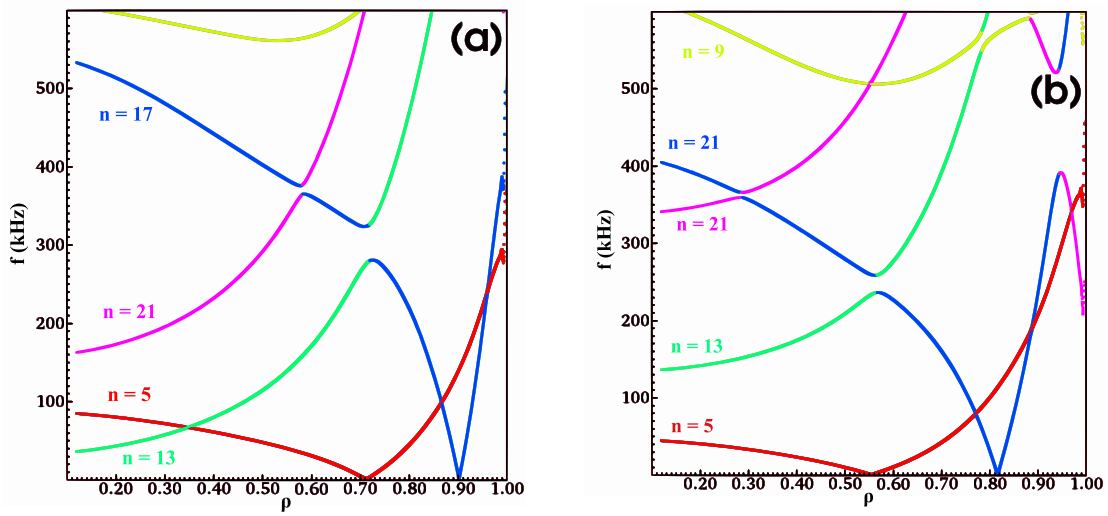

Fig. 4.7 Shear Alfvén spectra for discharge #29839. (a) Alfvén continuum structures for the chirping mode and (b) Alfvén continuum structures for the steady mode.

Again AEs are computed using the AE3D code and plotted in figures 4.8 and 4.9 for the chirping and steady modes respectively. It is interesting to note that in both cases the two observed modes remain the same, i.e. their mode numbers m = 10 and n = 17 and m = 8 and n = 13 are unchanged for the chirping and steady mode phases. However, there is a decrease in the modes frequencies from 289 and 316 kHz in the chirping case shown in figure 4.8 to 254 kHz in the case of steady mode shown in figure 4.9, explained by the higher density values at the mode position. Moreover, there is a radial inward movement of the mode from $\rho = 0.7$ to $\rho = 0.55$ when the AE structure changes from a chirping mode to steady mode. We consider the modes with m = 10 and n = 17 and m = 8 and n = 13 as the prominent modes consistent with experimental results, despite the slight decrease in their frequency from 289 to 254 kHz.

Similarly as for the case with the iota ramp-down, we have extended our simulations for discharge #29839 to an additional time slice t = 1170 ms with chirping AE activity and at higher iota value. At this time slice, our results show that there are also two different prominent modes. One of them having m = 8 and n = 13 is the same and the second one with dominant mode numbers m = 12 and n = 21 is unique as compared with the last two cases of discharge #29839. Both of these modes have the same frequency of 334 kHz which is relatively higher than the prior cases at t = 1150 and

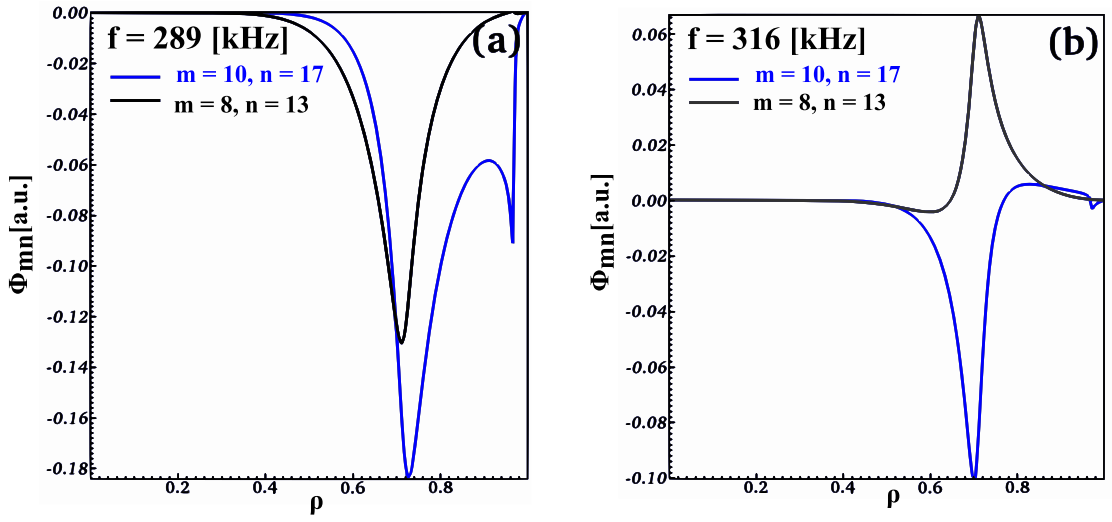

Fig. 4.8 Alfvén eigenmodes for the chirping mode in discharge #29839. (a) An AE with two different sets of prominent mode numbers (m, n) having single dominant frequency 289 kHz and (b) AE with two different sets of prominent mode numbers (m, n) having single dominant frequency of 316 kHz.

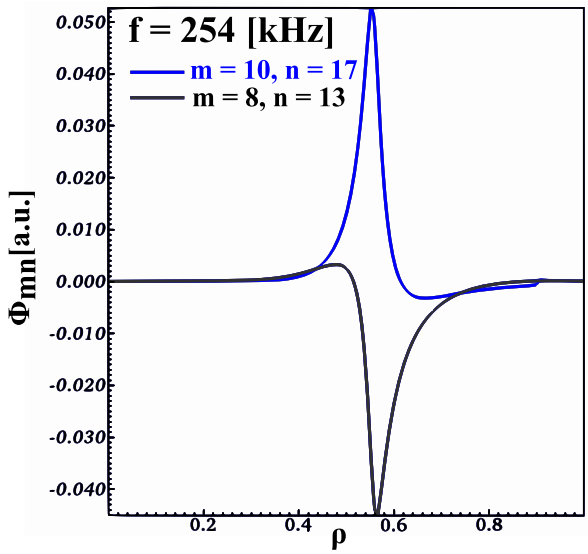

Fig. 4.9 Alfvén eigenmodes for steady mode in discharge #29839. An AE with two different sets of prominent mode numbers (m, n) having single dominant frequency 254 kHz.

1160 ms. These modes are located radially further outwards at $\rho = 0.8$ than the modes at the previous time points.

We have also carried out simulations to check the Alfvénic character of the modes. For this purpose we have performed simulations at different electron densities. We

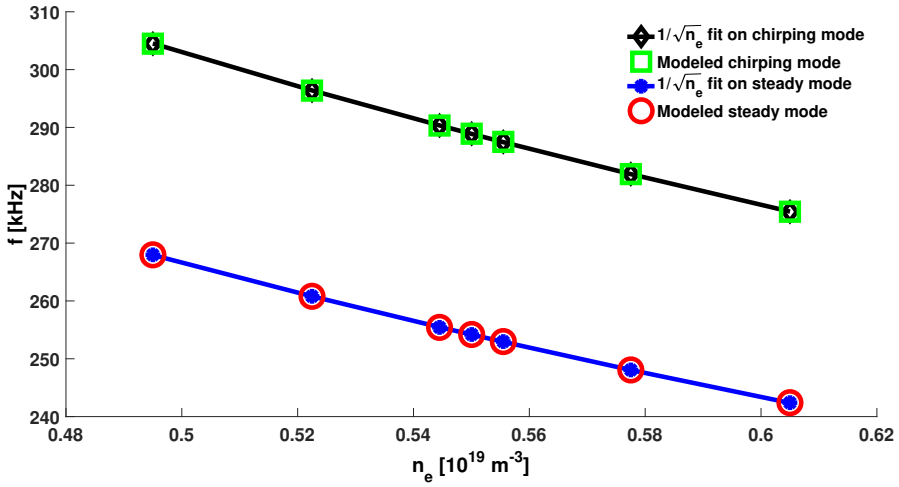

Fig. 4.10 Frequency of the prominent modes as given by the AE3D code for discharge #29839 as a function of the electron density compared with the Alfvénic density scaling of the frequency as $1/\sqrt{n_e}$.

find that the calculated mode frequency scales as $1/\sqrt{n_e}$, which confirms the Alfvénic character of the mode (c.f. Figure 4.10)

4.5 Summary and conclusions

Our 3D modelling results for dominant modes are summarized in table 4.1. We find that the reduced MHD simulations agree with the mode characteristics as measured by the heavy ion beam probe (HIBP) diagnostic in discharges #29834 and #29839 at the specified times. The HIBP data show that modes are located around $\rho = 0.55$ and the frequencies of modes are around 295 kHz. Good agreement between simulations and experiments is found in the frequency and radial location of the modes.

Discharges	**Modes** $(\mathbf{m}, \mathbf{n})$	**Frequency(kHz)**	**Radial location**(ρ)
#29834	$(11, 19)$ & $(9, 15)$	276 (s), 256 (s)	0.65
		292 (c), 287 (c)	0.75
	$(2, 3)$	272 (c), 275 (s)	0.40 , 0.45
#29839	$(10, 17)$ & $(8, 13)$	316 (c), 289 (c), 254 (s)	0.70 , 0.70 , 0.55
	$(8, 13)$	251 (s), 334 (c)	0.55 , 0.80

Table 4.1 Summary of simulation results for the AE mode localizations and frequencies. Here, s and c correspond to the steady and chirping types of modes, respectively.

Simulations show that the case with iota ramping down in time moves the modes towards the outboard side while a ramp-up in iota pushes them to the inboard side. The inward movement of the modes suggests that EP confinement is improving. Moreover, the AE frequencies show a ramp-up and ramp-down trend for iota ramp-down and ramp-up, respectively. The combination of the toroidal (n) and poloidal (m) mode numbers at different iota windows or, equivalently, at different time slices of discharge enhances the confidence of appearance of same mode, in agreement with the experimentally observed co-existence of the mode.

Chapter 5

Modelling of Alfvén cascade modes in stellarator plasmas

In this chapter an explanation of the steps to model Alfvén cascades is followed by the detailed analysis of the obtained results for the TJ-II plasmas. In TJ-II the frequency sweeping modes in the Alfvén frequency range have been observed [6]. Modelling of the observed phenomenon reveals the important features of the modes and their association with the magnetic rotational transform (iota), which are the key outcomes of these investigations.

This work has been published in:

[56] **A. Rakha** et al., Modelling of Alfvén cascades in NBI heated stellarator plasmas, *45th EPS Conference on Plasma Physics* **42A** P4.1004, 2018.

[57] **A. Rakha** et al., Modelling of Alfvén cascade modes in stellarator plasmas, *Submitted to Nuclear Fusion*

5.1 Overview

Alfvén frequency sweeping modes in stellarator plasmas with normal and reversed-shear rotational transform are modelled using a reduced MHD model. We focus on a TJ-II dynamic discharge in which a sequence of frequency sweeping modes with a frequency sweeping range from 20 kHz to 140 kHz (**A.V. Melnikov** et al. 2014 Nuclear Fusion **54** 123002) has been observed. We find that for the normal shear iota profile a lower number of modes are present centred around 150 kHz of frequency while for radially extended low shear non-monotonic (NM) iota profiles, an extended spectrum of Alfvénic modes is present covering a wider range of frequency from 115 to 295 kHz. Similarly a large number of discrete modes appear for relatively strong negative shear NM iota

profiles having a frequency range from 36 to 216 kHz. Results for the NM iota profiles with protracted discrete modes are in agreement with the extended frequency sweeping experimental findings. With strong negative shear one of the prominent modes (m = 7, n = 10/11) becomes narrower in radial width. An iota profile with strong negative shear and lower ι_{min} can therefore be considered more favourable for Alfvén eigenmode (AE) stability. Comparison of this mode's frequencies calculated using a standard dispersion relation and modelled through AE3D shows an agreement with the selection of ι_{min} values which supports the MHD spectroscopy calculations.

5.2 Introduction

Alfvénic instabilities driven by externally generated energetic particles (EPs) for sustainable plasma heating and fusion-born alpha particles are of primary importance in fusion plasmas. They can deteriorate plasma heating and the confinement of fast particles, cause high heat fluxes on plasma facing components and decrease ignition margin by transporting out the fusion products [58]. Reversed Shear Alfvén eigenmodes (RSAEs), also called Alfvén cascades (ACs) [17, 18, 59, 60] are a special type of Alfvénic instability that arises in the presence of a reversed-shear rotational transform profile. Recently, the interest in reversed magnetic shear plasmas has increased significantly because of the improved confinement conditions with the formation of internal transport barriers (ITBs) [61] and magnetohydrodynamic (MHD) stability [62, 63]. In addition, the ACs provide a unique diagnostic opportunity for the experimental estimation of the safety factor (q) profile in tokamaks [18–20, 64] and rotational transform (1/q) profiles, also called the iota (ι) profile, in stellarator plasmas [21, 65] because the time evolution of mode frequencies is easily recognizable via MHD spectroscopy. The rotational transform is defined as the number of poloidal transits per single toroidal transit of a field line on a toroidal magnetic flux surface. MHD spectroscopy provides spectral measurements of the Alfvénic activity and serves as a diagnostic tool for the plasma by providing the temporal evolution of the safety factor or the rotational transform. It has similarity to atomic spectroscopy and helioseismology for investigations of the internal structure of the sun. The magnetic shear defines variations in the direction of magnetic field, and in the presence of nested magnetic flux surfaces it is defined as the radial gradient of the rotational transform. This structure is important for plasma confinement properties and large-scale MHD instabilities.

ACs typically exhibit a quasiperiodic pattern of upward or downward frequency sweeping as the local minimum of the inverse safety factor changes in time. Due to the

time variation of the iota profile in stellarator plasmas, a rich spectrum of Alfvénic instabilities has been found. For such instabilities the frequency changes very rapidly in time. This is referred to as frequency sweeping when these rapid variations in frequency are driven by changes in the equilibrium e.g. by changes in the iota profile [16]. In a reverse-shear (RS) configuration, the upward sweep of AC frequency at $q_{min} > m/n$ may approach the toroidal Alfvén eigenmode (TAE) frequency as the local minimum of iota drops in time while a downward sweep at $q_{min} < m/n$ can lead to the geodesic acoustic mode (GAM), where $n(m)$ is the toroidal (poloidal) mode number [59]. The ACs resemble Global Alfvén eigenmodes (GAE) since both are cylindrical modes, typically dominated by a single poloidal mode, and since both may exist just below or above the extrema of the shear Alfvén continua. On the contrary, the reverse-shear (RS) modes localize around the extrema of the continua, while the GAEs have radially extended structures [66].

The investigation of EP instabilities is an important goal in three-dimensional (3D) fusion systems since 3D magnetic perturbations are present to some extent in all toroidal magnetic fusion devices with the presence of external symmetry breaking perturbations [**?**] and non-axisymmetric effects [**? ?**]. As stellarators are inherently 3D fusion devices, investigations and comprehensive understanding of such instabilities in stellarator plasmas would certainly be beneficial for future fusion devices. RSAEs have been observed in almost all working fusion devices including stellarators. In the Large Helical Device (LHD), RSAEs are observed with non-monotonic rotational transform profiles created with counter neutral beam (NB) drive [21]. In the TJ-II stellarator frequency sweeping modes are observed also with NB injection [6]. Global linear gyrokinetic simulations of reversed-shear LHD discharges [67] have been used to study their properties. Since the temporal evolution of RSAEs is well described by ideal MHD theory, a reduced MHD model [30] is used to investigate the experimentally observed frequency sweeping phenomena and model their properties over varying ι_{min}. This model solves reduced MHD equations as an eigenvalue problem by ignoring the fast-scale perpendicular dynamics in a 3D toroidal system. Previously, this model has been applied for the modelling of beam-driven EP instabilities in stellarators [47, 67], Reversed Field Pinch (RFP) [51] and tokamaks [16]. Initial modelling results of ACs for the TJ-II stellarator plasmas [56] suggest that the non-monotonic (NM) iota profile supports the experimental observations.

The frequency sweeping modes have been observed in TJ-II stellarator plasmas, and their frequencies have been modelled using a mathematical ansatz for the iota profile as discussed in [6]. Despite this promising approach and the evidence of following an

Alfvénic frequency dependence of plasma density ($1/\sqrt{n_e}$), the fast frequency sweeping of the observed modes remains unexplored. In this paper, we model the observed frequency sweeping modes in TJ-II. These modelling results based on a non-monotonic (NM) iota profile confirm the Alfvénic behavior of observed modes and also predict the associated frequency sweeping phenomenon. We provide modelling results of AEs with normal, radially extended low shear NM iota profiles and further extension with the strong shear centrally localized NM iota profiles. The existence of large number of modes with frequencies higher than GAEs and radially well localized mode structures in the presence of NM iota profiles support the experimental observations of frequency sweeping.

This chapter is organized as follows. In section 5.3 the experimental results for TJ-II plasmas with frequency sweeping modes are provided. The section 5.4 describes an equilibrium reconstruction for the modelled iota profiles. In section 5.5, simulation results for both the Alfvén continuum and mode structures are discussed, and section 5.6 gives a summary and conclusions of the findings.

5.3 Experimental Observations

TJ-II is a four-field period flexible heliac with a major radius $R = 1.5$ m, an averaged minor radius $\bar{a} \leq 0.22$ m, and an equilibrium magnetic field of $B_0 = 0.95$ T. Experiments have been performed at the TJ-II stellarator to investigate the up or down frequency sweeping of NBI-driven Alfvén eigenmodes by varying the magnetic configuration during a discharge. The magnetic configuration has been linearly varied over a time period of 60 ms by changing currents in helical coils [68]. The variations in iota profile appear due to the variations in plasma current for different reasons (skin current, dynamic configuration, changes in vertical/poloidal field, electron cyclotron current drive [69] and neutral beam current drive). It has been observed that the changes in the iota profile significantly vary the AE mode frequency, while the mode location does not change much if these variations are relatively small.

A typical TJ-II discharge scenario with the dynamic magnetic configuration is shown in Figure 5.1 [6]. In this scenario, the plasma is initially created and heated with off-axis electron-cyclotron resonance heating (ECRH); following this the plasma is heated with neutral beam injection (NBI) only. After the switching-off of ECRH, the plasma is sustained only with NBI heating, which also increases the plasma density.

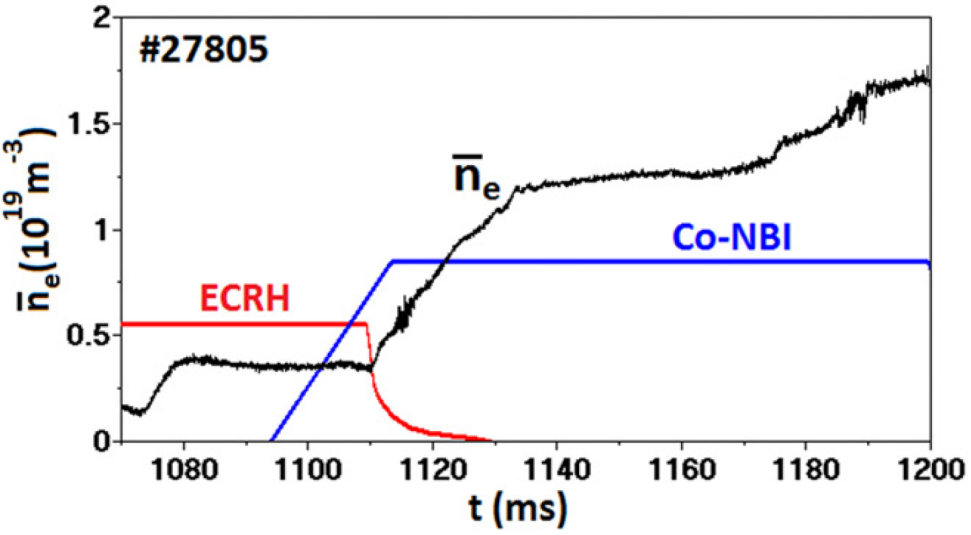

Fig. 5.1 A typical TJ-II discharge scenario and the corresponding line averaged plasma density evolution [6]

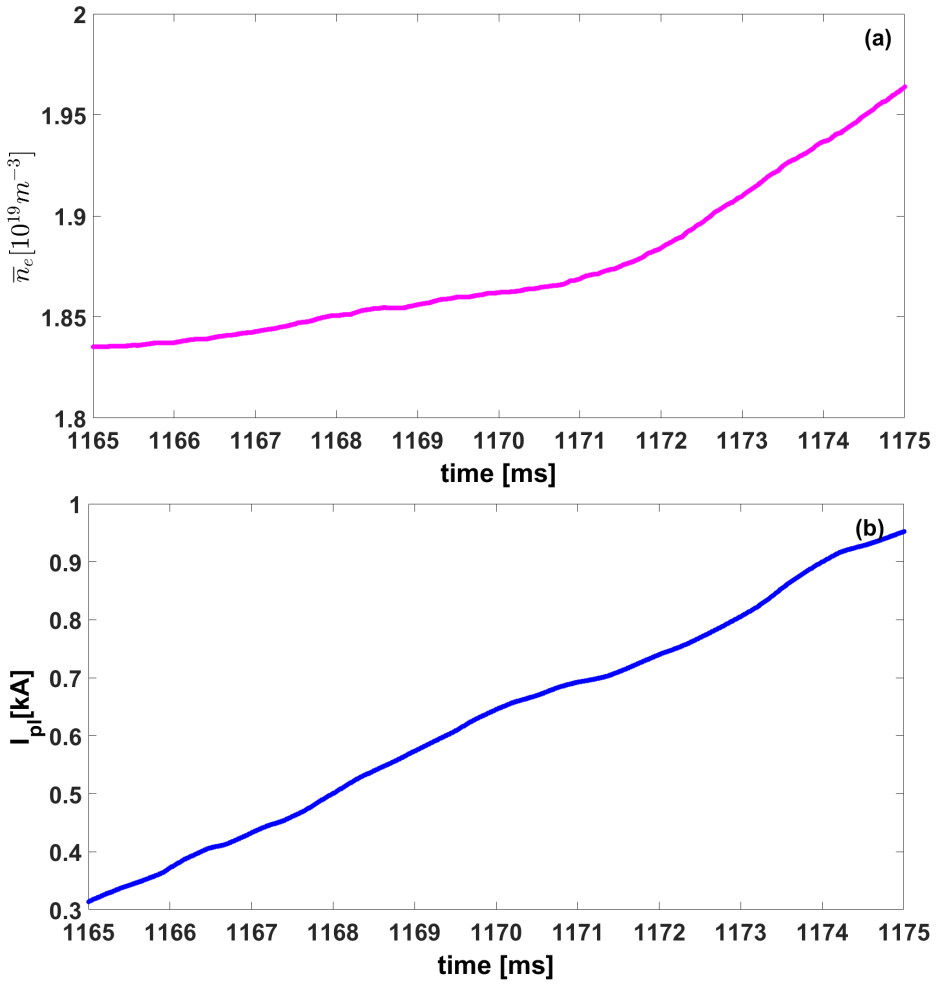

Fig. 5.2 Temporal evolution of (a) the plasma density and (b) current for TJ-II discharge #27804

We focus our analysis on TJ-II discharge 27804 where Alfvénic activity has been observed with downwards frequency sweeping at t = 1165-70 ms. The frequency sweeping modes are clearly visible in the plasma density spectrogram shown in Figure 5.3. The range of this fast downward frequency sweeping is from 150 kHz to 25 kHz in the time span of only $\sim$ 10 ms. This observed sharp frequency sweeping at nearly constant line averaged density $\bar{n_e} = 1.8 \times 10^{19} m^{-3}$ from t = 1165 to 1170 ms (Figure 5.2a) is expected because of the time varying iota profile induced through the relatively small variation in plasma current (Figure 5.2b). The cross-coherence of Heavy Ion Beam Probe (HIBP) and bolometer signals shows that the observed modes are radially extended and they are located around ($\rho \approx 0.7$). Here, ρ is a radial parameter which is defined as $\rho = \sqrt{\psi_t}$, where ψ_t is normalized toroidal flux.

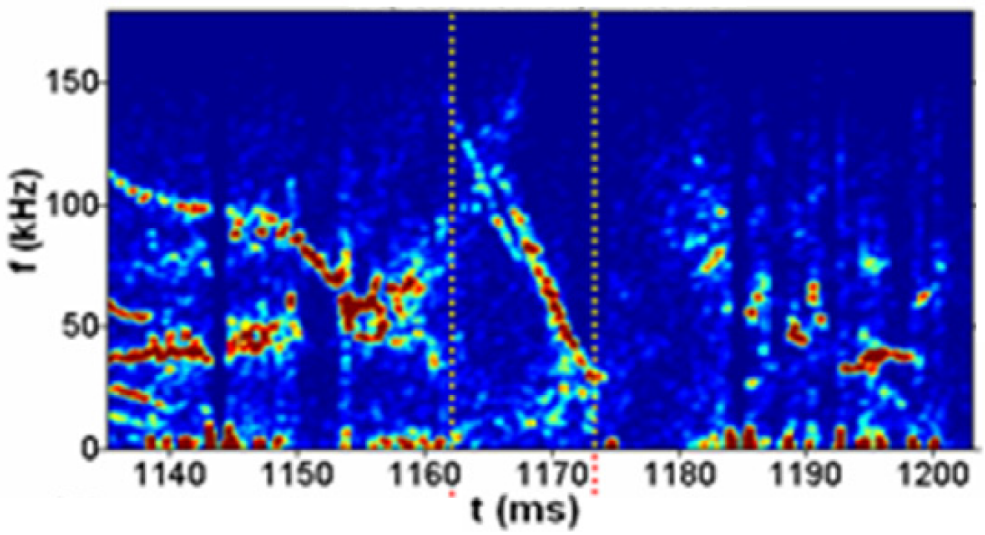

Fig. 5.3 Plasma density spectrogram measured by HIBP for TJ-II discharge #27804 [6]

In discharge 27804, the plasma current evolves in time during the time window ($\sim$ 10 ms) of mode sweeping as shown in Figure 5.2. These variations are $\Delta I_p = 0.35$ kA from t = 1165 to 1170 ms which can contribute to the details of the mode behaviour. Experimentally the effects of this variation on the modes have been studied in detail in reference [6]. In order to correctly model the experimental results we have carefully employed the experimental plasma density and measured on-axis iota value for the monotonic and non-monotonic iota profiles in our modelling calculations as discussed in section 5.4.

5.4 Equilibrium reconstruction

In the first step, MHD equilibrium calculations have been performed using the experimental magnetic geometry and plasma parameters for the TJ-II discharge 27804 at t = 1170 ms with an equilibrium solver VMEC [31]. VMEC iteratively solves the MHD model using a variational method to find a minimum of the system energy for the reconstruction of an equilibrium. It solves the MHD model assuming closed magnetic flux surfaces and, therefore, does not allow any formation of stochastic structures of the magnetic field.

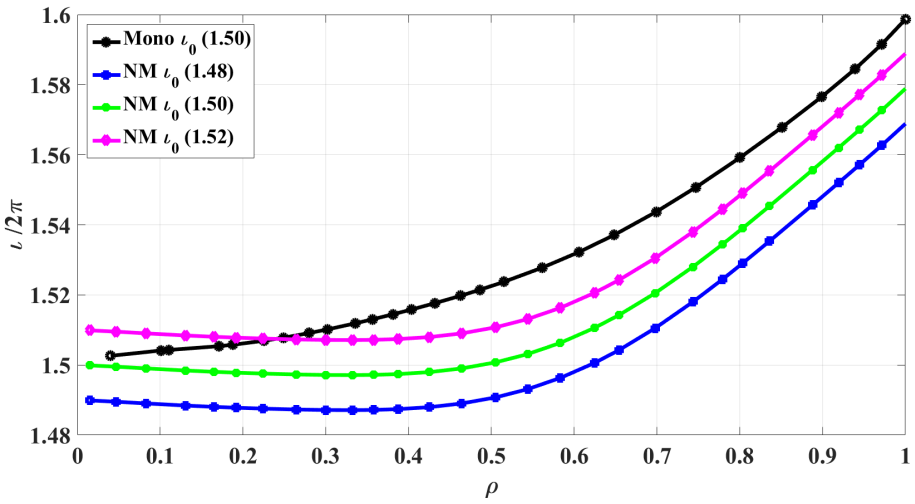

Fig. 5.4 Normal (monotonic) and radially extended low-shear non-monotonic (NM) rotational transform (iota) profiles for TJ-II discharge 27804 with an on-axis iota value of $\iota(0) = 1.50$.

When the frequency sweeping modes appeared in the TJ-II discharge 27804, the on-axis iota value $\iota(0)$ was determined around 1.5 [6]. Therefore, we have considered an on-axis iota of $\iota(0) = 1.50$ for the reconstruction of plasma equilibrium with normal (monotonic) and non-monotonic (NM) iota profiles. For the normal iota profile case, a linear iota profile is considered with $\iota(0) = 1.5$ for the reconstruction of fixed boundary MHD equilibrium to model the experimentally observed frequency sweeping modes. The Alfvén continuum and modal analysis given in section 5.5 with a small number of modes could not explain the experimentally observed frequency sweeping phenomenon. Therefore, we considered reversed shear NM iota profiles with radially extended low shear and centrally localized relatively strong shear regions.

TJ-II fixed-boundary equilibria with radially extended low-shear NM iota profile are achieved with $\iota(0) = 1.49$, 1.50 and 1.51 (see Figure 5.4). Extended low shear equilibria are computed to model a larger core area with reversed shear. Three distinct

values of $\iota(0)$ are considered to investigate how sensitive the results of the extended mode analysis are with respect to the on-axis iota value of the reversed shear iota profiles. A similar extended low shear region was observed with the neutral beam current drive (NBCD) in the Large Helical Device (LHD) [67] when Alfvénic activity is present. The normal and low-shear NM iota profiles we have considered range between $1.50 \geq \iota/2\pi \leq 1.6$. In these low shear NM iota profiles, the low shear region radially extends up to $\rho \approx 0.5$ with a minimum located around $\rho \approx 0.4$.

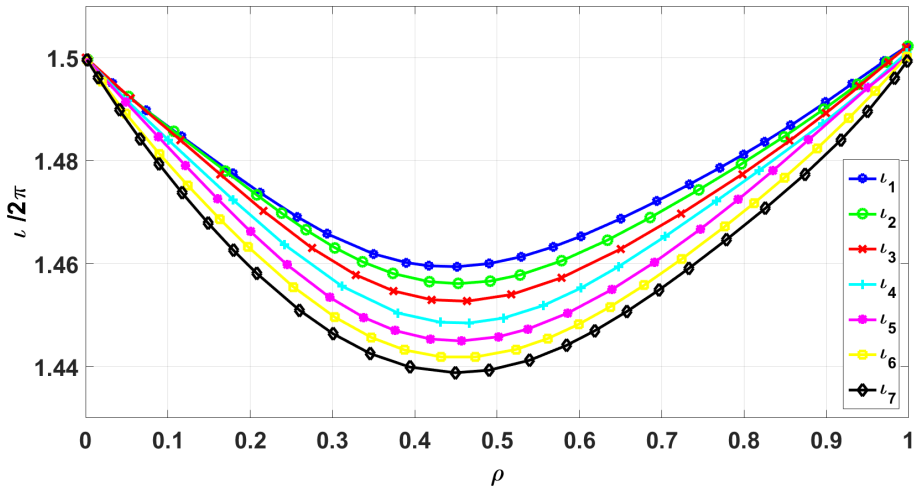

Fig. 5.5 Strong shear non-monotonic (NM) rotational transform (iota) profiles modeled for the TJ-II discharge #27804 with on-axis iota value $\iota(0) = 1.50$ and varying ι_{min} from 1.4388 to 1.4594 around $\rho = 0.45$.

ι_1	ι_2	ι_3	ι_4	ι_5	ι_6	ι_7
1.4594	1.4561	1.4527	1.4485	1.4450	1.4418	1.4388

Table 5.1 Minimum iota values i.e. ι_{min} for the strong shear NM iota profiles shown in Figure 5.5

To investigate the effects of strong shear, equilibrium calculations are performed by introducing strong shear in the iota profiles and keeping ι_0 and iota edge = 1.5. Seven similar strong shear NM iota profiles with varying ι_{min} shown in Table **??** radially localized around $\rho \approx 0.45$ as shown in Figure **??** are considered to investigate the ι_{min} effect on the modes. This set of strong shear NM iota profiles is selected so that ι_{min} remains lower than the 3/2 rational surface.

5.5 Simulation results

Following the plasma equilibrium reconstruction, Alfvén continuum spectra for the normal, radially extended low-shear NM and strong shear NM iota profiles are computed using the STELLGAP solver [36] and their detailed discussion is provided in section 5.5.1. The analysis of the Alfvén modes with the AE3D [37] code for all three types of iota profiles is provided in the section 5.5.2 which describes the nature of the modes, their prominent modes numbers, frequencies and radial localization.

5.5.1 Alfvén continuum spectra analysis

The observed frequency sweeping Alfvénic modes are modelled using reduced MHD simulations for the normal, low shear NM and strong shear NM iota profiles. In first step, in order to examine possible continuum gaps, the Alfvén continuum structures are calculated using STELLGAP [36]. These continuum calculations provide information on the possible formation of frequency gaps and the likely radial localization of the Alfvén modes at the gaps and extremum points in Alfvén continuum.

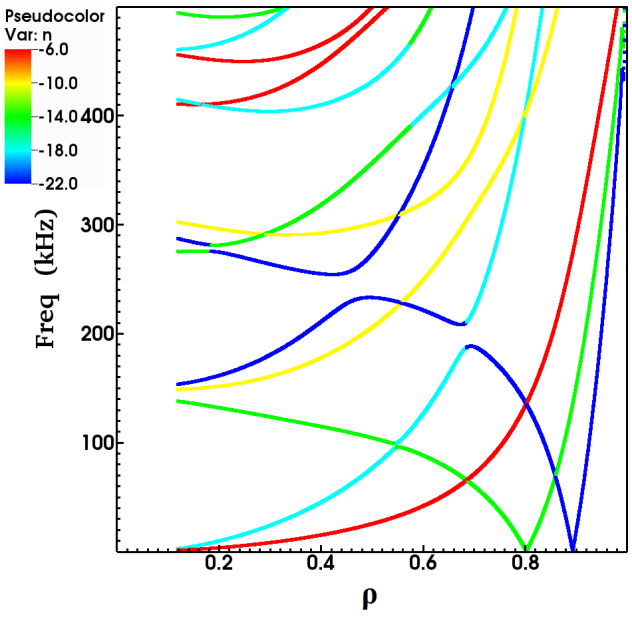

Fig. 5.6 Alfvén continuum structures for the normal/monotonic iota profile for discharge 27804. The color coding of continua represents the corresponding toroidal mode number (n).

Alfvén continuum structures for the normal iota profile are plotted in Figure 5.6. Figure 5.6 shows that the gaps form at frequencies of around 185 and 220 kHz and radially lie at ρ of 0.7 and 0.5 respectively. While there are some low-frequency extrema

present in these structures, due to their closed nature they are subject to the strong continuum damping, which inhibit low-frequency modes. Because of the limited gaps for the continuum calculated with the normal iota profile, this case is not useful for the possibility of a larger number of modes over an extended frequency range. Calculations with reverse shear NM iota profiles are therefore considered important for describing frequency sweeping modes which have been reported in reverse shear helical plasmas [21, 67].

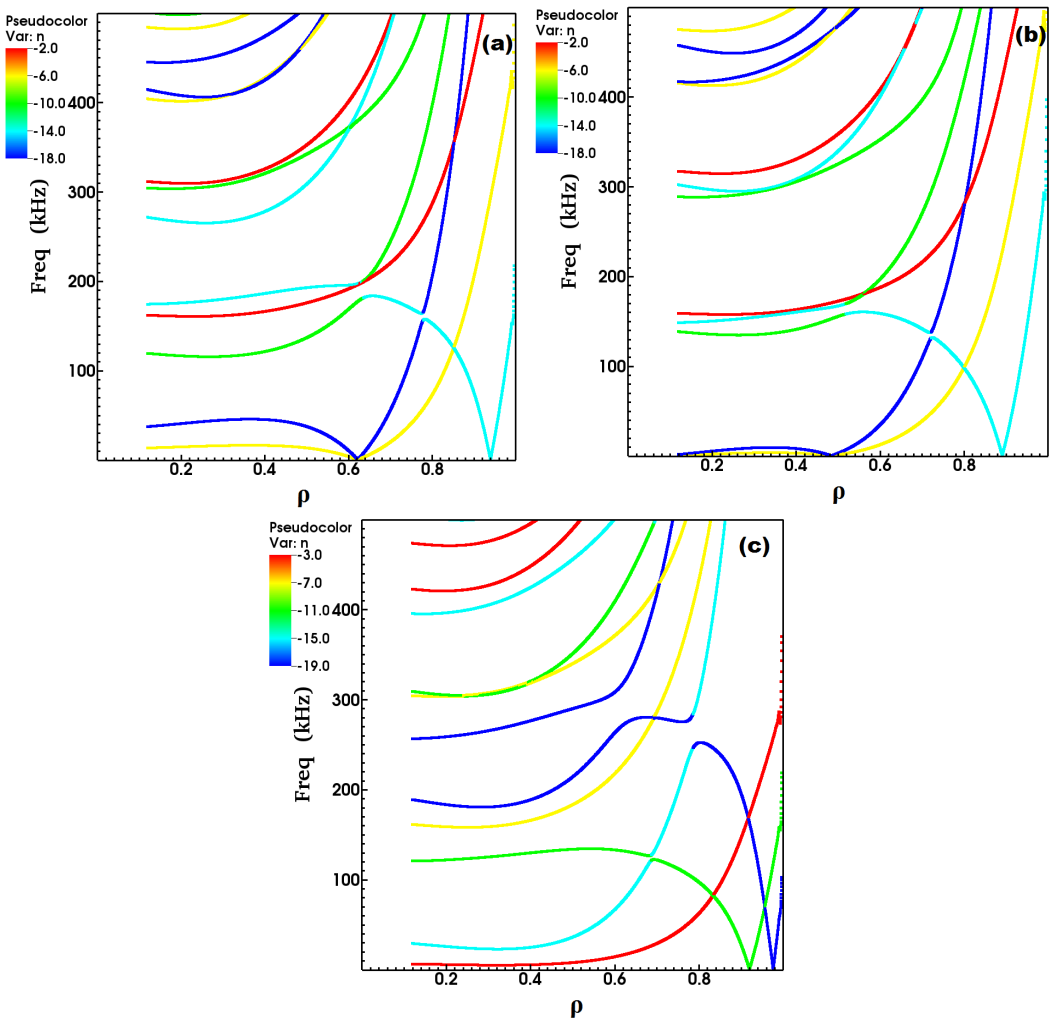

Fig. 5.7 Alfvén continuum structures for the extended low shear NM iota profiles with on-axis values of $\iota(0)$ = (a) 1.49, (b) 1.50 and (c) 1.51, while keeping all other parameters of discharge 27804. The color coding of continua represents the corresponding toroidal mode number (n).

In the second step, for modeling the observed frequency sweeping modes, a radially extended low-shear NM iota profile (Figure 5.4) is used; similar iota profiles have been

considered in previous investigations [67]. The corresponding continua for three similar radially extended low-shear NM iota profiles with different on-axis iota $\iota(0)$ are plotted in Figure 5.7. The continuum structures that form extrema and gaps in all three continua are extended radially up to $\rho \approx 0.75$ as the corresponding iota profiles are extended. In addition, gaps and extremum points move radially outward and upward in frequency as the $\iota(0)$ value increases from 1.49 to 1.51. Particularly, in the case of $\iota(0) = 1.50$ there are two wide gaps, the first between 5 kHz to 140 kHz and the second between 170 kHz to 290 kHz; these are important since they provide possibility of modes which may have larger frequency variations. Since the normal and one of the low-shear NM iota profiles have $\iota(0) = 1.50$, it seems reasonable to explain observed frequency sweeping modes using wider continuum gaps with the low shear NM iota profile.

In the third step, Alfvén continua are calculated while varying the minimum value ι_{min} for the strong negative shear NM iota profiles (see Figure 5.5). Variation of ι_{min} provides an opportunity to model an optimum iota profile scaling with the mode frequency; this diagnostics methodology is referred as MHD spectroscopy [18].The continuum structures for three out of seven iota profiles ($\iota 1$, $\iota 4$, and $\iota 7$) from left to right cover significant differences between these continua and show all gap structures in Figure 5.8. Three important gaps with frequencies in the range of 70-80, 140 and 210 kHz persist in all three continuum structures besides the extremum points. In addition to the persistence of the gaps, they are core localized and radially extended up to $\rho \approx = 0.6$. Towards the edge of plasma column the continuum structures do not form any gaps. In these modeled continua a large number of the gaps appear which provide the possibility of describing the large frequency range for the observed frequency sweeping modes.

The comparison of the Alfvén continuum structures shows relatively fewer gaps and extremum points for the normal iota profile, covering a short frequency range and radial extent. While there are relatively wider spectrum of gaps and extremum points across a wider frequency range and radial extent for both NM iota profiles.

This comparative study also highlights the effect of NM iota profile with the generation of extremum points in the range of the low-frequency Alfvén continuum. Comparison between the Alfvén continua of normal and NM iota profiles shows that the gaps are radially very localized in normal iota profiles whereas for the NM iota profiles the gaps or extemum points are radially extended in the core region of plasma column. These radially localized and /or extended gaps accommodate a large number of modes which support the observed frequency sweeping modes.

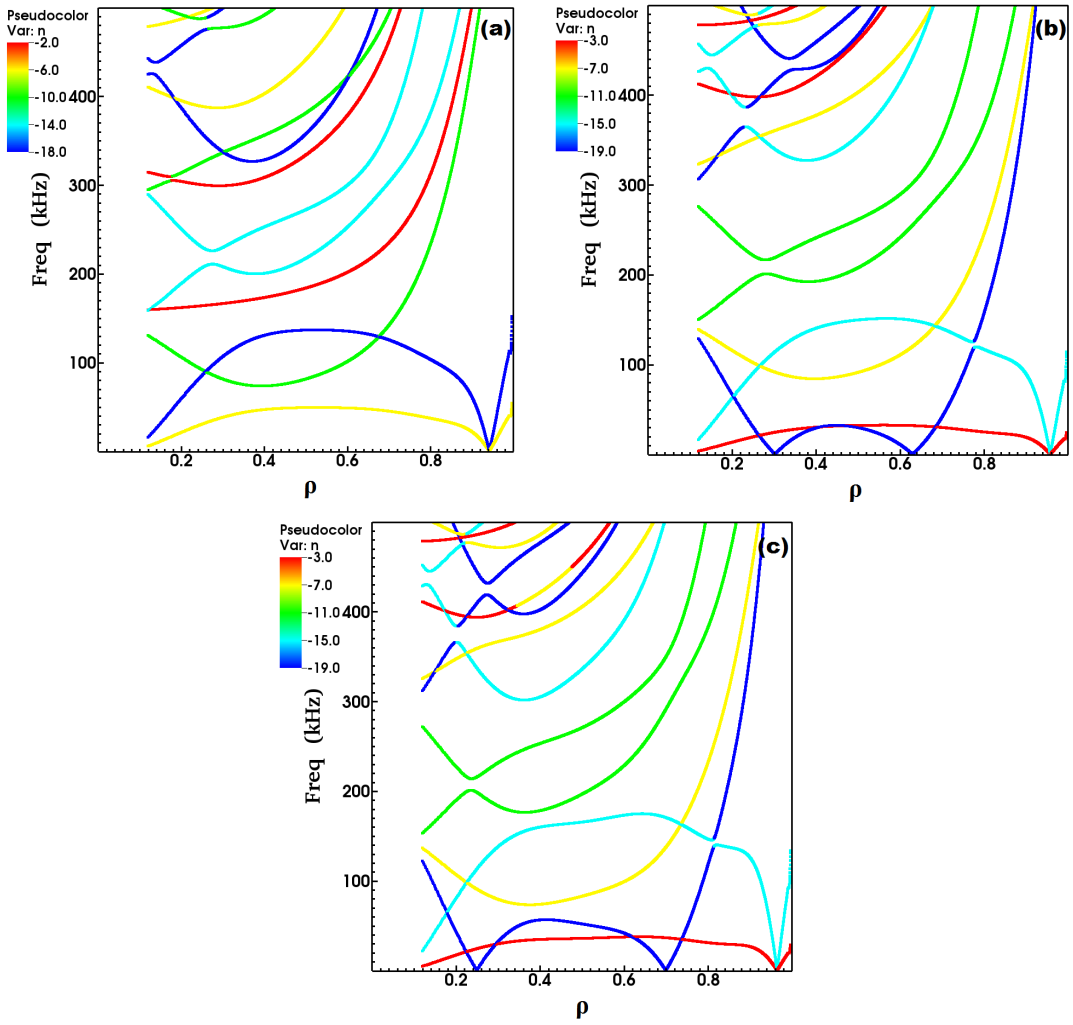

Fig. 5.8 Alfvén continuum structures for the strong shear NM iota profiles with on-axis value $\iota(0) = 1.50$ for the (a) ι_1, (b) ι_4, and (c) ι_7 profiles from left to right by keeping all other parameters of discharge 27804. The color coding of continua represents the corresponding toroidal mode number (n).

5.5.2 Alfvén modes analysis

In section 5.5.1, our modelling results of Alfvén continua for the TJ-II discharge 27804 with normal, low and strong shear NM iota profiles are provided. In this section we provide mode analysis using reduced MHD clustered frequency solver AE3D for the cases modeled. The mode analysis provides the potential profiles, radial localization, mode frequencies and the combination of prominent toroidal 'n' and poloidal 'm' mode numbers.

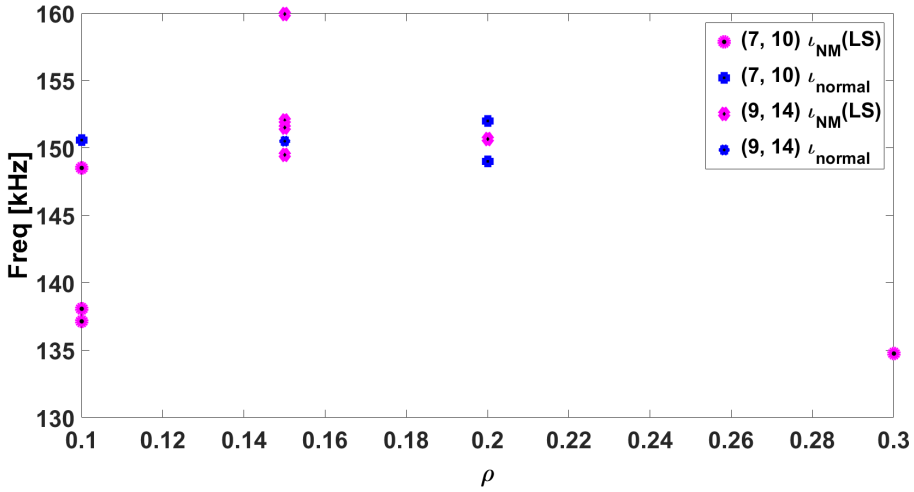

Fig. 5.9 Scatter plot for frequencies and radial locations of the identical modes obtained with the normal and low shear NM iota profiles with on-axis iota $\iota(0) = 1.50$

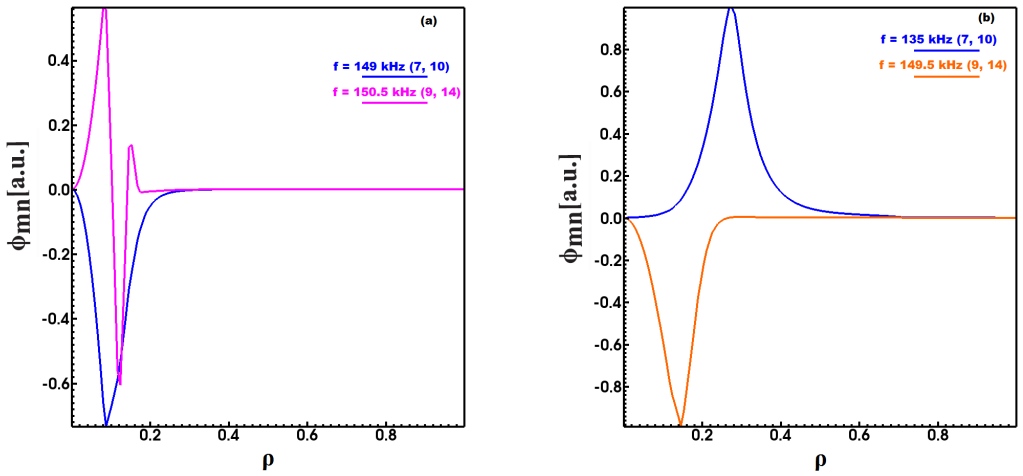

Fig. 5.10 Alfvén modes with the (a) normal and (b) low shear NM iota profiles with on-axis iota $\iota(0) = 1.50$. The corresponding frequencies and prominent mode number pairs (m, n) are shown as legend.

Simulations show that both in normal and NM low shear iota profiles with on-axis iota $\iota(0) = 1.50$ some identical modes are present. Their frequencies and radial positions are shown in Figure 5.9. The modes are core localized for these iota profiles. However, the number of modes increases and they cover a larger frequency range for the low shear NM iota profile. The potential profiles of the modes (m = 7, n = 10) and (m = 9, n = 14) which appear in the both iota profiles are plotted in Figure 5.10. It shows

the modes for the low shear NM iota profile are relatively extended radially up to $\rho \approx 0.3$ with frequencies 135 and 149 kHz while for normal iota profile similar modes are present which are radially localized around $\rho \approx 0.1$ and they have a frequency of 150 kHz.

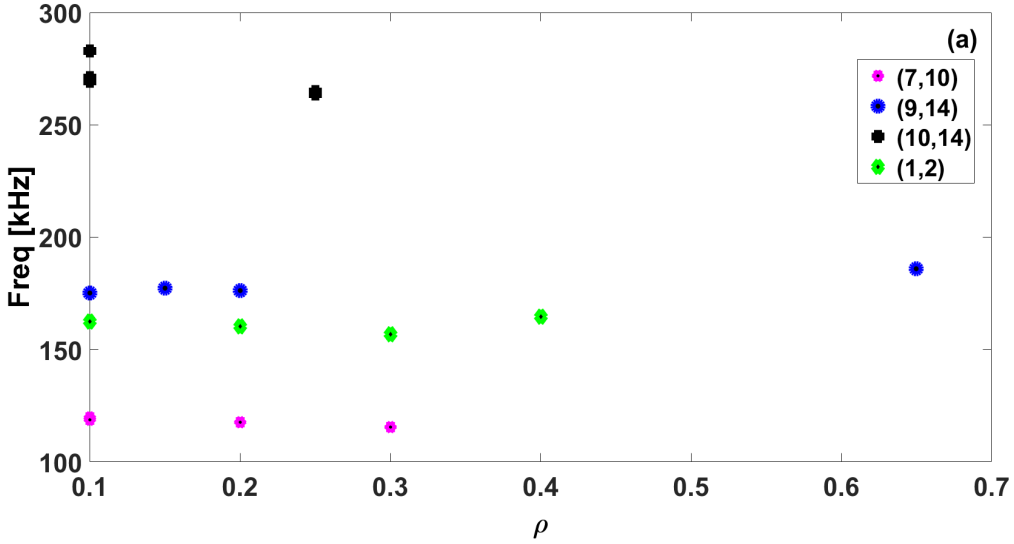

Fig. 5.11 Scatter plots for frequencies and radial locations of the prominent modes obtained with the low shear NM iota profiles with $\iota(0) = 1.49$

The modal analysis for the three similar low shear NM iota profiles having different $\iota(0)$ is shown in Figures 5.11,5.12, and 5.13. A large number of modes are present in these low shear NM iota profile cases covering a wide range of radial extents up to $\rho \approx 0.8$ with frequencies up to 300 kHz. The number of modes decreases as $\iota(0)$ increases from 1.49 to 1.51. The radial potential profiles of the representative modes are presented in Figure 5.14. An identical mode (m = 7, n = 10/11) appears for these three similar iota profiles, where as for $\iota(0) = 1.51$ the n = 11 becomes prominent instead of n = 10 because of the selection of the n+1 continuum. Qualitatively these modes share identical frequencies, while their radial extents are unique. Most of these modes are dominated by a single poloidal mode forming structures similar to the GAEs. The modes with lower n i.e. n = 2 are extended over a wider radial extent and the modes with higher n are relatively localized over their radial positions. Modes having properties of a single poloidal dominance and their radial localization for the higher n suggest that these modes are reversed shear AEs. One of the modes (m = 7, n = 10/11) which appears in all of three parts has frequencies of 115, 135 and 121 and 135 kHz with radial locations of $\rho = 0.25$, 0.3 and 0.15 and 0.55 respectively.

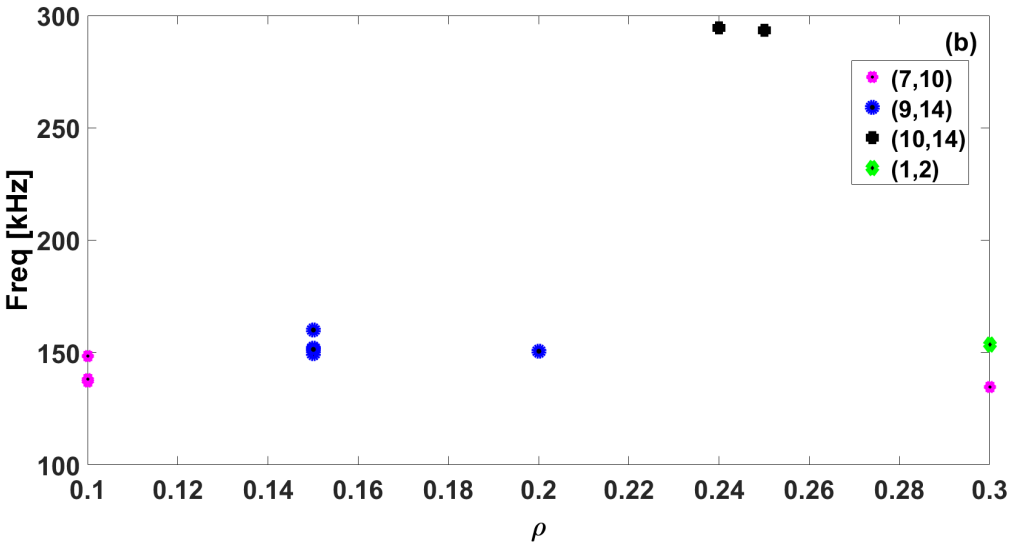

Fig. 5.12 Scatter plots for frequencies and radial locations of the prominent modes obtained with the low shear NM iota profiles with $\iota(0) = 1.50$

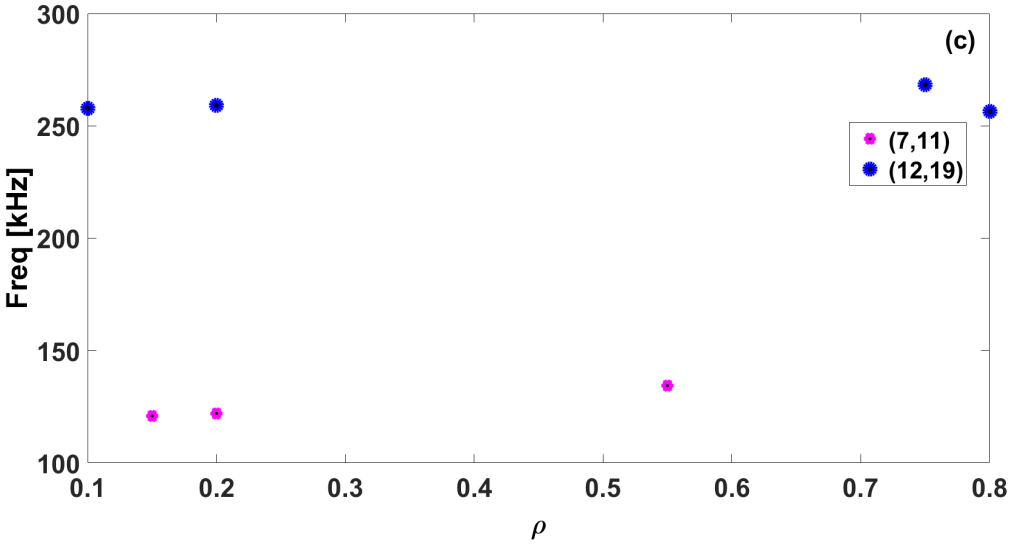

Fig. 5.13 Scatter plots for frequencies and radial locations of the prominent modes obtained with the low shear NM iota profiles with $\iota(0) = 1.51$

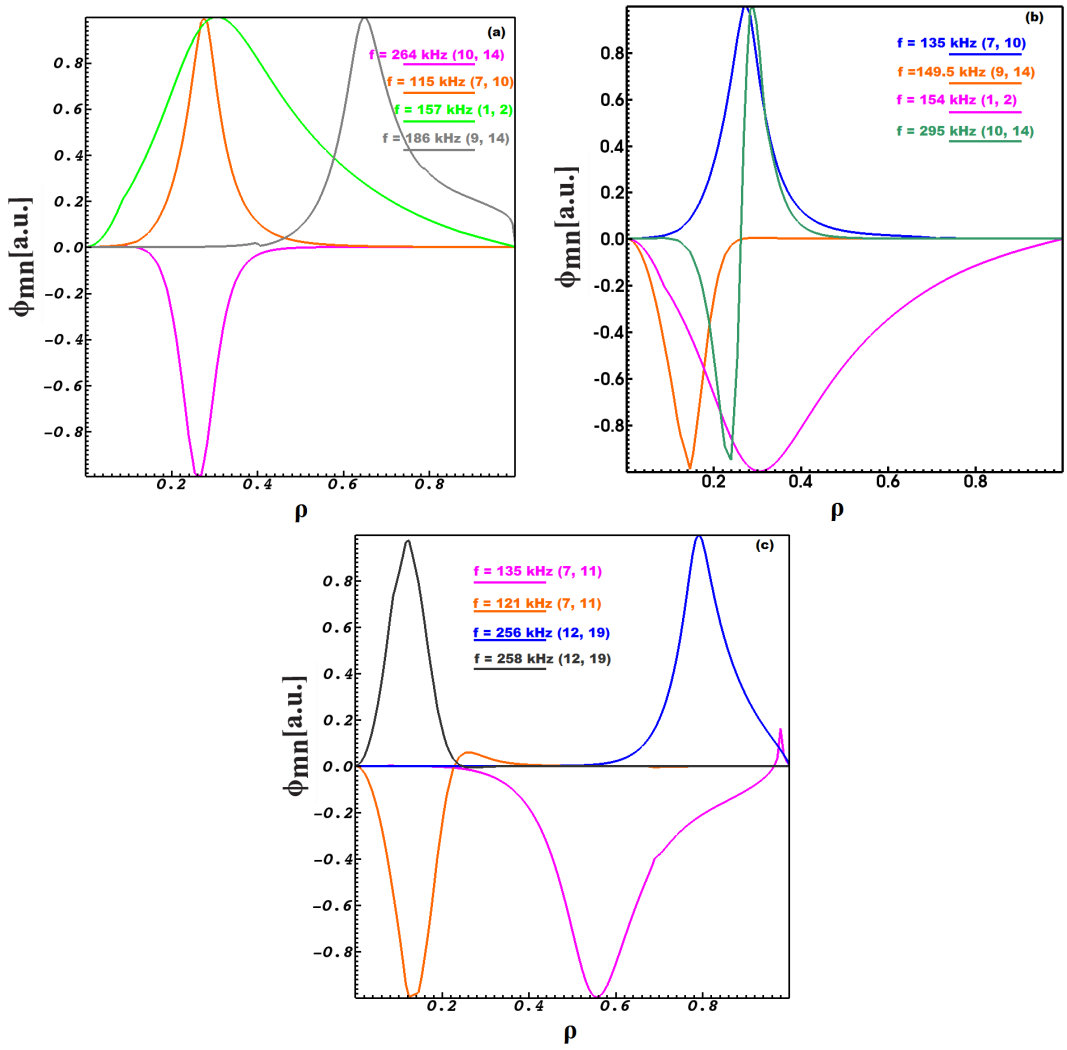

Fig. 5.14 Alfvén modes with the low shear NM iota profiles with $\iota(0)$ = (a) 1.49, (b) 1.50 and (c) 1.51. The corresponding frequencies and prominent mode number pairs (m, n) are shown as legend.

After investigating the Alfvénic instabilities for the monotonic and low-shear NM iota profiles, further investigations with the relatively strong shear NM iota profiles are performed. Seven similar iota profiles shown in Figure **??** with varying ι_{min} having identical shapes and $\iota(0) = 1.50$ are employed to investigate the effect of ι_{min} on the modes. Figures 5.15 and 5.16 show that the frequency of prominent modes does not vary much with variation in ι_{min}, although the finite variations are computed which are an essence of the ι_{min} variations. Results are divided into two similar sets on the basis of modes which appear in each set, since after the ι_4 profile the mode numbers get modified because of the selection of higher n+1 continua for those cases. Results show a decrease in the number of the prominent modes as ι_{min} is decreased.

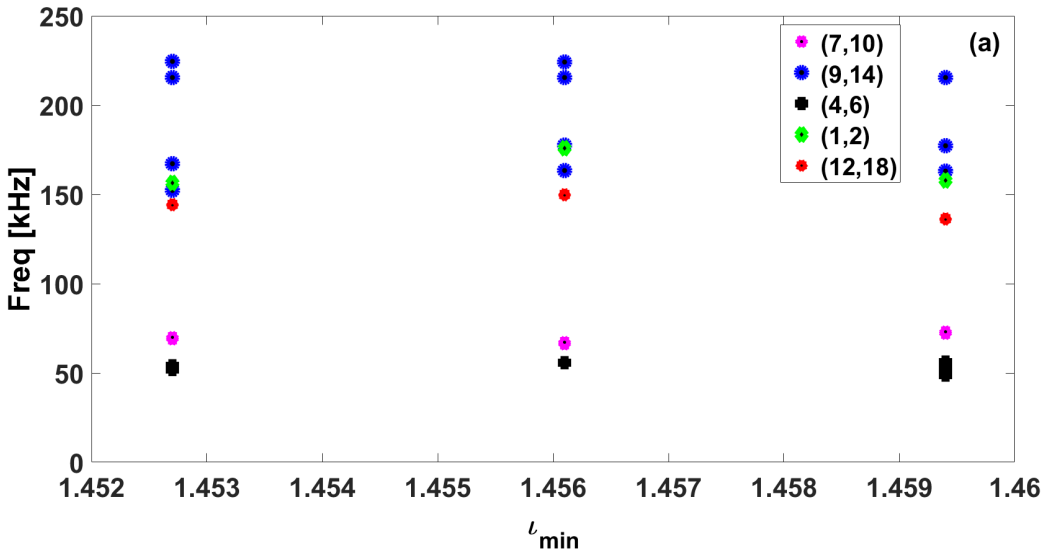

Fig. 5.15 The variation of the frequencies with minimum value of iota ι_{min} of the identical modes obtained with the strong shear NM iota profiles having $\iota(0) = 1.50$ for the iota profiles ι_1 to ι_3 of Figure 5.5.

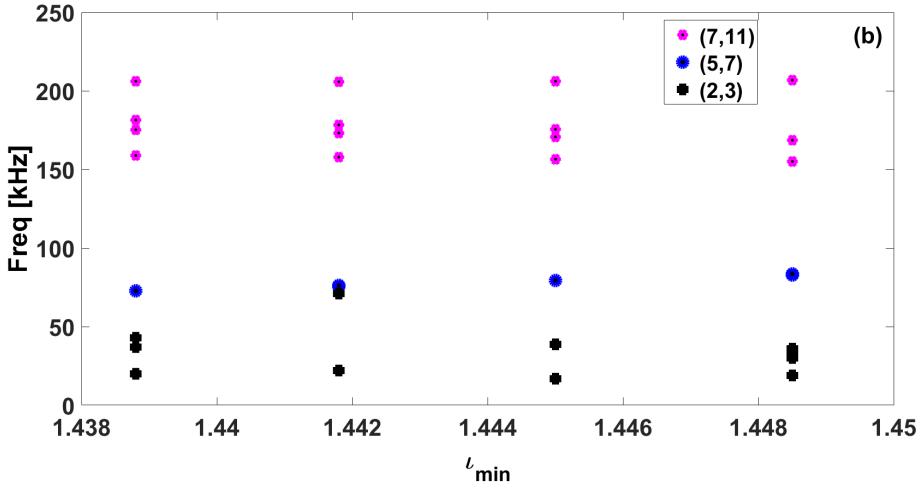

Fig. 5.16 The variation of the frequencies with minimum value of iota ι_{min} of the identical modes obtained with the strong shear NM iota profiles having $\iota(0) = 1.50$ for the iota profiles ι_4 to ι_7 of Figure 5.5.

The radial potential mode structures of the prominent modes for the relatively strong shear NM iota profiles from ι_1 to ι_3 are plotted in Figure 5.17. Similarly with the low shear NM iota profile case, the modes with relatively strong shear NM iota profiles are dominated by a single poloidal harmonic and radially localized except modes (m = 1, n = 2) and (m = 4, n = 6) which are radially extended over a wide

region and characterized as GAEs. The mode (m = 4, n = 6) also seems to go through a transition from GAE to RSAE after becoming radially localized for the ι_3 case. Small fluctuations in the frequencies of the modes (m = 4, n = 6) and (m = 7, n = 10) are found among the ι_1 and ι_3 cases. Most of these modes are radially localized up to ρ = 0.6 except the GAEs. These modes cover a range of frequency from 49 to 216 kHz, which is roughly consistent with the experimental findings.

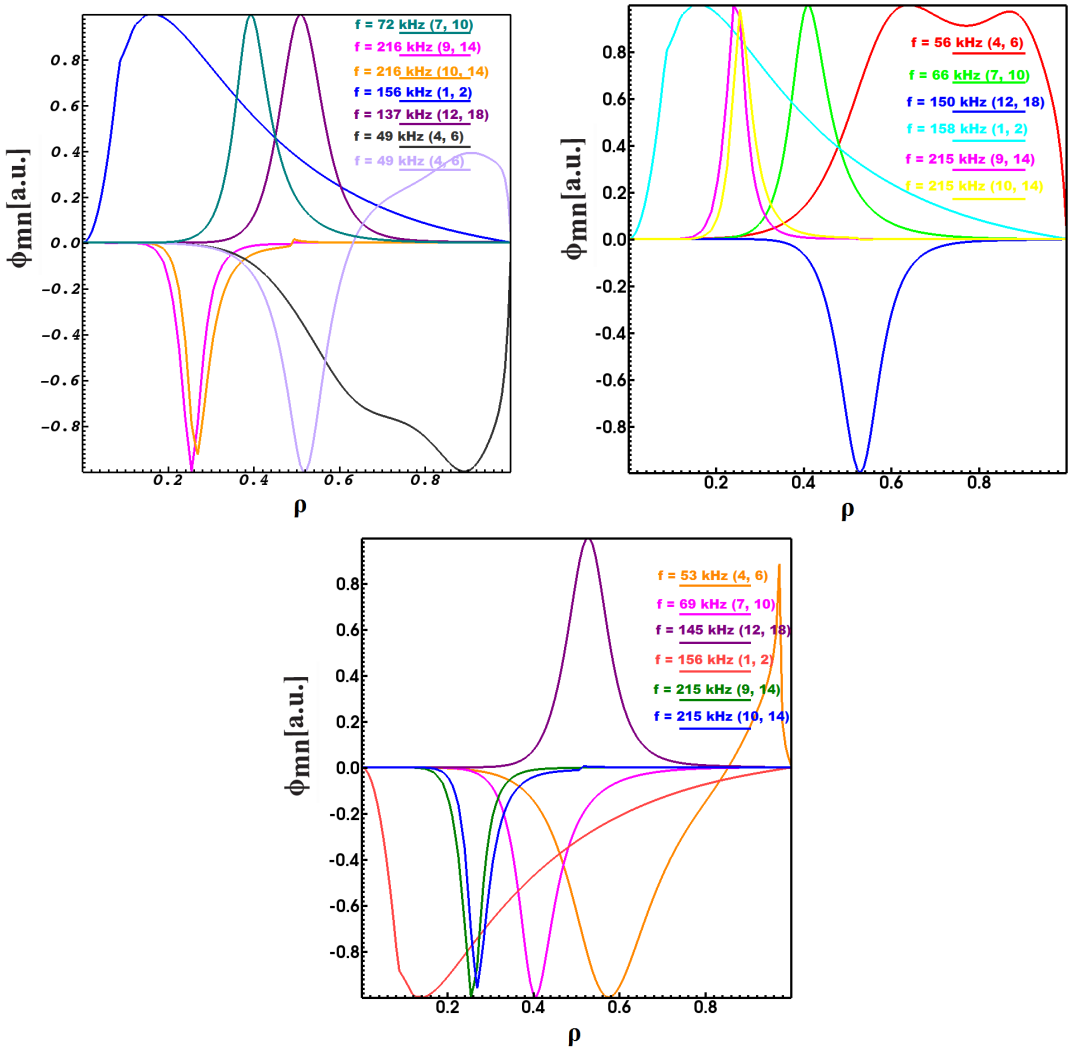

Fig. 5.17 Alfvén eigenmodes (AEs) radial structures for the NM iota profiles (a) ι_1 with ι_{min} = 1.4594 (b) ι_2 with ι_{min} = 1.4561 and (c) ι_3 with ι_{min} = 1.4527. The corresponding frequencies and prominent mode number pairs (m, n) are shown as legend.

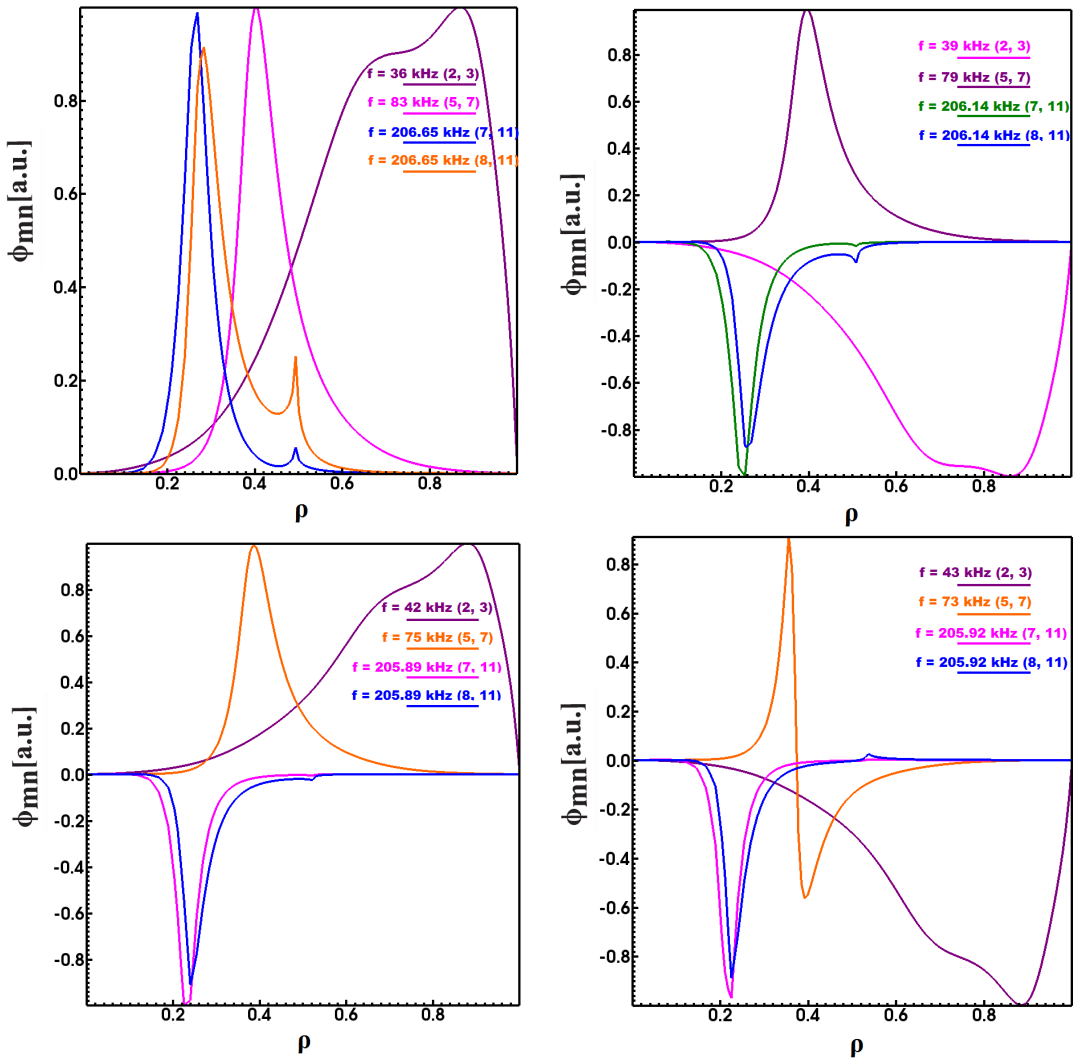

Fig. 5.18 Alfvén eigenmodes (AEs) radial structures for the NM iota profiles (a) ι_4 with $\iota_{min} = 1.4485$ (b) ι_5 with $\iota_{min} = 1.4450$ (c) ι_6 with $\iota_{min} = 1.4418$ and (d) ι_7 with $\iota_{min} = 1.4388$. The corresponding frequencies and prominent mode number pairs (m, n) are shown as legend.

The radial potential mode structures for the second set of strong shear NM iota profiles results from ι_4 to ι_7 are plotted in Figure 5.18. There are four prominent modes covering a wide range of frequencies from 36 to 206.65 kHz. Three of these modes which are radially localized around $\rho = 0.4$ and their frequency decreases with decreasing ι_{min}. These are characterized as RSAEs and one of them (m = 2, n = 3), which is radially extended over a wider extent up to $\rho = 0.9$ increases in frequency from 36 to 43 kHz as ι_{min} decreases. This mode is characterised as GAE.

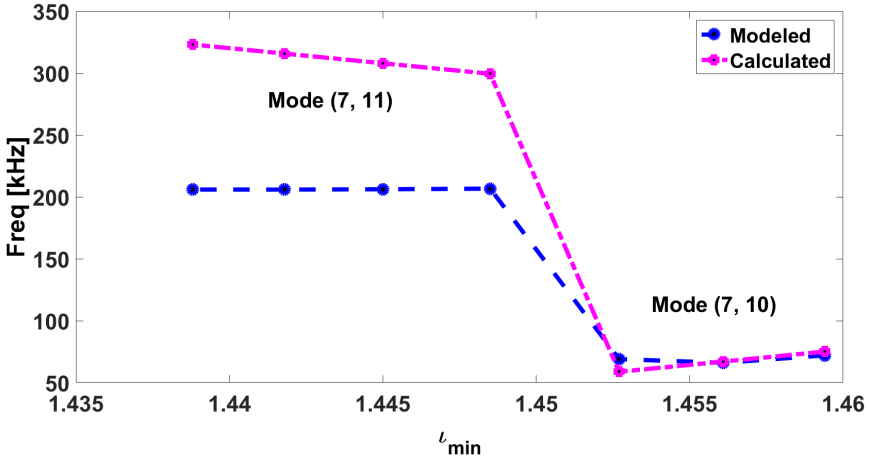

Fig. 5.19 Variation of the modeled frequency (using AE3D code) of the mode with ι_{min} and its comparison with the calculated mode frequency (using analytical dispersion relation).

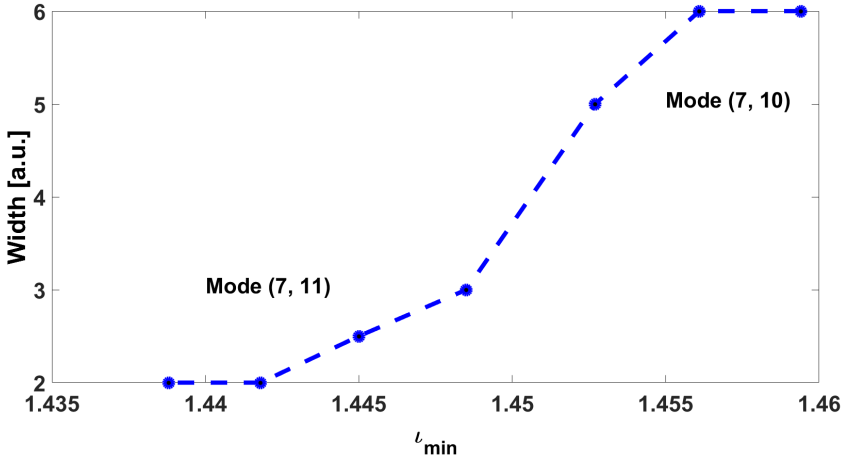

Fig. 5.20 Variation of the mode width calculated as FWHM of mode amplitude with ι_{min}

The frequency change of the modes (m = 7, n = 10/11) with the variation of the ι_{min} is plotted in Figure 5.19. It shows for both of the modes (m = 7, n = 10/11), the frequencies calculated with the dispersion relation of the shear Alfvén waves given as $\omega = |m - (\iota_{min}/2\pi)n|V_A/R$ by using ι_{min} values and modeled through the reduced MHD model by using strong shear NM iota profiles are consistent. There are differences at low ι_{min} values between the frequencies of modeled and calculated modes, since in these calculations we have focused on the lower frequencies of the modes and have discarded the calculation of the higher frequency modes. Therefore, these differences

can be accepted for this comparison. This comparison may provide a possible diagnostic tool for the calculation of ι_{min} in fusion plasmas.

The radial width of the identical modes (m = 7, n = 10/11) is also calculated and its variation with ι_{min} is plotted in Figure 5.20. This shows that the radial width of these modes increases with the increasing ι_{min} values. Figures 5.17 and 5.18 show that the amplitude of the computed modes qualitatively remains almost constant around 0.1 of the arbitrary units. This indicates that the strong shear drives the modes narrower and more radially localized. The narrower modes do not drive energetic particles radially due to a low region of interaction with fast ions. Therefore, strong shear NM iota profiles with lower ι_{min} are considered favourable for the AE stability.

5.6 Summary and conclusions

A detailed analysis of the Alfvénic instabilities has been performed using the STELLGAP and AE3D codes for three different types of rotational transform profiles in the low-field and low density TJ-II stellarator plasmas where frequency sweeping Alfvénic activity was observed [6]. In the comparison of the results of normal and radially extended low shear NM iota profiles, two similar core localized modes (m = 7, n = 10) and (m = 9, n = 14) appear with discrete frequencies. The frequency range of the modes calculated using the low shear NM iota profile goes from 135 to 150 kHz and is relatively larger than that for the normal iota profile where these modes are centred around 150 kHz. This shows the results obtained using the low shear NM iota profile explain better the frequency sweeping observed experimentally. Additionally, finite variations in the on-axis iota value lead to shifted low-shear NM iota profiles. Simulations with these iota profiles have found a variety of Alfvén modes covering a similarly wide frequency range from 115 to 295 kHz. Radially extended GAE and localized RSAEs are identified in these calculations covering a radial range up to ρ = 0.6. Radially localized RSAEs (m = 7, n = 10/11) appear with the frequencies of 115, 135 and 121 kHz and radial localization around ρ = 0.3 and 0.15 for $\iota(0)$ = 1.49, 1.50 and 1.51 respectively.

The investigations with relative strong shear NM iota profiles with varied ι_{min} have confirmed the appearance of the same mode for each iota profile. In simulations, the mode (m = 7, n = 10/11) appears for all of the seven strong shear NM iota profiles radially localized around ρ = 0.45, which is the location of ι_{min}. The frequencies obtained from AE3D simulations are consistent with the those calculated through an analytical dispersion relation using ι_{min}. This mode's consistency with similar

NM iota profiles offers an opportunity to model ι_{min}. These calculations support the development of MHD spectroscopy as a sensitive iota profile diagnostic technique for future fusion devices where other methods may not be practical.

The modes obtained in these calculations have global structures and therefore can be considered to impact the fast ion confinement and hence their heating efficiency. In the modal analysis some cases show modulational effects from multiple competing Alfvén modes with discrete frequencies. Modes with lower frequency and radially extended global structures are characterized as GAEs while radially localized modes with relatively higher frequency are identified as RSAEs. The width of the mode (m = 7, n = 10/11) increases with increasing ι_{min} values; therefore, with strong magnetic shear the mode becomes narrower and its frequency in each choice of ι_{min} nearly remains constant.Since a narrower mode has a lower region for interaction with energetic particles, it could possibly to reduce the radial transport of the energetic particles. It shows that an iota profile with strong shear and lower ι_{min} becomes more favourable for the stability of Alfvénic instabilities in the TJ-II plasmas.

In the future there is possibility of investigating these instabilities with the interaction of energetic particles by calculating their growth rates, amplitudes and three dimensional mode structures.

Chapter 6

Wave-particle resonances in stellarator plasmas

6.1 Overview

In this chapter, a resonance condition for the TJ-II stellarator has been evaluated using 3D MHD equilibrium as an initial input besides the transformation into Boozer coordinates and setting initial inputs as discussed in the coming part. In these calculations the corresponding wave-particle resonance maps suggest for low bounce harmonics (p) the possibility of describing the nonlinear evolution of the AEs in TJ-II by a sum of two ion populations with different weighting factors, one of which is dominated by drag and the other by diffusion. As the bounce harmonic increases, the resonance region starts to expand and can cover over a significant area of the particle phase space until this resonance region vanishes at high bounce harmonics.

This chapter is organized as follows: Briefly the Monte Carlo transport model employed in the DELTA5D code is discussed in section 6.2. In section 6.3 the results for wave-particle resonances in TJ-II are presented. Section 6.3 also includes a discussion on two fast particle populations with different weighting factors as a possible explanation for the observed non-linear evolution of the modes. Finally, section 6.4 includes the concluding remarks.

This work has been published in:

[47] **A. Rakha** et al., Modelling of beam-driven Alfvén modes in TJ-II plasmas, *Nuclear Fusion* **59** 056002, 2019.

6.2 Monte Carlo transport model

Energetic particle confinement in toroidal fusion devices with 3D perturbations is important for plasma heating, current drive, ignition margin evaluation, steady-state operation and device wall safety as wall heat loads in future ignited systems would be considerable. Energetic particle confinement can especially be degraded by instabilities such as fishbones and Alfvén modes that involve resonant wave-particle interactions. Fast ions may channel out of the burning plasma through prompt losses or get scattered into various loss regions. Resonance condition for these fast ions has been evaluated by finding their toroidal ω_ϕ and poloidal ω_θ precession frequencies corresponding to one of the resonating Alfvén eigenmode frequency and prominent mode numbers. For the wave-particle resonant interaction studies we have used DELTA5D Monte Carlo code [70, 71], which computes orbits and losses of fast ions using 3D MHD equilibria as an input. This follows orbits in Boozer space using Hamiltonian guiding center equations that are solved using an adaptive time step integrator. It is a guiding center orbit trajectory code that can also include fluctuating TAE mode structures with chirping frequencies. It performs ion transport calculations for both steady and chirping modes. Pitch angle and energy scattering are included using a Langevin approximation [72] to the collision operator and retaining the full velocity dependence of the collision terms. In this model, particles can be followed outside of the last flux surface until a wall intersection occurs. The derivation of these equations is considered beyond this thesis work, which have been performed in [70].

This model launches an ensemble of energetic particles with an initial energy around a specific toroidal location on a single interior flux surface randomly distributed in pitch angle and in toroidal and poloidal angles. In calculations the particle energies are approximated with with Maxwellian distribution. The different classes of orbits even with large displacements of fast ions are then traced using Hamiltonian guiding center equations. The $\mathbf{B}$ field is calculated over a large spectrum of the equilibrium $\mathbf{B}_{m,n}$ Fourier modes. As the particles are traced up to the outermost flux surface beyond that they start to leave the system, which are then reinitialized at the starting flux surface to keep the particle density conserved.

6.3 Modelling of wave-particle interaction in TJ-II

To assess the phase space region of the neutral beam injected fast ions which provides the main contribution to the wave-particle interaction, a resonance map of contours of,

$$\Omega \equiv \omega - n\,\omega_\phi - p\,\omega_\theta = 0 \tag{6.1}$$

was computed with the particle-following code DELTA5D for the beam injection geometry and magnetic equilibrium specific for the chosen time slices of interest. Here, ω_ϕ and ω_θ are the toroidal orbit frequency and the poloidal precession frequencies of the beam ions, respectively, n and ω are toroidal mode number and frequency of the AE, respectively, and the integer p is the bounce harmonic.

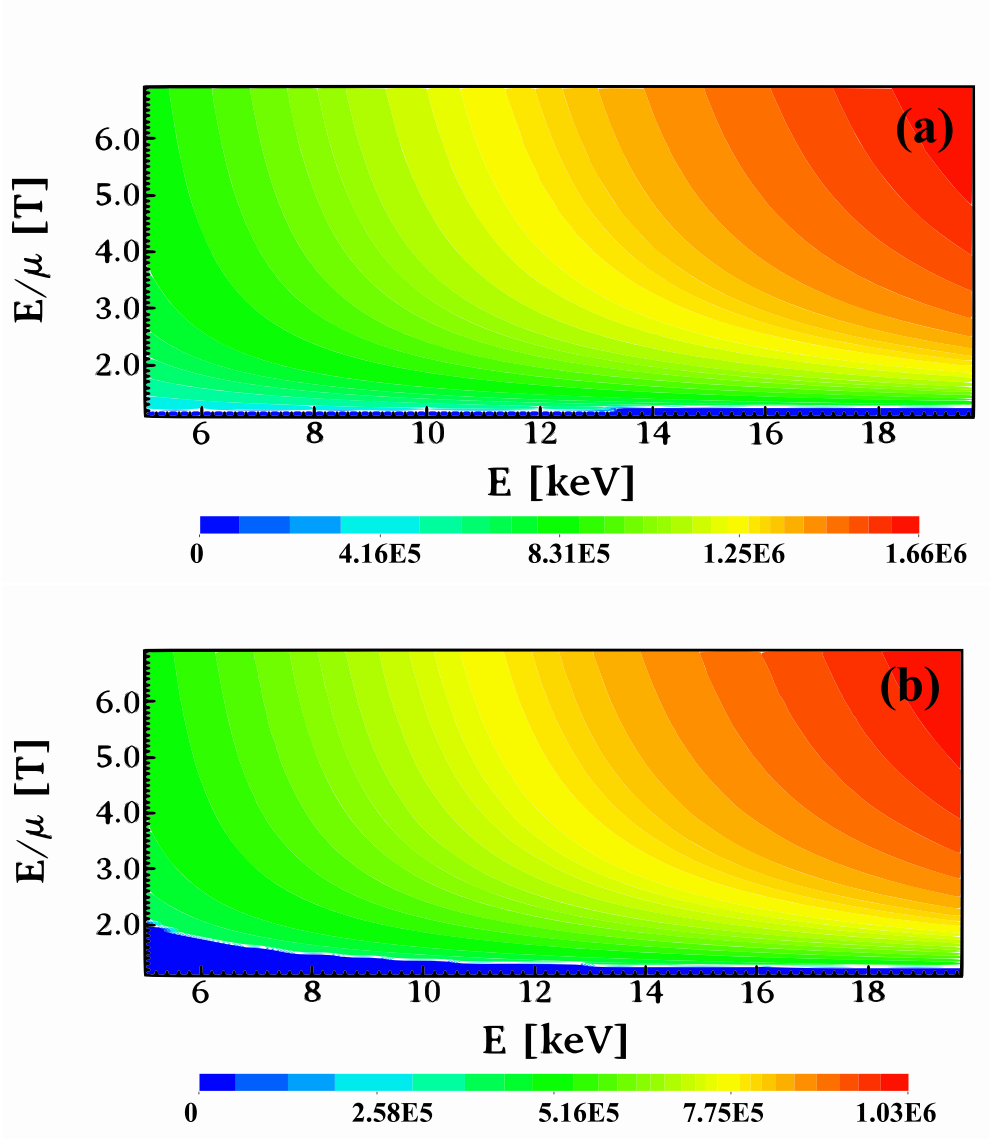

Fig. 6.1 Contour plots of (a) poloidal orbit frequency ω_θ and (b) the toroidal precession frequency ω_ϕ for the beam ions launched at $\rho = 0.25$.

In stellarators, due to the lack of axisymmetry, the toroidal mode number n is no longer a good quantum number since any specific toroidal mode can be coupled through the equilibrium variation of the magnetic field to other toroidal mode numbers displaced by N_{fp}, the field period number of the stellarator. Therefore, it is necessary to characterize stellarator mode structures in terms of toroidal mode families [73, 74] consisting of $n \pm N_{fp}, n \pm 2N_{fp} \cdots$. For any observed Alfvén instability, one of these n's will be dominant and this primary value of n is the one considered here for resonance evaluations. For assessing the resonances for the AEs found at different radii, beam particles were launched from the positions of $\rho = 0.25$, 0.55 and 0.75.

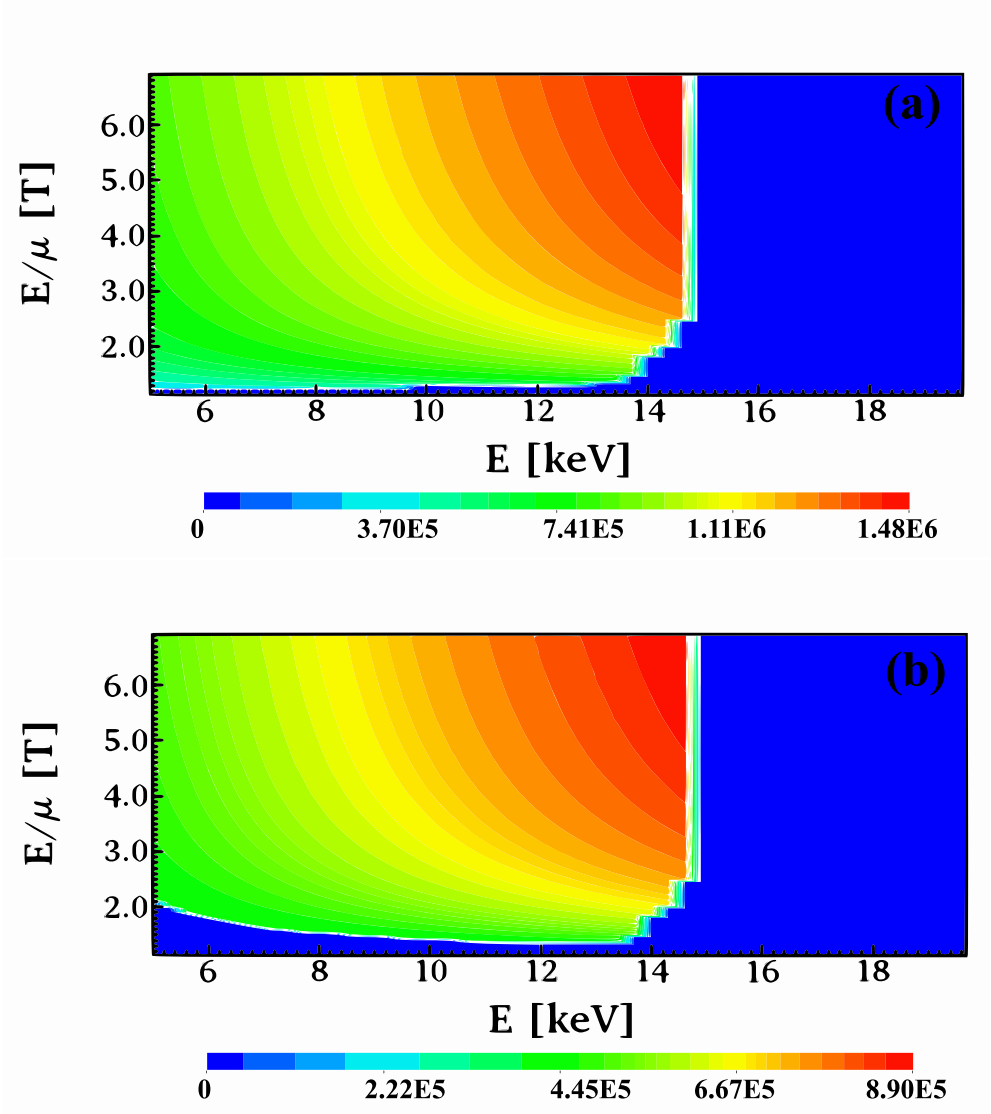

Fig. 6.2 Contour plots of (a) poloidal orbit frequency ω_θ and (b) the toroidal precession frequency ω_ϕ for the beam ions launched at $\rho = 0.55$.

For each value of ρ, fast hydrogen ions were launched in the range of energies 5 keV < E < 20 KeV and pitch-angles 1 T< E/μ < 9 T. For every fast ion launched, the corresponding drift orbit were computed assuming unperturbed particle motion, and the characteristic frequencies ω_ϕ and ω_θ were found as 2D functions of fast-ion energy and pitch-angle. The obtained 2D matrices for poloidal and toroidal frequencies of the drift orbits are shown in figures 6.1- 6.3.

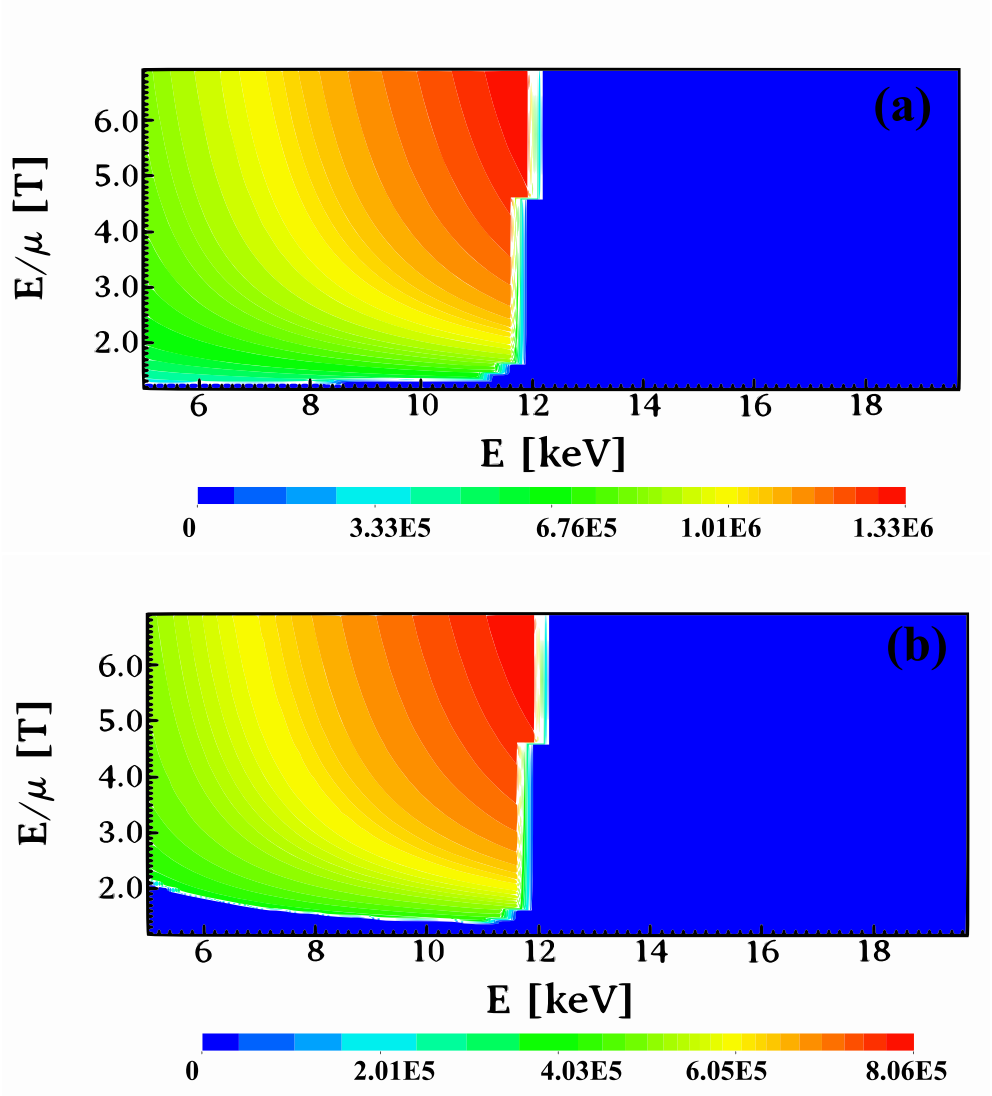

Fig. 6.3 Contour plots of (a) poloidal orbit frequency ω_θ and (b) the toroidal precession frequency ω_ϕ for the beam ions launched at $\rho = 0.75$.

As ρ increases from 0.25 (Figure 6.1) to 0.55 (Figure 6.2), and then to 0.75 (Figure 6.3), the area of unconfined beam ions as indicated by the blue area expands, effectively pushing the phase space area of confined beam ions down to lower energies.

Using the calculated poloidal orbit frequency and the toroidal precession frequency, one can now combine their 2D functions in the form (6.1) for various integer values of p and for the frequency and toroidal mode number of the AE of interest.

The resulting 2D function is then the resonance map, showing the phase space regions involved in the wave-particle resonance as a function of energy and pitch-angle. Figure 6.4 shows resonance maps relevant to the core-localised AE with a frequency of 306.57 kHz, for a range of p values and n = 11 for beam ions launched at $\rho = 0.25$. This high frequency core localized AE was considered a suitable candidate for resonance calculations because of its characteristics similar to the Global Alfvén eigenmode (GAE) having fewer poloidal couplings. The resonance maps for a relatively edge-localised AE having frequency 316 kHz and toroidal mode numbers 13 and 17 are computed to investigate the effect of higher frequency, toroidal mode number n and bounce harmonic p on the resonance condition. In figure 6.5 the resonance maps for an AE with a frequency of 316 kHz, for a range of p values and n = 13 for beam ions launched at $\rho = 0.25$ are presented and figure 6.6 presents for similar results for n = 17.

The special shape of the resonance map in figures(6.4a, 6.5a, 6.6a) suggests a natural division of the resonant ions in two phase space regions. Region 1 (orange oval) is narrow in energy (3 keV $<$ E $<$ 4 keV), but insensitive to pitch angle, while region 2 (black oval) covers only a narrow range of pitch angles and extends in energy (5 keV $<$ E $<$ 12 keV).

In region 1, the beam ions are affected by the electric field of the AEs and are replenished due to the beam energy scattering and electron drag. In contrast to this, the region 2 replenishes by pitch-angle scattering (with a diffusive collisional operator). Therefore, in the case of the TJ-II resonance map, one arrives at the possibility of describing the nonlinear evolution of the AEs by a sum of two ion populations with different weighting factors, one of which is dominated by drag and the other by diffusion for lower values of the bounce harmonic p. For higher values of p, the resonance zone expands towards higher energy range covering a significant part of pitch angle region and for further higher values of p, the resonance vanishes completely as shown in figures (6.4, 6.5, 6.6). It can also be noticed, for higher frequency and toroidal mode number n there is wider spectrum of p values which is available for two regions dominated resonance before reaching the zero resonance region.

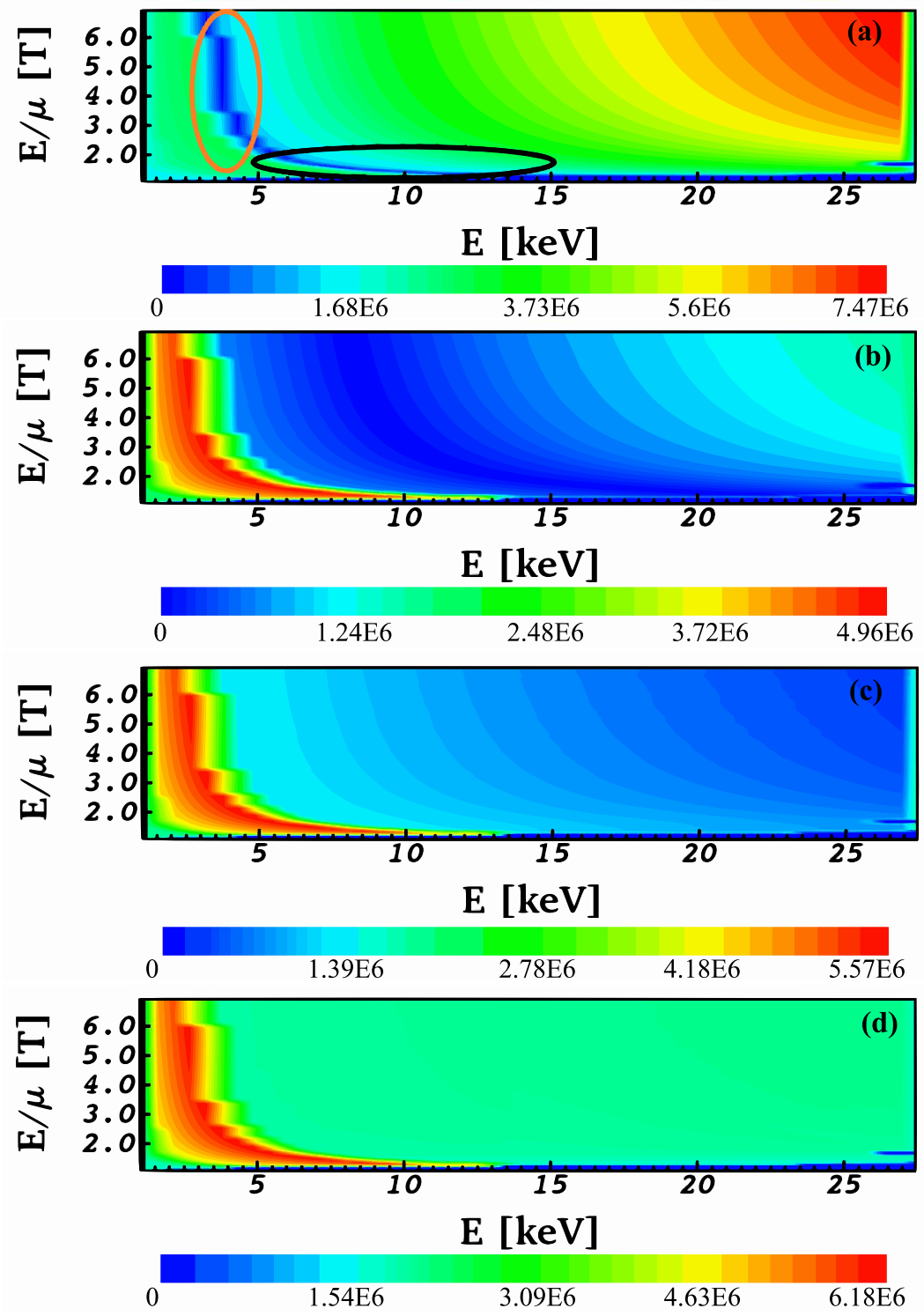

Fig. 6.4 Resonance maps $\Omega \equiv \omega - n\,\omega_\phi - p\,\omega_\theta = 0$ for the core-localised AE with a frequency of 306.57 kHz and n = 11 for beam ions launched at $\rho = 0.25$. Resonance map for (a) $p = 0$ to 2, here the orange oval marks Region 1 which is narrow in energy, but insensitive to pitch angle. The black oval marks Region 2 which covers a narrow range of pitch angles and extends in energy, (b) the extended resonance region with $p = 5$, (c) movement of resonance region towards higher energy for $p = 6$ and (d) no resonance at $p = 7$.

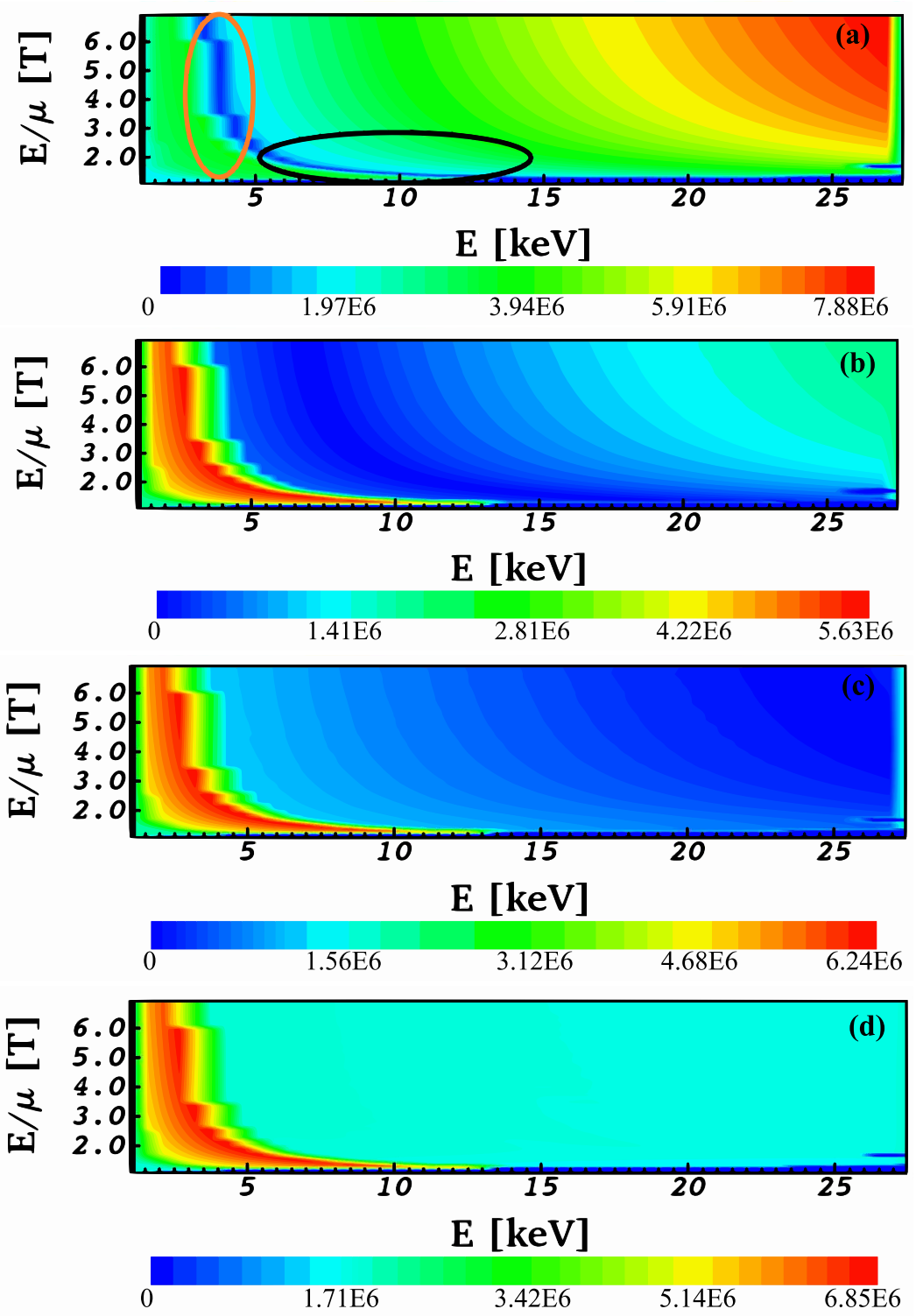

Fig. 6.5 Resonance maps for the edge-localised AE with a frequency of 316 kHz and n = 13 for beam ions launched at $\rho = 0.25$. Resonance map for (a) $p = 0$ to 3 having two regions of resonance similar to 6.4a (b) the extended resonance region with $p = 6$, (c) movement of resonance region towards higher energy for $p = 7$ and (d) no resonance at $p = 8$.

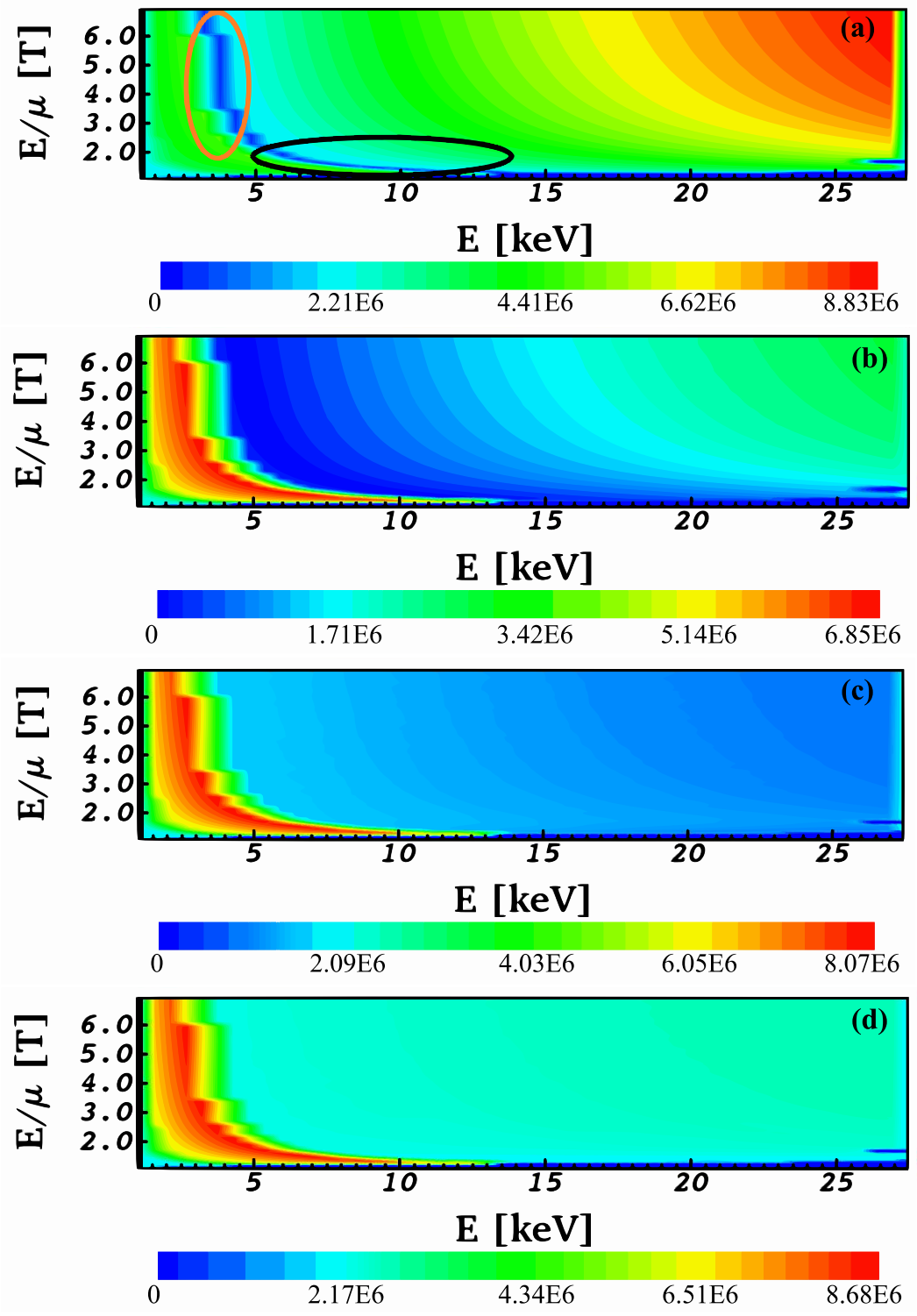

Fig. 6.6 Resonance maps for the same mode as shown in 6.5 with n = 17. Resonance map for (a) $p = 0$ to 5 having two regions of resonance similar to 6.5a (b) the extended resonance region with $p = 8$, (c) movement of resonance region towards higher energy for $p = 10$ and (d) no resonance at $p = 11$.

Figure 6.7 shows the orbits for two selected resonant fast ions as given by DELTA5D code in the drag and diffusion dominated regions of figure (6.4a). Similar fast ion orbits were previously obtained with the ISDEP code for TJ-II [75, 76]. The modelled orbits are broadly similar in both regions and exhibit full sampling in both the poloidal and toroidal directions.

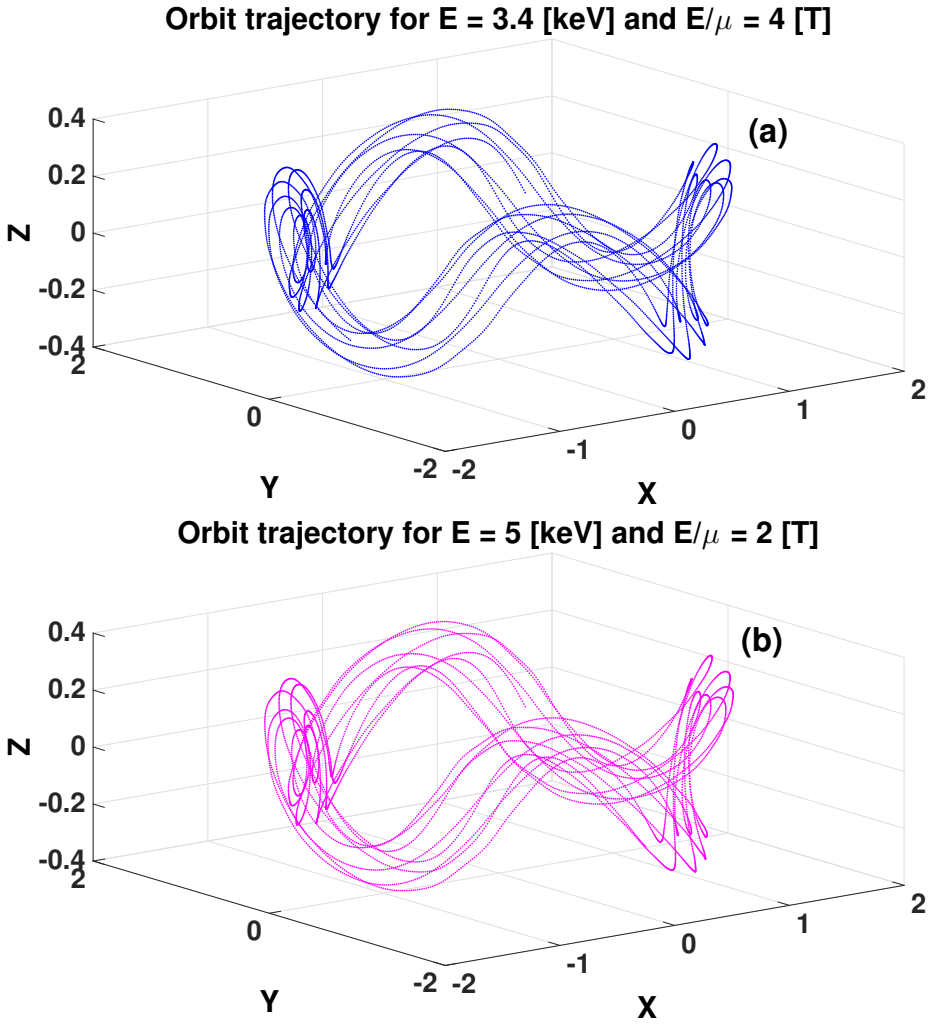

Fig. 6.7 Orbit trajectories of two fast ions launched at $\rho = 0.25$ in TJ-II that are resonant with the core-localised AE with a frequency of 306.57 kHz and $p = 0$ and n = 11. (a) The orbits with E = 3.4 keV and $E/\mu = 4$ T are those from Regions 1 and (b) the orbits with E = 5 keV and $E/\mu = 2$ T are those from Regions 2, of the resonance map shown in figure(6.4a).

It was found earlier in [77, 78] that the type of the replenishment (by drag or by diffusion) of an unstable energetic particle distribution determines the nonlinear evolution of energetic particle-driven modes. In particular, it was shown that the

drag-dominated distribution at the resonance could not give a steady-state evolution of the mode. Further development of this theory was performed recently [79] to include two species of the beam ions, one of which is reconstituted in the resonance area by drag only, and the other by diffusion only. New nonlinear scenarios of the mode evolution were found and, in particular, a transition from the steady-state nonlinear AE evolution to the sweeping frequency (chirping) AEs as the proportion between the two types of the resonating ions was varied slightly. It could be of particular interest for future studies to investigate whether the iota variation in TJ-II experiments could affect the proportion between the resonant beam particles in area I (drag-dominated region) and area II (diffusion-dominated region) so the scenario observed in [79] is reproduced.

6.4 Conclusions

We have displayed resonant wave-particle interaction (WPI) for the TJ-II plasmas utilizing Monte Carlo transport model i.e. DELTA5D code [70, 71]. This model calculates an enhanced energy transfer between the trapped energetic particles and resonant wave. In these calculations a modelled global Alfvén mode with $n = 11$ and varying bounce harmonic p having frequency 306.57 kHz is considered for the calculation of resonance function Ω using resonance condition. In our simulations, it is found that if an energetic ion beam is launched relatively more radially outward i.e. at higher ρ values then the 2D matrices for poloidal and toroidal frequencies of the drift orbits allow an expansion in the area of unconfined beam ions, effectively pushing the phase space area of confined beam ions down to lower energies. Using the calculated poloidal orbit frequency and the toroidal precession frequency, one can compute resonance function by combining their 2D functions in Equation (6.1) for various integer values of p and for the frequency and toroidal mode number of the AE of interest. In these calculations the corresponding wave-particle resonance maps suggest for low bounce harmonics (p) the possibility of describing the non-linear evolution of the AEs in TJ-II by a sum of two ion populations with different weighting factors, one of which is dominated by drag and the other by diffusion. As the bounce harmonic increases, the resonance region starts to expand and can cover over a significant area of the particle phase space until this resonance region vanishes at high bounce harmonics. The modelled orbits from each of the drag and diffusion sections of the resonance function are identical in TJ-II stellarator and are compatible with the previous orbit calculations [76].

Chapter 7

Shear Alfvén wave continuum spectrum with bifurcated helical core equilibria in tokamak plasmas

In this chapter Shear Alfvén continuum calculations are discussed due to the formation of helical core structures in tokamak plasmas. In axisymmetric devices such as tokamaks, at higher pressure internal-kink-like mode saturates around the magnetic axis and forms helical structure while reaching an equilibrium state by modifying axisymmetric (2D) equilibrium into the 3D equilibria. Investigations of the Alfvén modes in the presence of such internal 3D structures are important due to presence of the strong magnetic field at magnetic axis may affect the fast ion population. This work has been published in:

[80] **A. Rakha** et al., Shear Alfvén wave continuum spectrum with bifurcated helical core equilibria, *Accepted in Nuclear Fusion August 2019*

7.1 Overview

The radial structure of the continuum spectrum of shear Alfvén and Alfvén-acoustic waves in the beta-induced Alfvén eigenmode (BAE)frequency range is modeled for tokamak plasmas in the presence of 3D effects obtained from the bifurcated MHD equilibrium reconstruction. Plasma compressibility and geodesic curvature effects responsible for the low-frequency continuum spectrum calculations are invoked. In the equilibrium calculations we find that the helically distorted MHD equilibria may exist even for the axisymmetric devices if q = 1 rational surfaces are present. The continuum

calculations with the bifurcated equilibria lead to a frequency splitting between the highest frequency branch and the lowest frequency branch continua at the frequency accumulation point. Radially localised shifting of modes happens via coupling of the adjacent n-1 continuum around an accumulation point. Our modelling (including 3D effects) correctly reproduces the phenomenon of continuum frequency splitting and provides a possible solution for the differences of few kHz in frequency splitting, which remained unexplained with the 2D kinetic calculations (**D. Curran** etal. 2012 Plasma Physics and Controlled Fusion **54** 055001). The pressure scaling confirms the increase of helical excursion of the magnetic axis in equilibrium reconstruction and hence the range of continuum frequency splitting. In our calculations, the existence of low-frequency continua is in agreement with the experimentally observed low-frequency modes.

7.2 Introduction

In fusion plasmas, fast ions in the MeV energy range may have velocities comparable with Alfvén velocity directed along the magnetic field lines, which can satisfy conditions of effective resonance and energy exchange between Alfvén waves [81]. Shear Alfvén Waves (SAW) form a continuous spectrum which in the presence of symmetry breaking non-uniformities such as toroidicity or ellipticity is modified to exhibit Alfvénic gaps. In this context two types of Alfvénic instabilities exist: (1) energetic particle continuum modes (EPMs)[82], dwelling in the Alfvén continuum and having frequencies in the range of the continuum and (2) discrete Alfvén eigenmodes (AEs) [83] with frequencies inside the SAW gaps. Given the strong continuum damping due to the collisionless dissipation of SAWs in non-uniform equilibria and their low absorption threshold for entering into an unstable state [84, 85], the question arises about the significance of continuum radial structures for the tokamak stability problem. Understanding the impact of the helical core on the modification of SAW continua may have potential implications for Alfvénic instabilities in burning plasmas and identify new issues in approaching the ignition margin.

In tokamak plasmas, the SAW continuum gets modified due to the interaction with low frequency MHD fluctuations, such as magnetic island and helical core. Previously, theoretical investigations for the Alfvén continuum have been made in the presence of magnetic islands [86]. In this chapter, we have tried to investigate the effect of the helical core on the continuous spectrum. The helical core is an internal three-dimensional (3D) structure in non-uniform axisymmetric MHD equilibria regarded as

a saturated ideal internal kink mode and/ or a deformation of the magnetic axis. The helical excursion of the magnetic axis in a tokamak equilibrium appears because of the peaked pressure profile in the presence of a safety factor q passing through unity. The bifurcated equilibria are the combination of an axisymmetric part and a spontaneously triggered internal helical distortion of the magnetic axis, which are also called snakes in tokamaks [24] and in reversed field pinches (RFPs) single helical axis states (SHAx) [87]. The 3D helical deformation of the equilibrium destroys the symmetry properties of the tokamak. In highly elongated plasmas, the disappearance of sawtooth oscillations and the persistence of a saturated ideal internal kink m = 1, n = 1 mode with q is in the vicinity of unity also can cause the existence of such helical deformations [88]. Plasmas with such special conditions are called hybrid plasma scenarios [89], which often trigger Alfvénic magnetohydrodynamic (MHD) instabilities such as EPMs [90], long-lived modes (LLMs) [91], and internal kinks or fishbones. Studies have shown that the 3D helical distortion during hybrid scenario operation is very large, which is confirmed by a complete flattening of strong NBI induced toroidal flow in the core region [92]. When the helical equilibrium is formed by an internal kink m = 1, n = 1 mode, the fast ions orbits become more complex with stonger radial drifts [91, 92].

In fusion plasmas, the sawtooth crashes are associated with the appearance of MHD instabilities such as saturated internal kinks [93] and continuous modes [94]. Studies have shown that the sawteeth disappear or transform into internal kink-like modes [93]. Observation of the low-frequency MHD modes during a sawtooth crash in ASDEX Upgrade (AUG) discharges has motivated employing saturated internal kink-like modes as helical distortions for further investigations of Alfvénic instabilities. AUG is a medium size divertor tokamak with a major and minor radius of 1.65 and 0.5 meters, respectively. At AUG, various ICRH-driven instabilities in the BAE and sub-BAE frequency range have been observed during monster sawtooth crashes [95, 96]. Understanding these instabilities, their impact on EP transport and their importance on sawtooth stabilisation is an outstanding issue in the view of predicting the sawtooth cycle properties in various ITER scenarios. In reference [96] a careful kinetic analysis has been carried out in order to understand the complex frequency evolution of these modes during a sawtooth cycle. Most of the aspects have been clarified such as the origin of the low ($\sim$ 10kHz) and high ($\sim$ 70kHz) frequency branches, the mode number inversion (higher toroidal mode numbers appear at lower frequencies) and the frequency evolution during the sawtooth cycle. The gyro-kinetic dispersion relation [95, 97, 98] has been solved with the LIGKA code [98, 99] and compared to experimental measurements highlighting the importance of a kinetic analysis, in particular the role of diamagnetic

effects [96]. However, 3D effects had not been included, and the question arises as to whether the presence of a helical core can modify the shear Alfvén continuum in a way to explain the remaining differences (see Fig. 7 and discussion at the end of section 2.4 of reference [96]).

So far, the effects of a helical core on calculations of Alfvén continuum have received very little attention. In our work, the helical core is modeled as a static helical distortion of the equilibrium because of its typical low oscillation frequency as compared with the SAWs in AUG. Bifurcated tokamak equilibrium states are modeled using a 3D ideal MHD equilibrium solver VMEC [31] and it is generally found that the m = n = 1 helical magnetic axis is displaced most at the position of q_{min} [91]. It is therefore clear that the Alfvén continuum needs to be modeled using a realistic 3D equilibrium magnetic field geometry. The shear Alfvén continuum is modeled by using an extended continuum solver (STELLGAP) [44, 45]. STELLGAP has been previously used for the modelling of continuum structures in stellarators [47, 67], RFPs [51] and tokamaks [16]. It is based on the reduced MHD model for 3D devices including effects of finite plasma compressibility and geodesic curvature. An equivalent set of reduced MHD equations for the low beta plasmas have been earlier used in similar tools COBRAS [100] and CONTI [49, 50] for the modelling of sound-Alfvén continua of 3D systems. Low frequency gaps in SAW continuum opened by the plasma compressibility and geodesic curvature are responsible for BAEs and beta-induced acoustic-Alfvén modes (BAAE). Coupling of the SAW with helical core distortion forms a linear model of SAW dynamics in a non-uniform equilibrium.

This chapter is organized as follows. In section 7.3, the experimental details of the AUG discharges are provided. In section 7.4 the details of the reconstruction of 3D helical core MHD equilibria are provided. Alfvén continuum calculations for the 2D and 3D equilibria are provided in section 7.5 and, finally, the summary and conclusions are provided in section 7.6.

7.3 Experimental Observations

At the AUG tokamak experiments were conducted to investigate the low-frequency Alfvén instabilities. It has been observed that these modes appear during the sawtooth cycle and in the region surrounding with q = 1 surface [95]. The appearance of low-frequency modes around the region of q = 1 during sawtooth cycle suggests possible helical core formation. In order to estimate the upper limit of the effect of the helical core, an AUG discharge #20488 with monster sawtooth crashes is chosen. This

discharge dates back to 2005 when the vessel wall was only $\sim 50\%$ covered with tungsten W tiles. Similar discharges were repeated in 2009, however the sawtooth period was shorter and the pressure gradient at q = 1 before the sawtooth was slightly smaller, which has led us now to perform a pressure sensitivity scan in these calculations.

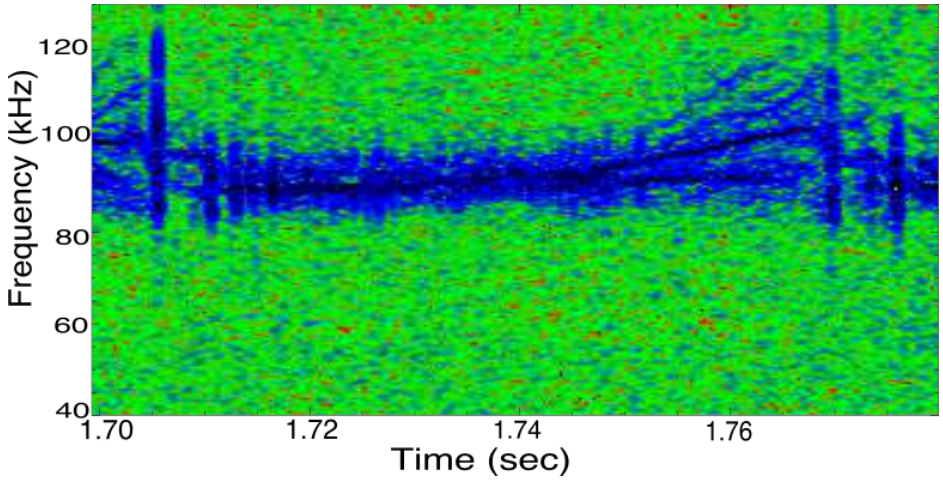

Fig. 7.1 Frequency spectrogram for discharge #20488 from t = 1.72 to 1.78 seconds. Strong BAE mode activity during monster sawtooth crashes is measured with Mirnov coils.

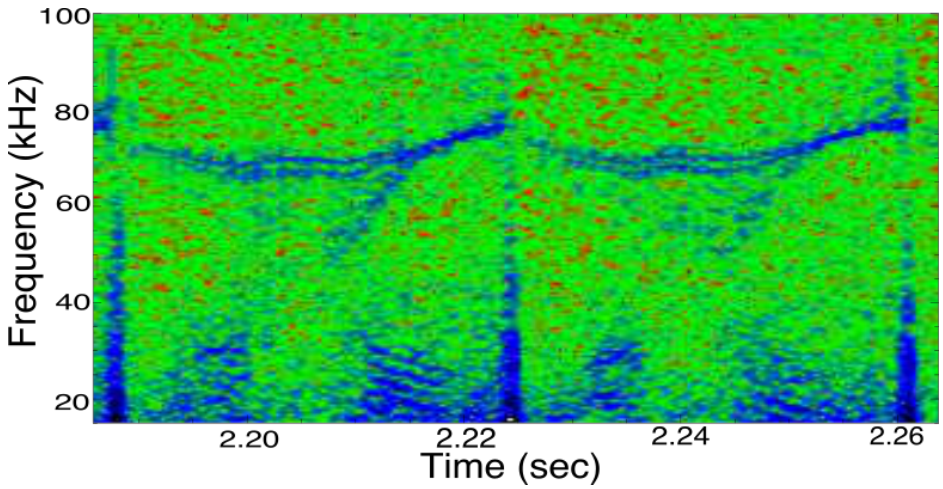

Fig. 7.2 BAE and low-frequency mode activity for discharge #25546 from t = 2.0 to 2.265 seconds measured with the core-localized soft X-ray channels.

In Figure 7.1, the BAE mode evolution in discharge #20488 as measured with magnetic diagnostics is displayed. At this time high resolution Soft X-Rays (SXR) system was not available. In the case of discharge #25546 the BAE and low-frequency

modes measured with the core SXR channels are shown in Figure 7.2. The classification of the observed modes as BAEs and low-frequency modes and the splitting of several modes using the kinetic model has already been provided in [96]. The detailed experimental findings for the discharges #20488 and #25546 are published in [95] and [96] respectively.

In Fig. 1 of reference [96] the low-frequency mode activity during two sawtooth cycles from t = 1.91 to 1.98 s for discharge #25546 as measured with a core ($\rho \approx 0.24$) soft x-ray channel is shown. In these results ρ is a normalized radial parameter defined as $\rho = \sqrt{\psi_{pol}}$ and ψ_{pol} is the normalized poloidal flux. Here, we focus on the high-frequency BAE branch at $\sim 70kHz$ with the toroidal mode numbers n = 3 to 6. One can observe that the mode frequencies directly after a sawtooth crash are almost degenerated, whereas during the sawtooth cycle they start to split. This observation has been explained with the raise of the pressure gradient and the corresponding downshift of the kinetic continuum (see Fig. 12 of reference [96]). This implies that higher mode numbers are shifted downwards more strongly than lower mode numbers. Towards the end of the cycle, the mode-frequency splitting starts to disappear, probably due to the sawtooth precursors, as discussed in section 2.4 of reference [96]. Despite the success of this model, it is interesting to try to understand the remaining differences of 2 to 5 kHz in frequency splitting, especially towards the end of the sawtooth cycle. It should be noted, that it is assumed that the evolution of the BAE continuum accumulation point is a proxy for the evolution of the global BAE mode [101]. Based on an ASDEX Upgrade equilibrium reconstruction for discharge #20488 (and the practically identical discharge #25546 discussed in [96]) a pressure scan is performed that is intended to model the increase in the core pressure after a sawtooth crash.

7.4 Bifurcated MHD equilibrium reconstruction

The saturated internal-kink mode is dominated by m = 1, n = 1, surrounding the magnetic axis and leads to the helical equilibria. They distort the symmetry properties in the plasma core area by forming a 3D helical core surrounded by an axisymmetric 2D mantle. Plasma equilibria with a 3D helical core and axisymmetric boundary are defined as bifurcated helical equilibrium states.

In our studies, we have modeled a bifurcated helical equilibrium by introducing a small perturbation in the magnetic axis for AUG-tokamak discharge #20488, which has q in the vicinity of unity in the core region of the tokamak. Two sister equilibria, one axisymmetric and another helical are calculated simultaneously using an identical

boundary with the VMEC code [31]. The q-profile of the discharge #20488 presented in Figure 7.3 is used as an input to the VMEC code together with the plasma boundary, peaked pressure profile (Figure 7.4) and an initial perturbation in the magnetic axis. The q-profile in Figure 7.3 shows the extended region of low shear up to $\rho = 0.4$ and q close to one. These are the principal requirements for the formation of a helical core.

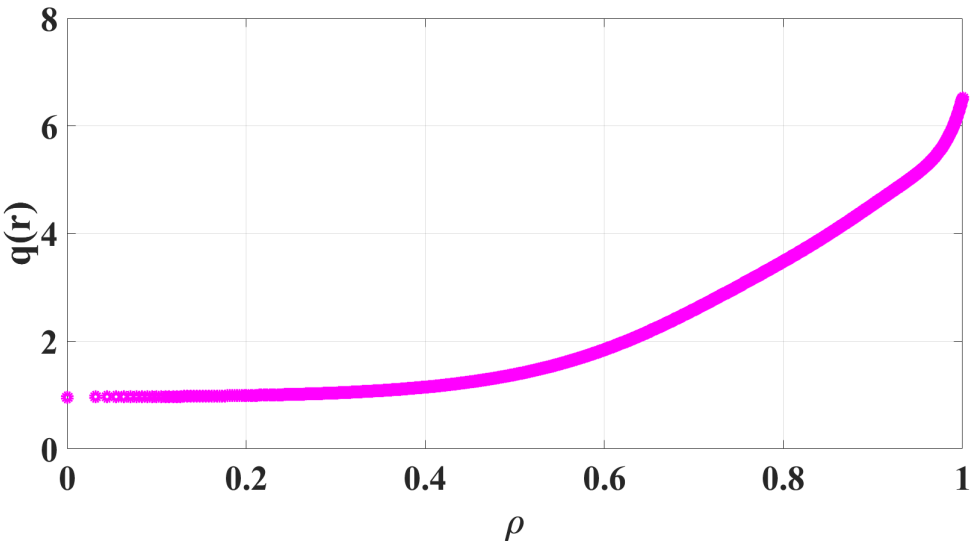

Fig. 7.3 Safety factor (q) profile of ASDEX-Upgrade discharge #20488.

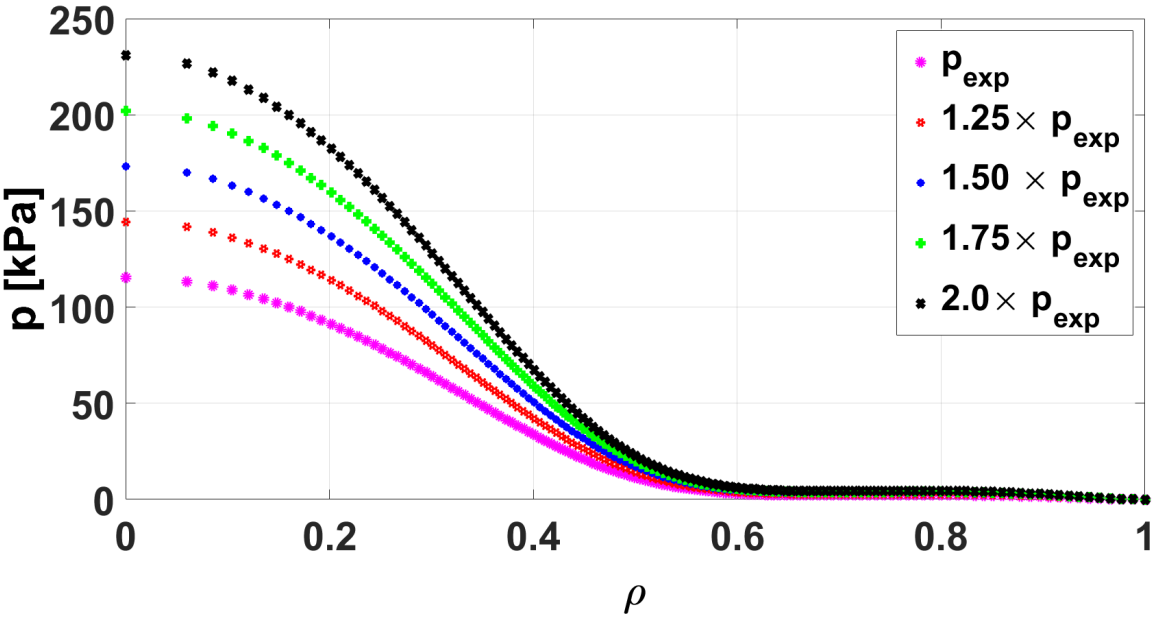

Fig. 7.4 Plasma pressure profile of AUG discharge #20488. Here p_{exp} is the experimental pressure and remaining four profiles are the scaled pressures.

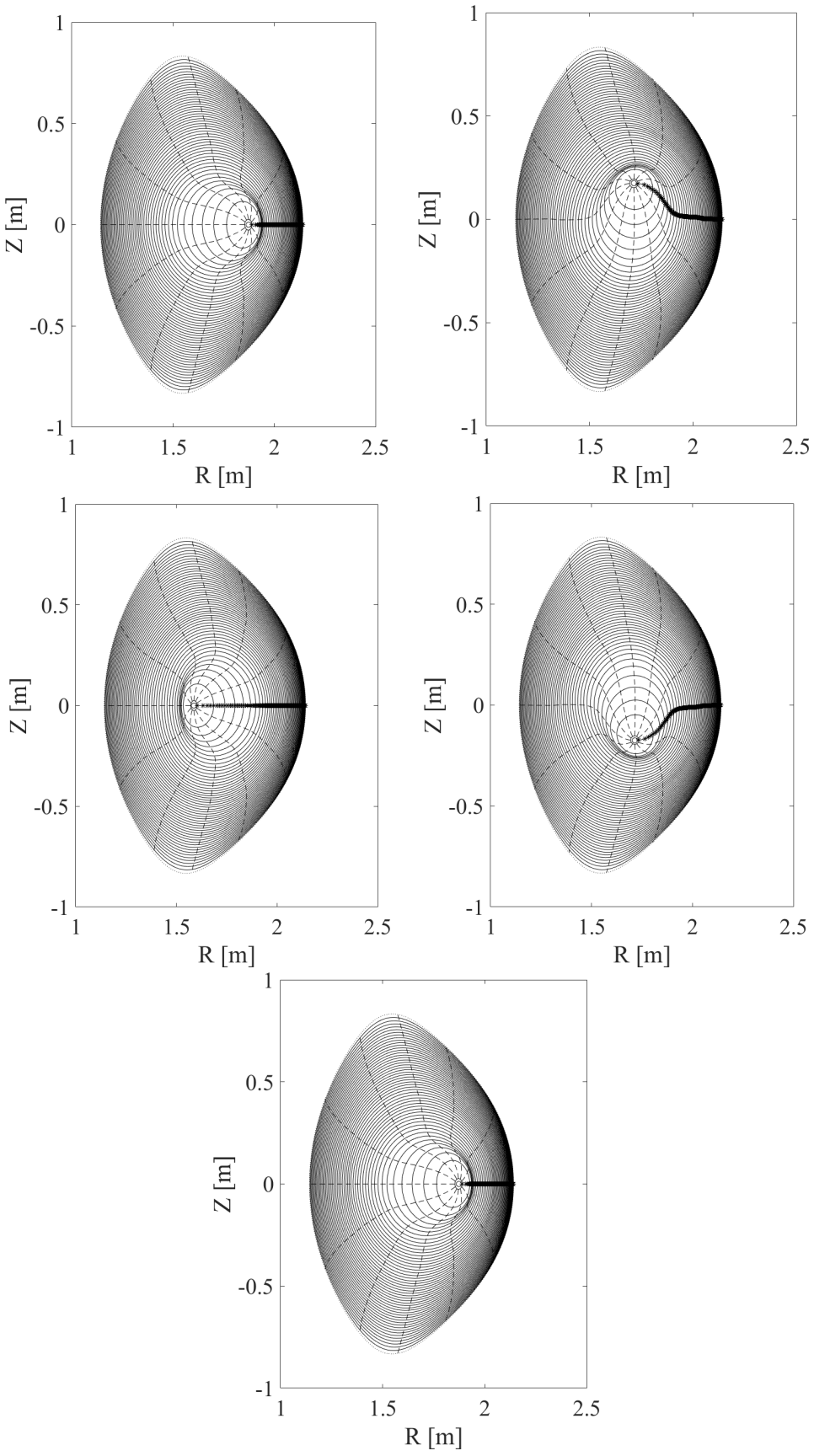

Fig. 7.5 Poloidal cross-section of the toroidal magnetic flux surfaces for helical core equilibria with $\delta_H = 0.37$ at five toroidal angles $\phi = 0$, $\pi/2$, π, $3\pi/2$, 2π (left to right). The deformations in flux surfaces are helical excursions of the bifurcated equilibrium while preserving the plasma boundary

The reconstructed equilibrium having the bifurcated behavior can be assessed through the progression of modified magnetic flux surfaces. The magnetic flux surfaces are plotted in the Figure 7.5, which clearly shows modifications in those flux surfaces around the torus, which are clear signals of the helical core formation near the magnetic axis. The saturated state of the magnetic axis can be characterized as an m = 1 and n = 1 perturbation, the internal kink mode. It can be seen that while qualitatively the helical formation is similar, it changes its orientation along the toroidal angle. In comparison with these flux shape variations, the axisymmetric equilibrium calculations display continuous magnetic flux surfaces with no deformation across the whole torus as shown in Figure 7.6. In these calculations, identical pressure, inverse rotational transform (q-profile) and plasma boundary are imposed. The only difference is the removal of the seed perturbation of the magnetic axis, which is added for the helical core calculations to allow the magnetic axis transform to a saturated internal-kink mode, if necessary conditions permit [23].

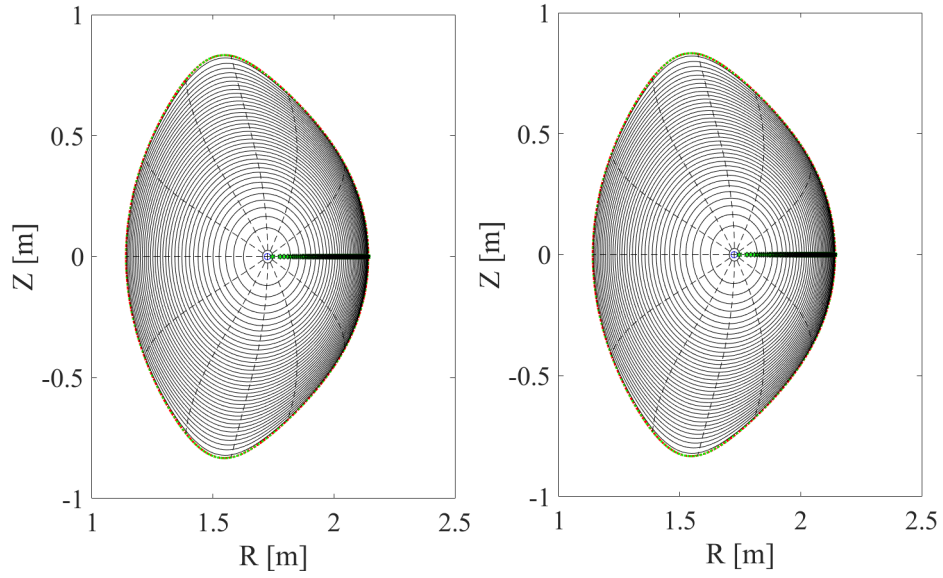

Fig. 7.6 Poloidal cross-section of the magnetic flux surfaces at two different toroidal angles $\phi = 0, \pi/2$ and $\pi/2, \pi$ for the axisymmetric equilibria. In axisymmetric equilibrium both contours have exactly matching flux surfaces and the magnetic axis. Here the magnetic axis is represented with blue and green colors.

In the comparison of magnetic flux surfaces contours at two different toroidal angles, the results for axisymmetric case are shown in Figure 7.6, which confirm the zero level of distortion in the flux surfaces. On the other hand, the 3D helical core comparison given in Figure 7.7 for the two identical toroidal angles provides the proof of relative excursion of magnetic axis due to helical core formation and simultaneous existence

of two equilibria solutions, one with helical equilibrium in plasma core and second with axisymmetric equilibrium in the rest of contour are confirmed. This comparison shows the qualitative excursion of the magnetic axis at two different toroidal angles and highlights the regions of closely packed magnetic flux surfaces due to the helical core formation.

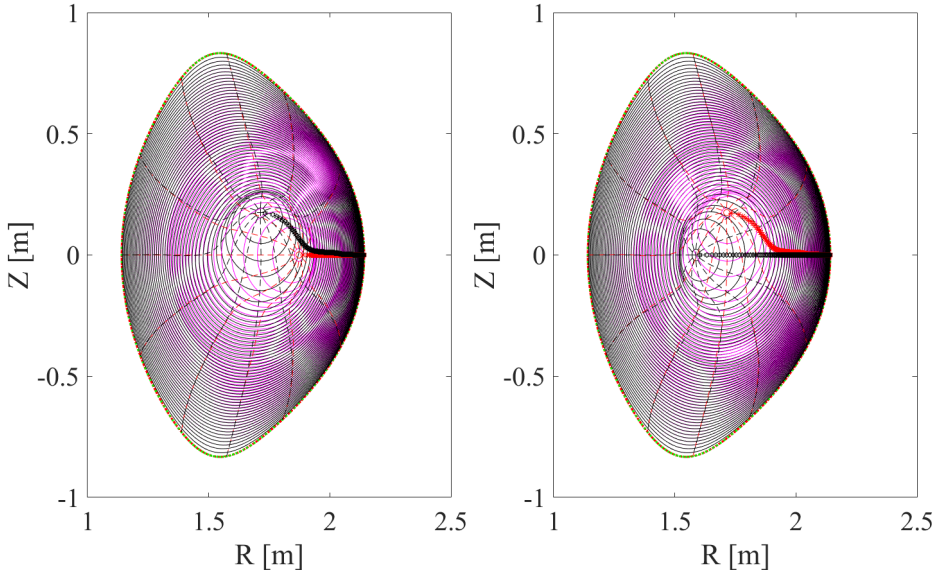

Fig. 7.7 Poloidal cross-section of the magnetic flux surfaces at two different toroidal angles $\phi = 0,\ \pi/2$ and $\pi/2,\ \pi$ helical core equilibria with $\delta_H = 0.37$. In both graphs, the excursion of the magnetic axis is clear and represented by red and black symbols and the magnetic flux surfaces are represented by magenta and black color lines. The red and black color dashed lines are the theta contours.

The convergence of the reconstructed equilibria has been investigated by using the volume averaged residual horizontal force F_R as a function of number of iterations as shown in Figure 7.8. The significant drop in F_R along the number of iterations confirms the convergence of helical core formation results. As in previous investigations [24], the normalized radial force balance given in the Equation (3.14) has been used as a diagnostics for the convergence of the equilibrium state by reaching to the value of the order of 10^{-8}. In our results, with the number of flux surfaces equal to 799, we have achieved a similar level of convergence in around 20 000 iterations for the experimental pressure. In the higher pressure calculations, we have used around 40 000 iterations to achieve the converged results for 500 radial grid points.

We have also modeled the excursion of the helical core δ_H defined in Equation (7.1) with the number of iterations. It is found that the helical core saturates at an identical number of iterations for different radial resolutions. In previous studies the saturation

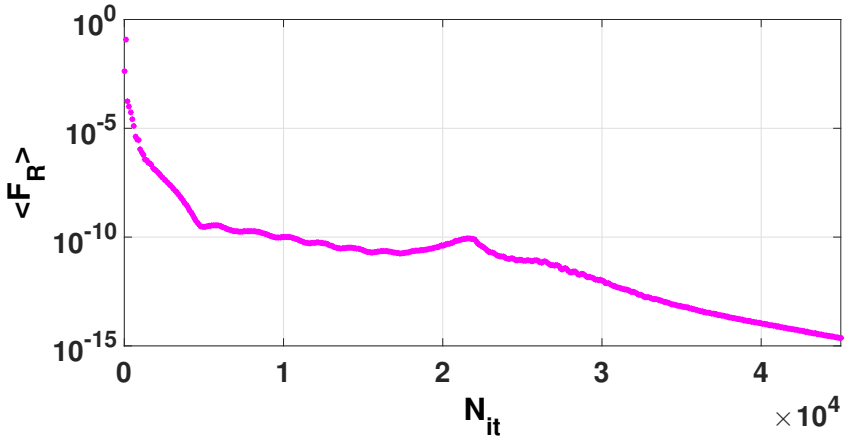

Fig. 7.8 The volume averaged horizontal force F_R evolution with number of iterations

of the helical core with a higher number of radial grid points [102] and the increase in the helical core with the increase in number of iterations [34] has been associated with the convergence of helical core equilibria. In our results presented in Figure 7.9, the helical core for the lower number of iterations remains smaller, and after reaching a sufficient number of iterations as defined by the threshold given in [102], it grows rapidly and eventually saturates. At this point the helical core becomes fully resolved.

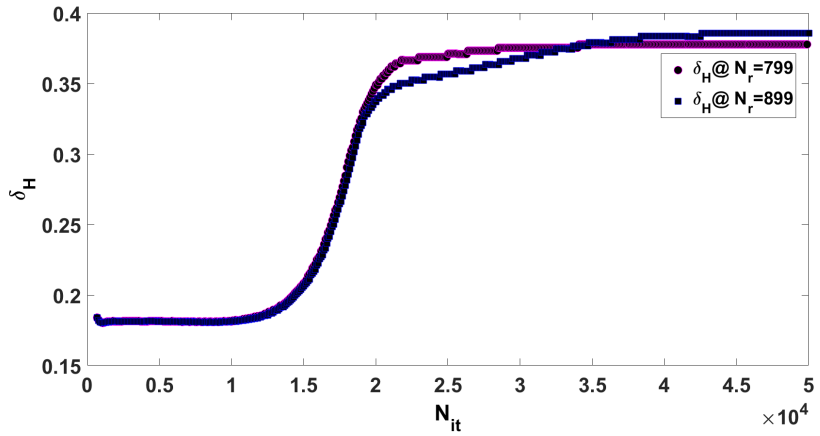

Fig. 7.9 Dependence of helical core size δ_H on number of iterations N_{it} for different levels of radial resolution N_r

The quantitative measure of the helical excursion of the reconstructed equilibria can be provided with a parameter δ_H [24] defined as

$$\delta_H = \frac{\sqrt{R^2{}_{01}(s=0) + Z^2{}_{01}(s=0)}}{a} \tag{7.1}$$

Here $R_{01}(Z_{01})$ corresponds to the Fourier amplitude of the $R\,(Z)$ components of the $m = 0, n = 1$ mode at the magnetic axis $s = 0$ ($a = 0.4$ meters is the effective plasma minor radius). In this work the helical excursion of the magnetic axis has

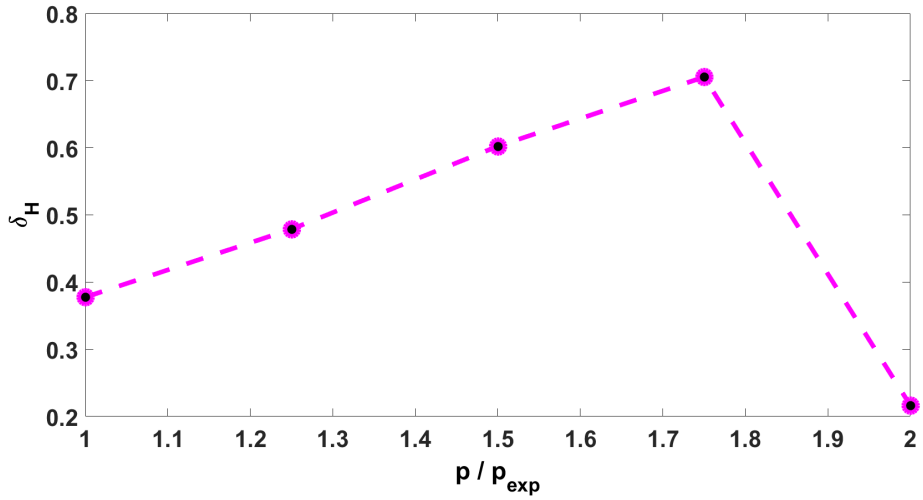

Fig. 7.10 The magnetic axis helical distortion parameter δ_H as a function of the pressure normalized to the experimental pressure.

been calculated with respect to the plasma pressure as shown in Figure 7.10, as the peaked plasma pressure has been considered an important parameter in the formation of helical structures. Results computed with fixed boundary equilibrium calculations, show that the helical excursion of the magnetic axis increases with the increase in the plasma pressure up to a certain limit, from $\delta_H = 0.37$ for the experimental pressure to $\delta_H = 0.7$ for 1.75 times of the experimental plasma pressure. When the plasma pressure is increased further, the helical excursion decreases due to the fixed boundary nature of the equilibrium calculations. In a fixed boundary equilibrium model, the Shafranov shift at the maximum plasma pressure already distorts the magnetic flux surfaces strongly enough and leaves no room for their further stretching. Therefore, a further excursion of the helical core is not possible at the higher plasma pressures.

7.5 Alfvén continuum results and discussions

Alfvén continuum calculations have been performed for the experimentally observed radially extended low-shear q-profile plasmas using axisymmetric and non-axisymmetric MHD equilibria as discussed in section 7.4. Two different cases, one with axisymmetric (2D) and the second one with helical (3D) equilibria have been investigated. In Alfvén continuum calculations the parallel plasma compressibility $\gamma = 1.6$ is employed for the

low frequency Alfvén continuum calculations. In these calculations, we have limited the selection of toroidal mode numbers (n) from 1 to 6, since a similar range of n was measured in the experiments.

7.5.1 Alfvén continuum calculations with axisymmetric 2D equilibria

Axisymmetric equilibrium calculations for tokamaks are straightforward because ideal tokamaks are inherently axisymmetric (2D) devices. Alfvén continua using an axisymmetric equilibrium are calculated for n = 1 to 6. The Alfvén continuum structures for the full radial extent and frequencies up to 475 kHz are shown in Figure 7.11.

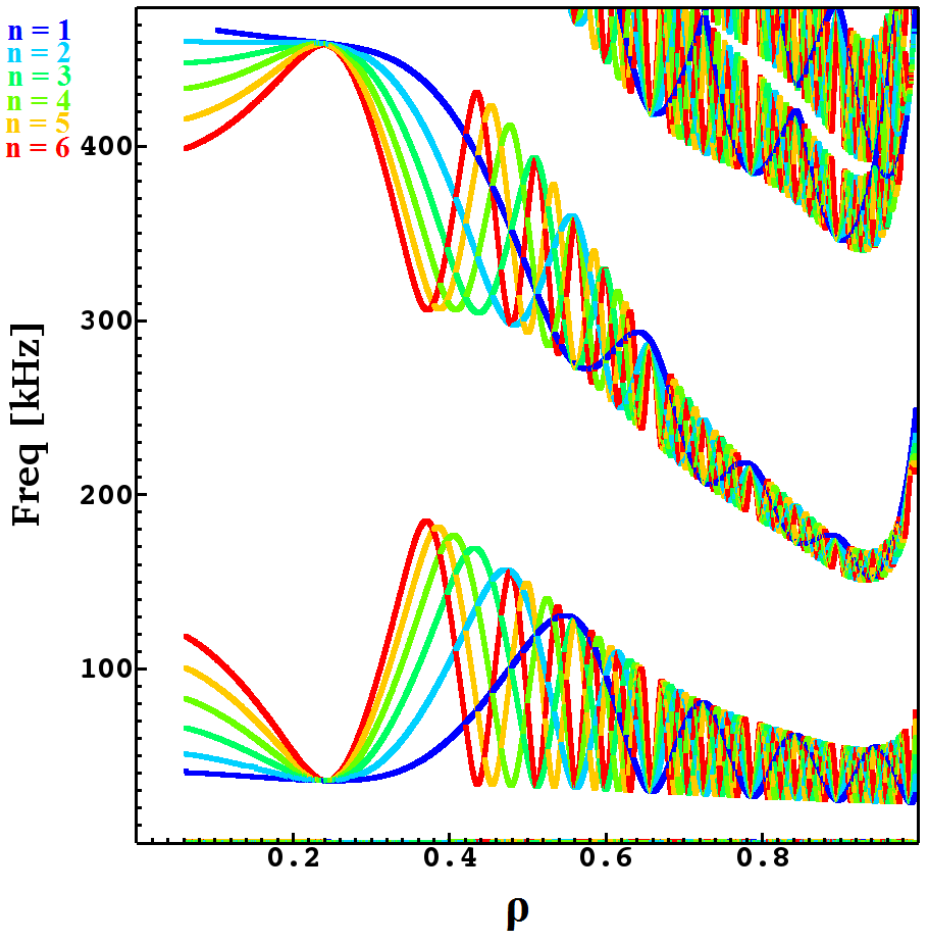

Fig. 7.11 Alfvén continuum structures with axisymmetric (2D) equilibrium for discharge #20488.

In these continuum structures a frequency gap appears in the full plasma column. The gap is wide in the core and becomes narrower towards the edge. These structures are similar for all toroidal mode numbers, including their resonant extrema points.

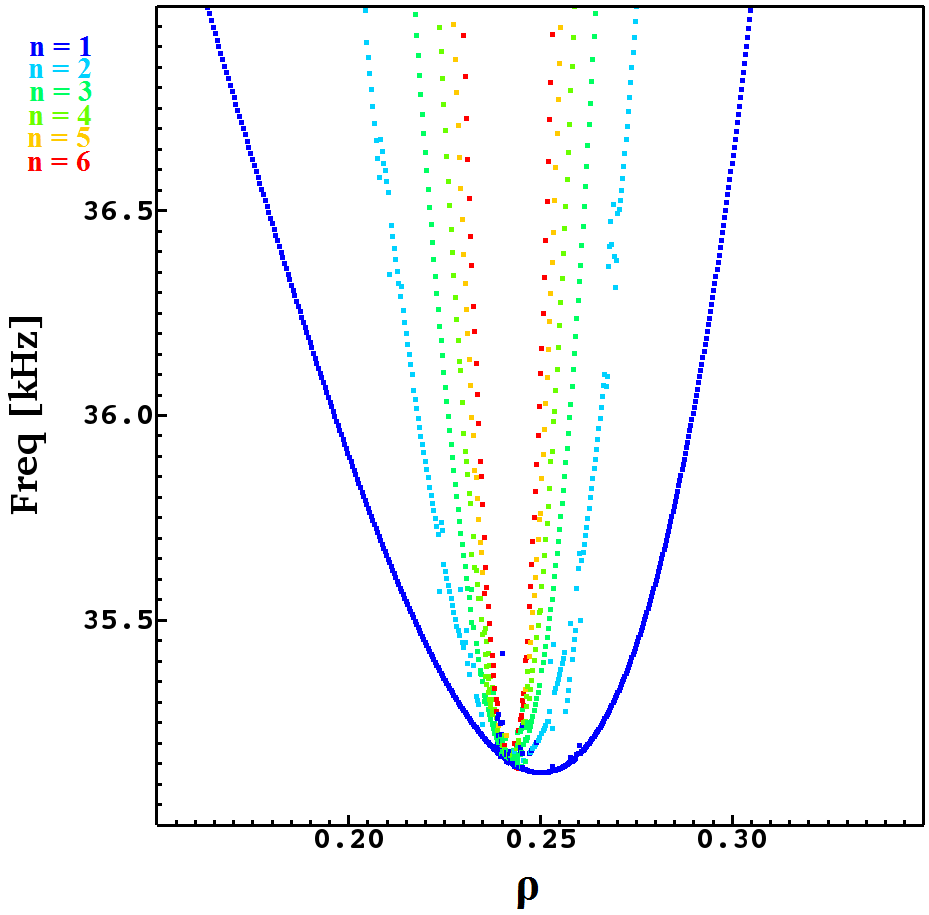

Fig. 7.12 Zoom of Alfvén continua in Figure 7.11. Different colors represent the corresponding toroidal modes number (n)

For the six toroidal mode numbers considered here, the Alfvén continuum structures at $\rho \approx 0.23$ approach an accumulation point as shown in Figure 7.11 around the q = 1 rational surface exhibited in Figure 7.3. Zooming in on these structures in Figure 7.12 shows that all continua accumulate around a single frequency of 35 kHz and there is no splitting in the frequency range. These characteristics of non-splitting frequency at the accumulation point around rational surfaces are the hallmarks of axisymmetric continua. Here, we define frequency splitting (Δf) as the difference between the highest frequency branch and the lowest frequency branch in the continuum structures around the frequency accumulation point caused by the 3D effect of the helical core. We will study this frequency splitting in detail in section 7.5.2 below.

It should be noted that in the experiment the BAE mode frequency was observed at 60-70kHz. The remaining difference after taking into account the Doppler shift $\sim$ 3kHz [96] can be attributed to a different model for the plasma compressibility: here the value of $\gamma = 1.6$ is used where as in [96] the more sophisticated kinetic expression was used. Nevertheless, the frequency splitting due to 3D effects is not expected to change significantly due to the choice of this parameter.

7.5.2 Alfvén continuum calculations with bifurcated helical core equilibria

The continuum structures using helical 3D equilibria have been investigated for the same discharge for the five different pressures (Figure 7.4) as discussed in the section 7.4.

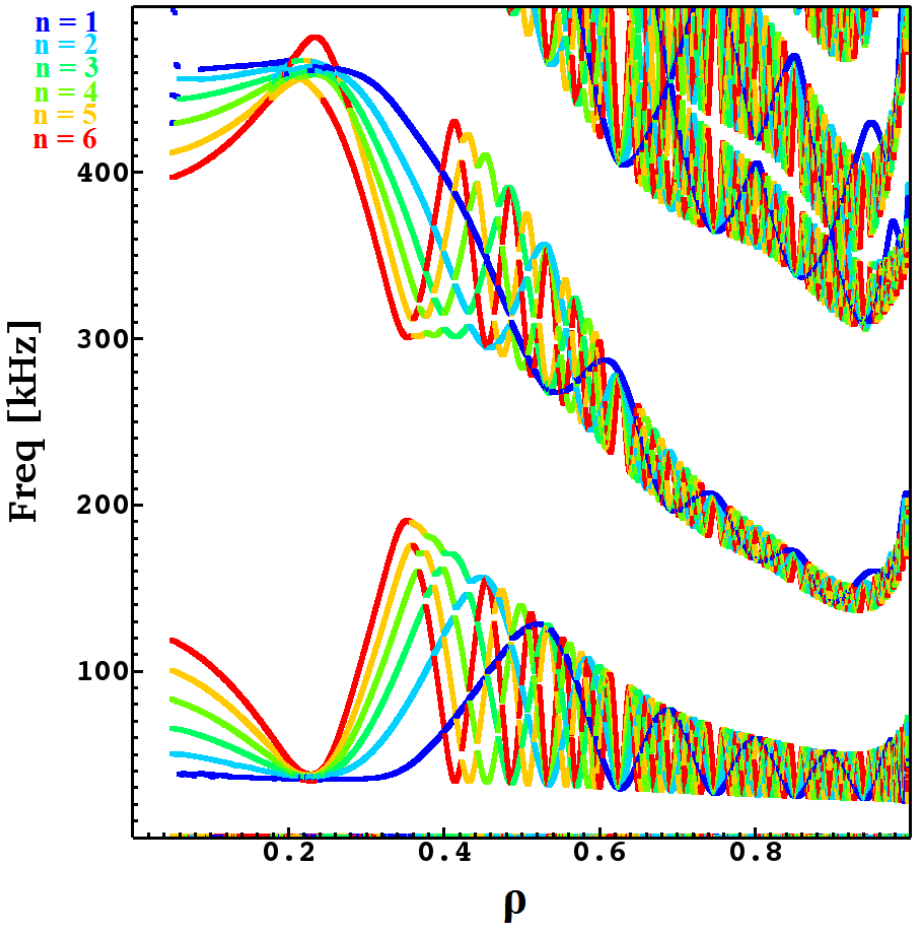

Fig. 7.13 Alfvén continuum structures with 3D helical core equilibrium having $\delta_H = 0.37$ for discharge #20488

The helical core excursion shown in Figure 7.10 is strongly dependent upon the plasma pressure. The Alfvén continuum calculations are performed to investigate the effect of helical core size, since in the experimental investigations a peaked pressure profile was measured after the sawtooth crashes. Simulation results of Alfvén continua for the experimental pressure with an m = 1, n = 1 helical core and $\delta_H = 0.37$ are presented in Figures 7.13 and 7.14. For the maximum achieved helical core size of $\delta_H = 0.7$ the Alfvén continua are presented in Figures 7.15 and 7.16.

There are a number of significant differences in the Alfvén continua computed using bifurcated MHD equilibria with the Alfvén continua computed using an axisymmetric equilibrium. They include: frequency splitting in Alfvén continua, shifting of the modes at the frequency accumulation point and the appearance of helical Alfvén eigenmodes (HAE) gaps. In following, we discuss the differences in detail.

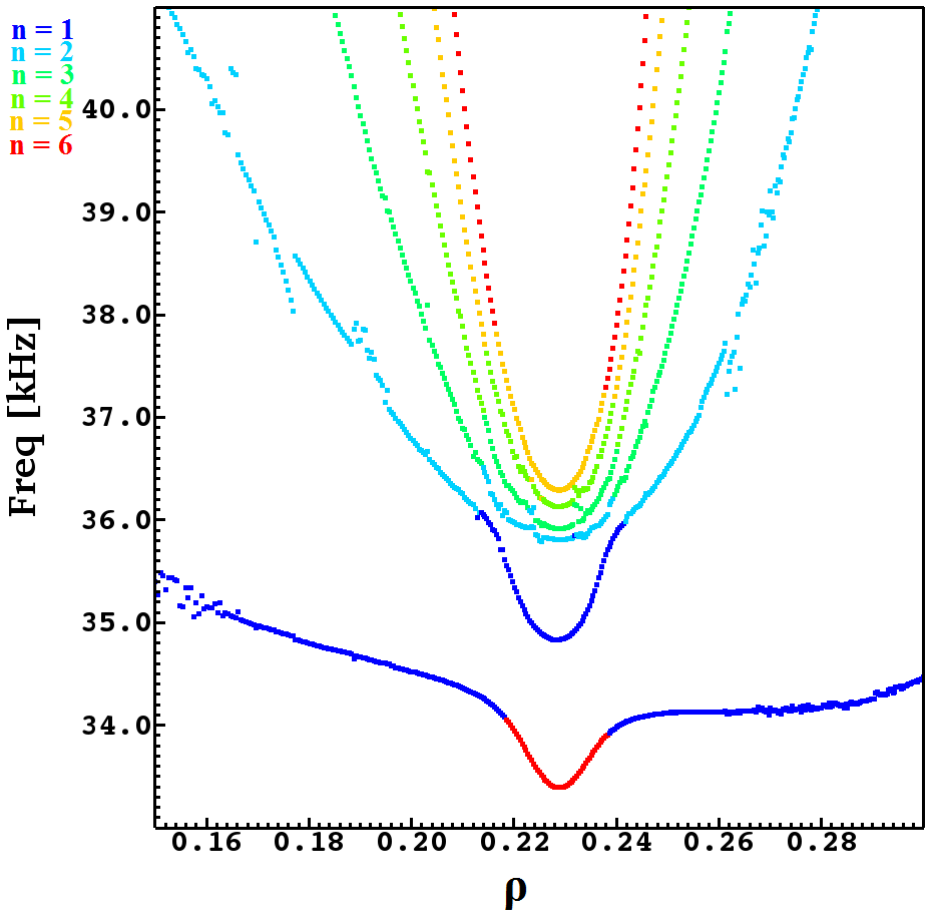

Fig. 7.14 Zoom of Alfvén continua in Figure 7.13. Different colors represent the corresponding toroidal modes number (n)

Alfvén continua computed using helical equilibrium and having exactly equivalent plasma parameters as the axisymmetric calculations is shown in Figure 7.13. Around the frequency accumulation point at $\rho \approx 0.23$ there is a noticeable splitting in the frequency range of continua as shown in Figure 7.14. Following the definition of frequency splitting, we have the highest frequency branch at f = 36.4 kHz with toroidal mode number n = 5 and the lowest frequency branch at f = 33.4 kHz with toroidal mode number n = 6, resulting in Δf = 3 kHz. The radial shifting in the mode structures via coupling to the n-1 continuum structures around an accumulation point is also clearly shown in Figure 7.14 e.g. a mode n = 1 converts to an n = 6 mode in the range $0.218 \leq \rho \leq 0.238$, then it reverts back to a n = 1 mode at higher ρ.

The radial shifting in mode structures is associated with the change in $k_{\|}$ due to the 3D excursion of magnetic axis. Due to the helical contribution, for the small $k_{\|}$ at the accumulation point, the smaller non-axisymmetric sideband terms compete with the axisymmetric terms and become prominent. Close to $k_{\|} = 0$ they become more significant. This prominence of non-axisymmetric sidebands at smaller $k_{\|}$ values leads to a radial shifting of modes around the accumulation point.

In figure 7 of [96], the shifting of the Alfvén continua relative to each other have also been modeled using a kinetic Alfvén model. They observed that the modes with higher n were shifted downwards after a few seconds of observation due to the strong diamagnetic frequency. Similarly, we have computed the shifts in Alfvén continua around the frequency accumulation point with the formation of helical core equilibria with a saturated 3D magnetic axis.

For the extreme helical excursion of $\delta_H = 0.7$, which happens at 1.75 times the experimental pressure, the computed Alfvén continuum structures are presented in Figure 7.15. In this case, the frequency gap around the plasma axis decreases by 20 kHz as compared with the Alfvén continuum calculated at the experimental pressure and helical core equilibria (Figure 7.13). The maximum frequency of the Alfvén continuum drops to 410 kHz from 475 kHz with minimum of 32 kHz. The splitting in the frequency range around the accumulation point $\rho \approx 0.23$ has also increased to 5 kHz, which corresponds to the difference between thethe highest frequency branch f = 32.6 kHz with toroidal mode number n = 4 and the lowest frequency branch f = 27.6 kHz with toroidal mode number n = 1 as shown in Figure 7.16. In our analysis, for lower (δ_H = 0.37) as shown in figure 7.14, the continuum of each n is shifted with the adjacent lower continuum of $n - 1$ around the frequency accumulation point. Only the continuum of $n = 1$ changes with the continuum of $n = 6$ due to our selection of a maximum toroidal mode of n = 6 in the STELLGAP code. In figure 7.16 with strong helical deformation

($\delta_H = 0.7$) this type of mode transitioning around the accumulation point from n to n-1 no longer holds, this can be due to the stronger helical distortion resulting in further radial stretching of the accumulation point. The radial drift of the accumulation point is associated with the increase in the Shafranov shift due to the higher plasma pressures [103].

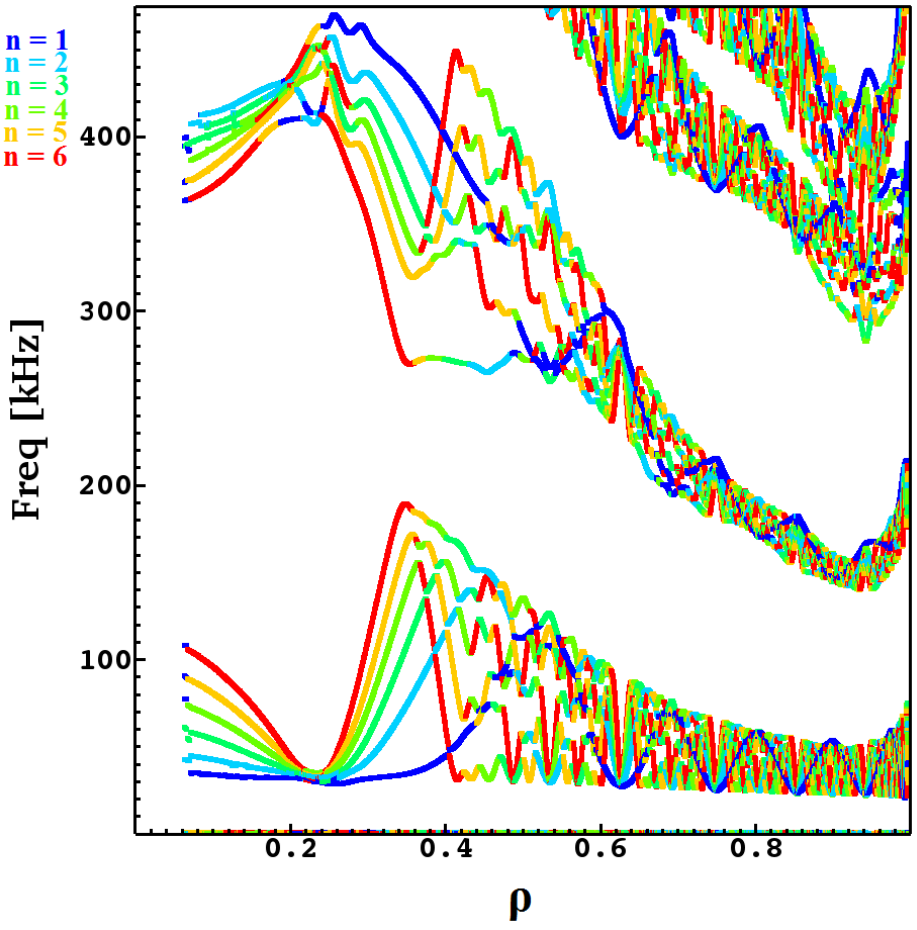

Fig. 7.15 Alfvén continuum structures with 3D helical core equilibrium having $\delta_H = 0.7$ in discharge #20488, where pressure is scaled to 1.75 times

Coexistence of modes with similar n over a significant radial extent is associated with the existence of radially extended rational surfaces and the saturation level of the helical excursion of the magnetic axis. These factors mutually tend to maintain smaller $k_{\|}$ around the radially localized accumulation point; additionally for higher δ_H the frequency accumulation point becomes radially extended as seen in figure 7.16. As mentioned earlier, under these conditions the frequency shifting phenomenon and prominence of the non-axisymmetric sidebands undergo the radial transition of the

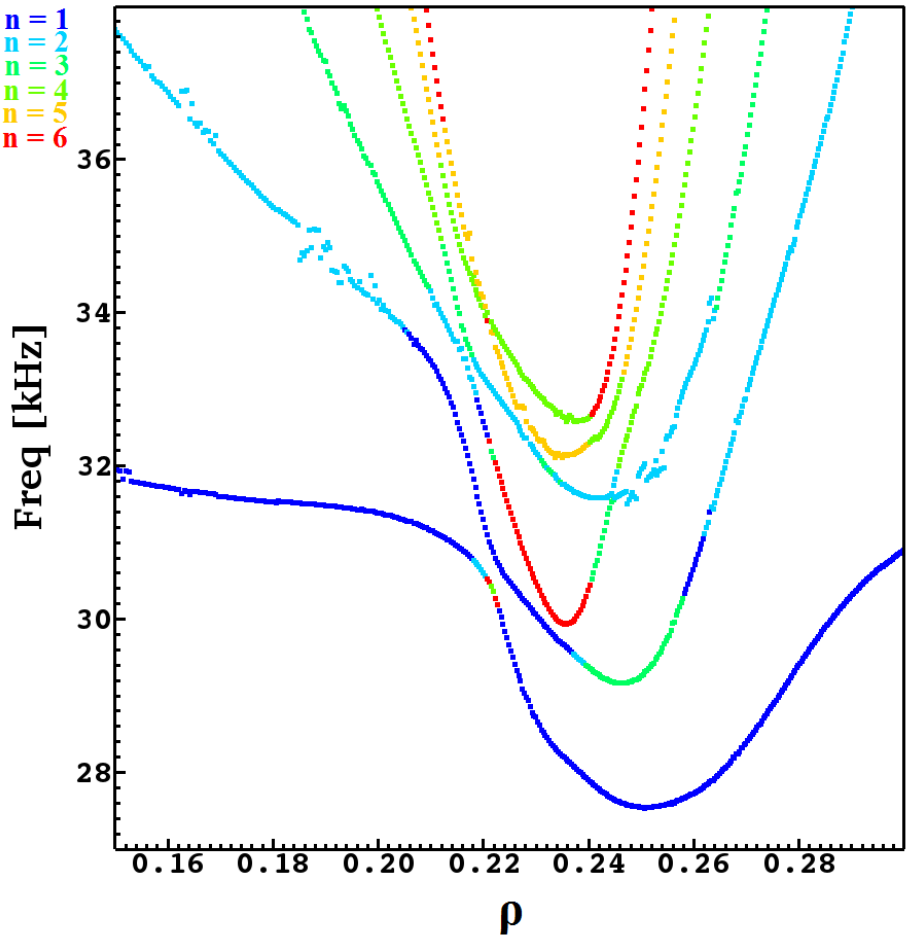

Fig. 7.16 Zoom of Alfvén continua in Figure 7.15. Different colors represent the corresponding toroidal modes number (n)

modes which leads to the coexistence of modes over a wide radial extent since the accumulation point at stronger δ_H gets stretched in radius. The successive transition of the modes happens as shown in figure 7.16, in the mode n = 2 branch which converts into a n = 1 mode in the range $0.205 \leq \rho \leq 0.236$, and beyond $\rho \approx 0.236$ it again changes into an n = 3 mode. Later it transforms back to n = 1 and finally reverts back to n = 2. These successive transitions of the mode can be due to the radial extension of the frequency accumulation point at the stronger helical core ($\delta_H = 0.7$), as they are not present for the lower helical excursion of ($\delta_H = 0.37$) as shown in figure 7.14.

The dependence of frequency splitting around $\rho \approx 0.23$ on the helical core size is shown in Figure 7.17. It shows that splitting in frequency (Δf) increases with the helical core size. It is very low, around 0.5 kHz for small $\delta_H = 0.22$ values and reaches 5 kHz for the maximum helical core size of $\delta_H = 0.7$.

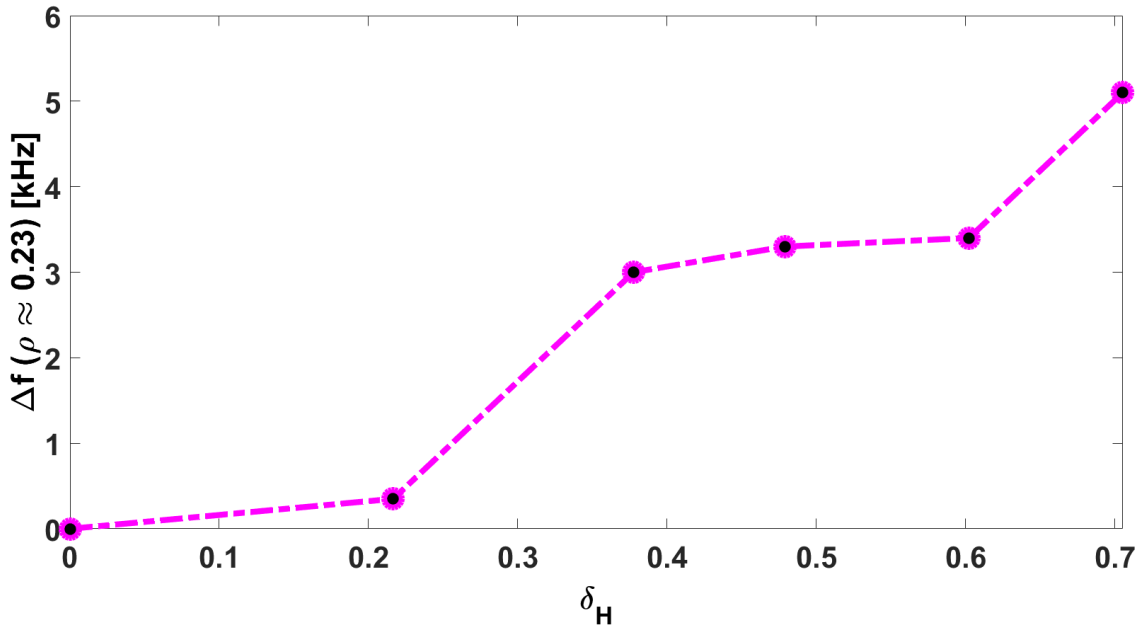

Fig. 7.17 Alfvén continuum frequency splitting with helical core size around $\rho \approx 0.23$ when toroidal mode numbers n = 1 - 6 have been taken into account in the calculations. If a larger number of n's had been included in the calculations, the Δf could have been different.

Around the frequency splitting accumulation point, the radial variation of the Alfvén continuum extrema remains unchanged at the lower values of the helical core size δ_H as shown in Figure 7.18. However a small increase of $\rho = 0.025$ has been noticed, which suggests that frequency splitting appears with a very small radial excursion of continua. For the maximum achieved helical core excursion ($\delta_H = 0.7$), a small difference of $\rho = 0.016$ between the continua minimum and maximum frequencies shows that the frequency splitting is accompanied with a small movement of the accumulation point in radius.

Alfvén continuum calculations for the different levels of the helical core equilibria have been performed. The dependence of the Alfvén frequency gaps on δ_H, formed by the extrema of n = 6 continua with helical equilibria, around the plasma axis and at two further out radial locations is shown in Figure 7.19. Alfvén gaps at these three ρ values show a decreasing tendency for further increases in helical core strength beyond $\delta_H = 0.37$. Around the plasma axis ($\rho \approx 0$), the continuum gaps are narrower than the gaps around $\rho \approx 0.23$ and wider than the gaps $\rho \approx 0.35$. Alfvén gaps for $\rho \approx 0$ at $\delta_H = 0$ and $\delta_H = 0.37$ are comparable having around 280 kHz frequency and for the maximum helical excursion $\delta_H = 0.7$, the gap is 255 kHz.

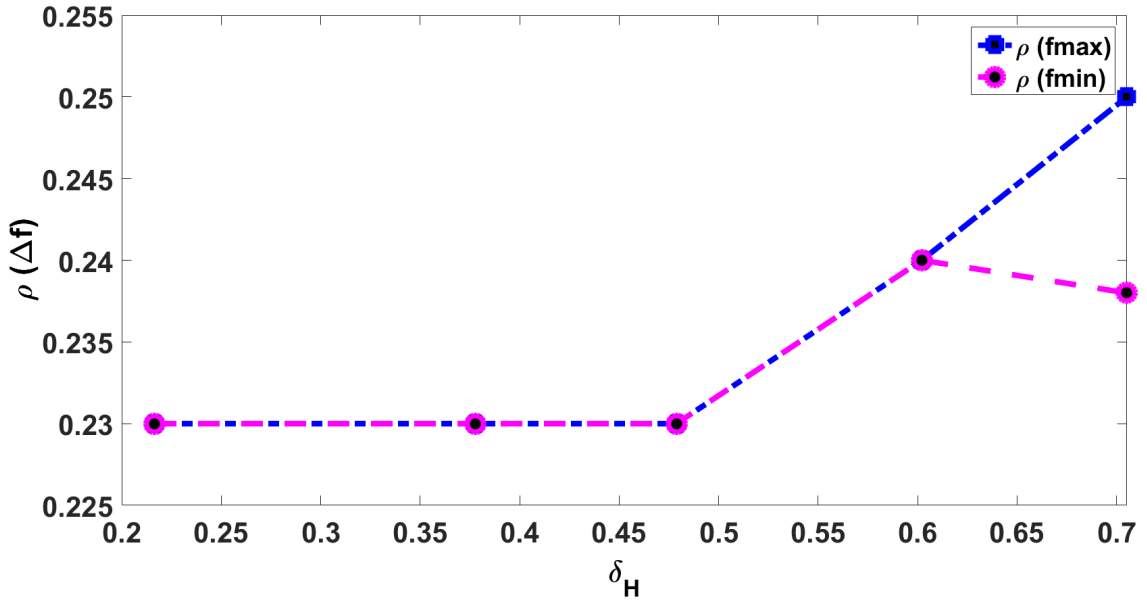

Fig. 7.18 Radial variation of the frequency splitting accumulation point with helical core excursion

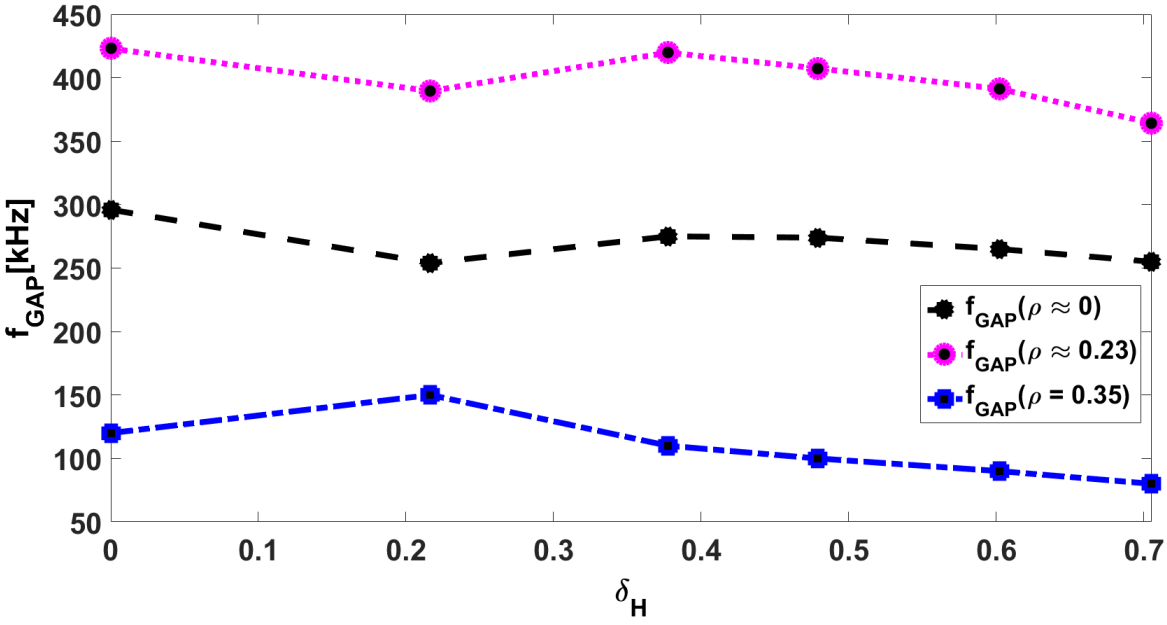

Fig. 7.19 Alfvén frequency gap variation with the helical core size at three different radial locations

At the frequency splitting radial location $\rho \approx 0.23$, the Alfvén gap is larger for the axisymmetric case ($\delta_H = 0$) having a frequency of 420 kHz as compared with the increasing values of δ_H. The Alfvén gap around $\rho \approx 0.23$ decreases with an increase

in $\delta_H = 0.37$ to 0.7 and reaches to 365 kHz for largest helical core size. However for $\delta_H = 0.22$ the gap is relatively smaller. It is also noticeable that at $\rho \approx 0.23$, the continuum gaps at $\delta_H = 0$ and $\delta_H = 0.37$ are comparable. The decrease in the Alfvén frequency gap has been encountered for higher values of ρ, at the radial location $\rho \approx 0.35$ the frequency gap decreases around in the range of 126 kHz for the axisymmetric case. Contrary to the gap around $\rho \approx 0.23$, the Alfvén gap around $\rho \approx 0.35$ follows a decreasing trend from $\delta_H = 0.22$ to 0.7 and reaches to 80 kHz for the maximum helical core size $\delta_H = 0.7$. In this case it is also noticeable, the Alfvén gaps at $\delta_H = 0$ and $\delta_H = 0.37$ are not alike as they were in the case of $\rho \approx 0.23$. The lower maxima of continuum structures for the formation of these gaps remained constant around 190 kHz except for $\delta_H = 0.22$ at which it decreased to 160 kHz. The gaps calculated at $\delta_H = 0.22$ correspond to the twice the experimental plasma pressure. The increased plasma pressured decreases helical core excursion and hence the Alfvén gaps at all three radial locations. These results show that the Alfvén frequency gap is strongly influenced by the helical core size and also varies along the minor radius. Close to the plasma axis $\rho \approx 0$, the gap is smaller than at $\rho \approx 0.23$ and as ρ increases from $\rho \approx 0.23$ to 0.4 the Alfvén frequency gap also decreases as shown in Figures 7.11, 7.13 and 7.15.

In these results, three major gaps have been found as characterized by their frequencies. In low frequency region the gap is identified with the BAE gap which is generated by the plasma compressibility and geodesic curvature. In between the two identical toroidal mode numbers, a wider gap has been found due to the adjacent poloidal mode couplings, therefore it is called TAE gap. At relative farther radial location and higher frequency a gap also forms, which is identified as the EAE gap. These results show that the TAE gap is the largest gap and has its maximum value around the frequency accumulations point $\rho \approx 0.23$ and it decreases at the outer radii. Thus it is expected that not only the BAE physics is modified but also the TAE (odd and even) and EAE mode frequencies which will be investigated elsewhere.

In comparison with 2D results given in Figures 7.11 and 7.12, a distortion in the continuum structures δf_{AC} around $\rho \approx 0.35$ has been noticed (Figures 7.13 and 7.15), which appears only when the helical core 3D equilibrium is employed. We have inferred δf_{AC} as conversion of the mode from one toroidal mode number to another; this generates localised gaps between the different continuum spectra along the radius starting from $\rho \approx 0.35$. Distortion in the Alfvén continuum provides an information about the formation of the localised gaps between different continua and the mode conversion which are absent in the axisymmetric calculations.

The maximum radial extent to which the effect of δf_{AC} is modelled with the helical excursion δ_H is shown in figure 7.20. This shows, for smaller helical core ($\delta_H = 0.22$), the distortion in continua ranges up to $\rho \approx 0.42$ staring from $\rho \approx 0.35$ and it reaches up to $\rho \approx 0.56$ (figure 7.15) for the maximum achieved helical core size. It generates localised frequency gaps in radius between the different branches of continua. These are Helical Alfvén Eigenmode (HAE) gaps since they emerge due to the coupling of continuum branches from different n's. Up to $\delta_H = 0.7$, the radial extension around $0.35 \leq \rho \leq 0.56$ of the HAE gaps between different continua suggests that they are radially extended modes. At $\delta_H = 0.7$, radially localized closed HAE gaps also appear around $\rho \approx 0.56$.

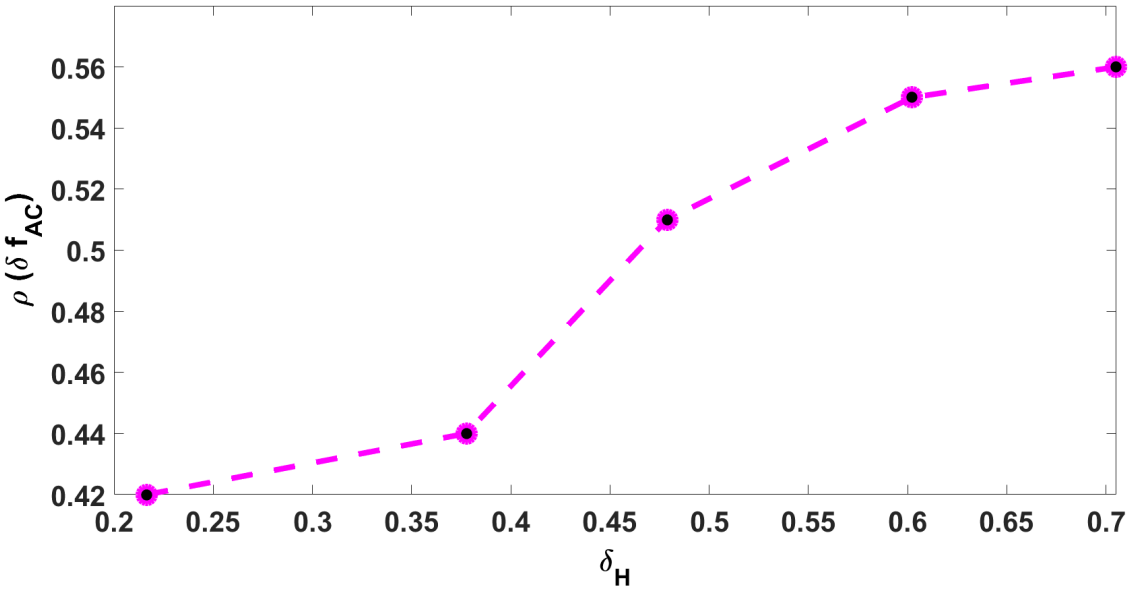

Fig. 7.20 Variation in the radial extent of the Alfvén continuum distortion with helical core size

As per HAE definition [36], n couples to $n \pm \delta_n N_{fp}$ and m with $m \pm \delta_m$, where n and m are toroidal and poloidal mode numbers, N_{fp} is field period and δ_n, δ_m are integer mode displacements, therefore the coupling between successive n's is possible; this leads to open gaps between different n continua. In our calculations, for a significant helical excursion of $\delta_H = 0.7$, initially an $n = 6$ mode (in red) converts to $n = 5$ (yellow) and then $n = 4$ (green) and generates a radially extended gap with the internal mode $n = 5$ frequency (yellow) which then converts to $n = 6$ (red), following to $n = 4$ (green) and back to $n = 5$ as function of radius. These gaps are limited in radial extent associated with the radial extension of $q = 1$ rational surfaces as shown in figure 7.3.

Effects of the 3D density inhomogeneities on the Alfvén spectrum for tokamak plasmas [104] lead to the coupling of different n Alfvén continuum is possible. Specifically, when the toroidal inhomogeneity is prominent these couplings produce new gaps where the continua of the two toroidal harmonics were degenerate in the homogeneous case. Similarly, for in helical equilibria the continuum spectrum is distorted, with the generation of additional gaps caused by the coupling of successive n in radius.

This splitting of Alfvén continua with helical core size is helpful to explain the experimental observations: first one has to note that lower mode numbers have lower accumulation points for the acoustic-Alfvén modes (see e.g. fig 13 of [96]). However, the BAE modes observed in the experiment show the inversion of the mode numbers from the kinetic simulations [95]. Towards the end of the sawtooth cycle the splitting of the modes remains in the model whereas it disappears experimentally (see t = 1.98 of fig 7 in reference [96]). Before the crash, the core pressure is at its maximum, and despite some sawtooth precursors it remains large in the last 10 ms before the crash. The modification of the BAE accumulation points due to the helical core suggest that the splitting should decrease since it cancels the 'inverse diamagnetic' splitting discussed in reference [96]. In addition, also a small radial shift of the BAE accumulation point due the helical core is observed (see fig. 16 [96]), changing the kinetic BAE accumulation point because of radial profile (mainly T_i and T_e) effects. Thus, the combination of helical core ($\sim$ 3-5kHz shift) and diamagnetic downshift may go hand in hand to explain the experimental observations. Very demanding global kinetic 3D calculations would be needed to investigate this question more quantitatively.

7.6 Summary and conclusions

Investigations for the Alfvén continuum spectra of helically distorted MHD equilibrium have been carried out for improved understanding of observed low-frequency Alfvénic modes in tokamak plasmas. First, we have carried out the bifurcated MHD equilibrium investigations for the tokamak plasmas using a 3D numerical tool (VMEC). Identical sets of parameters have been employed in the reconstructions of axisymmetric (2D) and helical core (3D) equilibria, with the only difference being a small seed perturbation in the magnetic axis. The formation of the helical core has been associated with a saturated internal-kink m = 1, n = 1 mode [93] which determines its excursion level. In previous studies [96], a kinetic model has been applied to the experimental findings. We find that near rational surfaces having q = 1, the Alfvén continuum splits into multiple frequencies and the continuum of n couples with that of n-1. However,

despite the promising results, the kinetic model [96] alone could not well describe the remaining differences of the 2 to 5 kHz in the frequency splitting. Results for the Alfvén continuum calculations obtained with the extended STELLGAP solver including the 3D effects of helical core equilibria, explain these few kHz differences in the frequency splitting, and confirm the frequency splitting phenomenon around q = 1 rational surfaces. The continua obtained with gaps opened by the plasma compressibility and geodesic curvature are in the range of frequencies of Alfvénic (BAE) and mixed acoustic-Alfvénic (BAAE) modes, which support the experimental findings of low-frequency modes.

The sensitivity studies with pressure variation show that the helical excursion of the equilibrium increases with increasing plasma pressure and eventually it drops at extreme pressures due to the fixed boundary equilibrium calculations. Fixed boundary reconstruction has been considered sufficient in these calculations because of the desired plasma pressure scaling. The continuum results show that the frequency splitting around the accumulation point also increases with increases in the helical excursion. The accumulation point does not vary in radius with the plasma pressure. The distortion in the continua along the radial extent starting from $\rho \approx 0.35$ has been found, which is also an effect from the helical core equilibria.

Finally, it is concluded that these new results are comparable with the experimental findings discussed in [96], with the confirmation of frequency splitting in Alfvén continuum via coupling of adjacent n continua around an accumulation point. Additionally, the issue of few kHz differences in the frequency splitting is addressed and explained by including 3D effects. Furthermore, the formation of additional low-frequency gaps due to the coupling of acoustic-Alfvén waves are also addressed in our calculations.

Chapter 8

Conclusions and perspectives

8.1 Summary and conclusions

In this thesis, the shear Alfvén continua and discrete Alfvén eigenmodes (AEs) on three dimensional (3D) equilibria have been modelled using 3D numerical tools for the tokamak and stellarator plasmas. Modelling of the steady and chirping AEs, Alfvén cascade modes and the continuum calculations with the helical perturbation of the magnetic axis are the main research areas in this thesis. Comparison of the modelling results obtained using reduced MHD formulation [36, 37] with experimental findings not only benchmark these numerical results but also provide grounds for the concrete solutions of the problems in burning plasmas.

After theoretical description of shear Alfvén waves and mathematical models/tools, in chapter 4 we have modelled the coexistence of the chirping and steady AEs in the TJ-II geometry with dynamic discharges [47]. Fixed boundary equilibria reconstruction have been computed using a 3D equilibrium solver [31] using experimental plasma parameters and with appropriate rotational transform profiles for the iota rising (IR) and lowering (IL) dynamic discharges. In the IR case, we found two prominent modes (m = 8, n = 13) and (m = 10, n = 17) for both chirping and steady types of the modes with decrease in frequency from chirping to steady transition and radially inward localization of the steady modes. Similarly in the IL case, there also are two prominent modes (m = 9, n = 15) and (m = 11, n = 19) with decrease in frequency from chirping to steady states and more inward radial localization of the steady modes. These results suggest that the steady modes are more inward radially localized and their frequencies are relatively lower than the coexisting chirping modes. These modelling results are comparable to the experimental findings.

In chapter 5, for the first time we have modelled the Alfvén cascade modes for the TJ-II plasmas [56, 57] in which frequency-sweeping Alfvén modes were observed experimentally [6] using three different types of the rotational transform profiles i.e. normal, radially extended low shear non-monotonic (NM), strong shear NM iota profiles each having on-axis iota $\iota(0) = 1.5$. In these calculations radially extended GAE and localized RSAEs are identified. For the normal and radially extended low shear NM iota profiles, two similar core localized modes (m = 7, n = 10) and (m = 9, n = 14) appear with discrete frequencies. The frequency range of the modes calculated using low shear NM iota profile covers from 135 to 150 kHz and is relatively larger than the normal iota profile for which these modes are centred around 150 kHz. This shows the results obtained using low shear NM iota profile explain better the frequency sweeping experimental observations. Results obtained through this modelling, with additional low-shear identical NM iota profiles obtained by slight variation in on-axis iota values, also observe similar frequency range from 115 to 295 kHz. An identical mode (m = 7, n = 10/11) appears in the calculations with relatively strong shear NM iota profiles with varying ι_{min} radially localized around the ι_{min} radial position. Frequencies obtained 3D modelling tools are consistent with the frequencies calculated using an analytical dispersion relation. This mode's consistency with similar NM iota profiles offers an opportunity to model the ι_{min}. These calculations support the development of MHD spectroscopy as a sensitive iota profile diagnostic technique for the future fusion devices where other methods may not be practical due to high neutron flux.

The modes obtained in these calculations have global structures and therefore can be considered to impact the fast ion confinement and hence their heating efficiency. In modes analysis some cases show modulational effects of multiple competing Alfvén modes having discrete frequencies. Modes with lower frequency and radially extended global structures are characterized as GAEs and radially localized ones with relatively higher frequency as RSAEs.

In chapter 6, we have modelled the resonant wave-particle interaction (WPI) for the TJ-II plasmas using Monte Carlo transport model i.e. DELTA5D code [70, 71]. In this model the enhanced energy transfer between wave and particles is implemented. In our calculations we consider one modelled mode with $n = 11$ and varying bounce harmonic p having frequency 306.57 kHz to model the resonant condition. In our simulations we find that if the energetic ion beam is launched relatively more outward radially i.e. at higher ρ values then the 2D matrices for poloidal and toroidal frequencies of the drift orbits allow an expansion in the area of unconfined beam ions, effectively pushing the phase space area of confined beam ions down to lower energies. Using

the calculated poloidal orbit frequency and the toroidal precession frequency, one can compute resonance function by combining their 2D functions in Equation (6.1) for various integer values of p and for the frequency and toroidal mode number of the AE of interest. In these calculations the corresponding wave-particle resonance maps suggest for low bounce harmonics (p) the possibility of describing the nonlinear evolution of the AEs in TJ-II by a sum of two ion populations with different weighting factors, one of which is dominated by drag and the other by diffusion. As the bounce harmonic increases, the resonance region starts to expand and can cover a significant area of the particle phase space until this resonance region vanishes at high bounce harmonics. The modelled orbits from each of the drag and diffusion sections of the resonance function are identical in TJ-II stellarator and are compatible with the previous orbit calculations [76].

In chapter 7, we have modelled for the first time the observed low-frequency Alfvén instabilities with the helical core formation in ASDEX Upgrade (AUG) tokamak plasmas [80]. Initially we reconstructed bifurcated MHD equilibrium for the tokamak plasmas using a 3D numerical tool (VMEC) as a prerequisite for the further calculations. The bifurcation of MHD equilibrium due to the saturation of the magnetic axis quantitatively identical to the saturated internal-kink (m = 1, n = 1) mode leads to the formation of 3D helical structures along with the axisymmetric boundary. Reconstruction of the bifurcated 3D helical core equilibria serves as perturbation which affects the Alfvén continuum structures. Previously, a kinetic model [99] was applied to such observations [96], despite of finding the Alfvén continuum splitting this model could not describe the differences of few kHz in such frequency splitting. We have again confirmed these frequency splitting with the helical core equilibria using an extended version of the Alfvén continuum solver (STELLGAP) [45] around q = 1 rational surfaces. The obtained continua with gaps opened by the plasma compressibility and geodesic curvature are in the range of frequencies of Alfvénic (BAE) and mixed acoustic-Alfvénic (BAAE) modes, which support the experimental findings of low-frequency modes.

Pressure sensitivity scan suggests the increase in helical excursion with the increase of plasma pressure, at higher pressures the helical excursion decreases because of the fixed boundary equilibrium calculations. Here, the fixed boundary equilibrium reconstruction has been considered sufficient because of the observed plasma pressure. It is also worth to notice that continuum splitting around the frequency accumulation point also increases with the increase in the helical core size. These results are comparable with the experimental findings as discussed in [96], with the confirmation of frequency splitting in Alfvén continuum around an accumulation point. Additionally,

the formation of low-frequency gaps due to the coupling of acoustic-Alfvén waves is also compatible with the experimentally observed BAEs.

8.2 Future perspectives

Despite the comprehensive modelling analysis of the Alfvénic instabilities in TJ-II flexible heliac in dynamic plasmas, there are still possibilities to extend such modelling efforts to build a comprehensive understanding of coherent MHD instabilities in 3D fusion plasmas. Here few of the important areas are highlighted for the consideration of the next-step modelling.

Modelling of Alfvénic instabilities driven by energetic ions using their practical distribution functions is an active field of research in many fusion devices, therefore investigations utilizing different possible fast ions distribution would add to understand the drive and impact in such 3D systems. There is possibility of investigating these instabilities with the interaction of energetic particles by calculating their growth rates, amplitudes and three dimensional mode structures. Further investigations for the mode structures are possible for the low-frequency modes with the use of Alfvénic-acoustic coupling model in the AE3D code.

These numerical tools can be upgraded by introducing an interaction of energetic particle with Alfvén instabilities. The drive of these modes due to the interaction of fast ions with the iota profile and plasma parameters is an important aspect to be evaluated. Calculation of the modes growth rate on the account of fast ions distribution would enhance the applicability of these numerical tools in 3D toroidal devices. While calculating the modes structures and their prominent mode numbers, AE3D code can be upgraded by introducing the low-frequency sound-wave coupling with the Alfvén waves, which can help to investigate the acoustic (BAE) and Alfvén-acoustic (BAAE) modes structures and their growth rates at lower frequency range.

Investigations using free-boundary equilibrium both in stellarator and tokamak plasmas would be an interesting opportunity to find the effect of relaxing last closed flux surface (LCFS) on these instabilities. It is possible that the free-boundary calculations would allow the continuum gaps to extend relatively beyond the plasma column and would track the saturation levels of the Alfveénic modes. In the case of helical core formation, free-boundary equilibrium calculations would allow to extend the plasma pressure scaling and its effect on the helical core excursion. This will then allow to model Alfvén modes for scaled plasma pressure and extended helical core excursion, which will in return provide pressure scaling in such plasmas.

Such investigations can also be extended for the introduction of the magnetic islands in fusion devices due to the formation of magnetic stochastic regions in the MHD equilibrium. The investigations of the island induced Alfvén (IAEs) modes have not been considered in this thesis, which can also be considered in the future outlook.

In the wave-particle interaction (WPI), it would be interesting to investigate whether the iota variation in TJ-II experiments could affect the proportion of the resonant beam particles between the two different areas of the computed resonance function i.e. drag-dominated region and diffusion-dominated region to see if the scenario observed in [79] is reproduced.

References

[1] M. Hölzl. *PhD Thesis*. Max-Planck-Institut für Plasmaphysik, München, 2010.

[2] S.E. Sharapov. Toroidal alfvén eigenmodes and fast particles in tokamaks. *Transactions of Fusion Science and Technology*, 61:104, 2012.

[3] T.B. Fehér. *Simulation of the interaction between Alfvén waves and fast particles*. PhD thesis, Max-Planck-Institut für Plasmaphysik, Greifswald, 2013.

[4] W.W. Heidbrink. Basic physics of alfvén instabilities driven by energetic particles in toroidally confined plasmas. *Physics of Plasmas*, 15:055501, 2008.

[5] A.V. Melnikov et al. Transition from chirping to steady NBI-driven alfvén modes caused by magnetic configuration variations in the TJ-II stellarator. *Nuclear Fusion*, 56:076001, 2016.

[6] A.V. Melnikov et al. Effect of magnetic configuration on frequency of NBI-driven alfvén modes in TJ-II. *Nuclear Fusion*, 54:123002, 2014.

[7] Weston M. Stacey. *Fusion Plasma Physics*. WILEY-VCH Verlag GmbH, Darmstadt, 2005.

[8] J. Freidberg. *Theory of Fusion Plasmas*. Cambridge University Press, New York, 2007.

[9] C. Beidler et al. Chapter 8: Helical confinement concepts. *Fusion Physics, IAEA*, page 847, 2012.

[10] T.J. Dolan. *Fusion Research (Principles, Experiments and Technology)*. Pergamon Press, New York, 2000.

[11] H. Alfvén. 3d field phase-space control in tokamak plasmas. *Nature Physics*, 14:1223, 2018.

[12] N. Nakajima C.Z. Cheng and M. Okamoto. High-n helicity-induced shear alfvén eigenmodes. *Physics of Fluids* ***B****, Plasma Physics*, 4:1115, 1992.

[13] Ya.I. Kolesnichenko et al. Alfvén continuum and high-frequency eigenmodes in optimized stellarators. *Physics of Plasmas*, 8:491, 2001.

[14] S. Yamamoto et al. Observation of helicity-induced alfvén eigenmodes in large-helical-device plasmas heated by neutral-beam injection. *Physics Review Letters*, 91:245001, 2003.

[15] C. Schwab. Ideal magnetohydrodynamics: Global mode analysis of three-dimensional plasma configurations. *Physics of Fluids* ***B****, Plasma Physics*, 5:3195, 1993.

[16] D.A. Spong et al. Simulation of alfvén frequency cascade modes in reversed shear-discharges using a landau-closure model. *Nuclear Fusion*, 53:053008, 2013.

[17] S.E. Sharapov et al. Alfvén wave cascades in a tokamak. *Physics of Plasmas*, 9:2027, 2002.

[18] S.E. Sharapov et al. MHD spectroscopy through detecting toroidal alfvén eigenmodes and alfvén wave cascades. *Physics Letter A*, 289:127, 2001.

[19] A. Fasoli et al. MHD spectroscopy. *Plasma Physics and Controlled Fusion*, 44:B159–B172, 2002.

[20] S.E. Sharapov et al. Alfvén cascades in JET discharges with NBI-heating. *Nuclear Fusion*, 44:S868, 2006.

[21] K. Toi et al. Observation of reversed-shear alfvén eigenmodes excited by energetic ions in a helical plasma. *Physics Review Letters*, 105:145003, 2010.

[22] G.J. Kramer et al. Mitigation of alfvénic activity by 3d magnetic perturbations on NSTX. *Plasma Physics and Controlled Fusion*, 58:085003, 2016.

[23] W.A. Cooper et al. Tokamak magnetohydrodynamic equilibrium states with axisymmetric boundary and a 3D helical core. *Physics Review Letters*, 105:035003, 2010.

[24] W.A. Cooper J.P. Graves and O. Sauter. Jet snake magnetohydrodynamic equilibria. *Nuclear Fusion*, 51:072002, 2011.

[25] H. Alfvén. Existence of electromagnetic-hydrodynamic waves. *Nature*, 150:405, 1942.

[26] K. Miyamoto. *Plasma Physics for Controlled Fusion*. Springer-Verlag GmbH, Berlin Heidelberg, 2016.

[27] Ya.I. Kolesnichenko et al. Affinity and difference between energetic-ion-driven instabilities in 2d and 3d toroidal systems. *Plasma Physics and Controlled Fusion*, 53:024007, 2011.

[28] A. Weller et al. Survey of magnetohydrodynamic instabilities in the advanced stellarator wendelstein 7-AS. *Phys. Plasmas*, 8:931, 2001.

[29] R. Jiménez-Gómez et al. Alfvén eigenmodes measured in the tj-ii stellarator. *Nuclear Fusion*, 51:033001, 2011.

[30] S.E. Kruger C.C. Hegna and J.D. Callen. Generalized reduced magnetohydrodynamic equations. *Physics of Plasmas*, 5:4169, 1998.

[31] S.P. Hirshman and J.C. Whitson. Steepest-descent moment method for three-dimensional magnetohydrodynamic equilibria. *Phys. Fluids*, 26:3553, 1983.

[32] S.P. Hirshman and H.K. Meier. Optimized fourier representations for three-dimensional magnetic surfaces. *Phys. Fluids*, 28:1387, 1985.

[33] W.A. Cooper et al. Magnetohydrodynamic properties of nominally axisymmetric systems with 3D helical core. *Plasma Physics and Controlled Fusion*, 53:074008, 2011.

[34] E. Strumberger S. Günter and C. Tichmann. MHD instabilities in 3D tokamaks. *Nuclear Fusion*, 54:064019, 2014.

[35] W.A. Cooper J.P. Graves and O. Sauter. Helical ITER hybrid scenario equilibria. *Plasma Physics and Controlled Fusion*, 53:024002, 2011.

[36] D.A. Spong R. Sanchez and A. Weller. Shear alfvén continua in stellarators. *Physics of Plasmas*, 10:3217, 2003.

[37] D.A. Spong E. D'Azevedo and Y. Todo. Clustered frequency analysis of shear alfvén modes in stellarators. *Physics of Plasmas*, 17:022106, 2010.

[38] A. Salat and J.A. Tataronis. Shear alfvén mode resonances in nonaxisymmetric toroidal low-pressure plasmas. ii. singular modes in the shear alfvén continuum. *Physics of Plasmas*, 8:1207, 2001.

[39] A.H. Boozer. Plasma equilibrium with rational magnetic surfaces. *Phys. Fluids*, 24:1999, 1981.

[40] A.H. Boozer. Establishment of magnetic coordinates for a given magnetic field. *Phys. Fluids*, 25:520, 1982.

[41] M. Chu et al. A numerical study of the high-n shear alfvén spectrum gap and the high-n gap mode. *Physics of Fluids B*, 4:3713, 1992.

[42] O.P. Fesenyuk Ya.I. Kolesnichenko H. Wobig and Yu.V. Yakovenko. Ideal magnetohydrodynamic equations for low-frequency waves in toroidal plasmas. *Physics of Plasmas*, 9:1589, 2002.

[43] C.Z. Cheng and M.S. Chance. Low-n shear alfvén spectra in axisymmetric toroidal plasmas. *Physics of Fluids B*, 29:3695, 1986.

[44] C.B. Deng et al. Energetic-electron-driven instability in the helically symmetric experiment. *Physics Review Letters*, 103:025003, 2009.

[45] D.A. Spong et al. Energetic-particle-driven instabilities in general toroidal configurations. *Contrib. Plasma Phys*, 50:708, 2010.

[46] G.L.G. Sleijpen and H. A. Van der Vorst. A jacobi-davidson iteration method for linear eigenvalue problems. *SIAM J. Matrix Anal. & Appl.*, 17:401–425, 1996.

[47] A. Rakha et al. Modelling of beam-driven alfvén modes in TJ-II plasmas. *Nuclear Fusion*, 59:056002, 2019.

[48] R. Jiménez-Gómez et al. Alfvén eigenmodes measured in the TJ-II stellarator. *Nuclear Fusion*, 51:033001, 2011.

[49] A. Könies and D. Eremin. Coupling of alfvén and sound waves in stellarator plasmas. *Physics of Plasmas*, 17:012107, 2010.

[50] A. Könies et al. A code for the calculation of kinetic alfvén waves in three-dimensional geometry. *10th IAEA TM on Energetic Particles in Magnetic Confinement Systems*, 2007.

[51] C. R. Cook et al. Identification of island-induced alfvén eigenmodes in a reversed field pinch. *Plasma Physics and Controlled Fusion*, 58:054004, 2016.

[52] K. Toi. Energetic-ion-driven global instabilities observed in the large helical device and their effects on energetic ion confinement. *Plasma and Fusion Research*, 8:1102002, 2013.

[53] A.V. Melnikov et al. Alfvén eigenmode properties and dynamics in the TJ-II stellarator. *Nuclear Fusion*, 52:123004, 2012.

[54] F. Castejón et al. Influence of magnetic well on electromagnetic turbulence in the TJ-II stellarator. *Plasma Physics and Controlled Fusion*, 58:094001, 2016.

[55] A.V. Melnikov et al. Internal measurements of alfvén eigenmodes with heavy ion beam probing in toroidal plasmas. *Nuclear Fusion*, 50:084023, 2010.

[56] A. Rakha et al. Modelling of alfvén cascades in NBI heated stellarator plasmas. *45th EPS Conference on Plasma Physics, Prague, Czech Republic*, 42A:P4.1004, 2018.

[57] A. Rakha et al. Modelling of alfvén cascade modes in stellarator plasmas. *Submitted to Nuclear Fusion*, 2019.

[58] K.L. Wong et al. Alpha-channeling simulation experiment in the DIII-D tokamak. *Physics Review Letters*, 93:085002, 2004.

[59] H.L. Berk et al. Theoretical interpretation of alfvén cascades in tokamaks with nonmonotonic q profiles. *Physics Review Letters*, 87:185002, 2001.

[60] B.N. Breizman et al. Theory of alfvén eigenmodes in shear reversed plasmas. *Physics of Plasmas*, 10:3649, 2003.

[61] M.E. Austin et al. Core barrier formation near integer q surfaces in DIII-D. *Physics of Plasmas*, 13:082502, 2006.

[62] D.A. Spong et al. Verification and validation of linear gyrokinetic simulation of alfvén eigenmodes in the DIII-D tokamak. *Physics of Plasmas*, 19:082511, 2012.

[63] M.A. Van Zeeland et al. Reversed shear alfvén eigenmode stabilization by localized electron cyclotron heating. *Plasma Physics and Controlled Fusion*, 50:035009, 2008.

[64] S.E. Sharapov et al. MHD spectroscopy of JET plasmas with pellets via alfvén eigenmodes. *Nuclear Fusion*, 58:082008, 2018.

[65] K. Toi et al. Energetic-ion-driven global instabilities in stellarator/helical plasmas and comparison with tokamak plasmas. *Plasma Physics and Controlled Fusion*, 53:024008, 2011.

[66] T.E. Evans et al. Direct observation of the structure of global alfvén eigenmodes in a tokamak plasma. *Physics Review Letters*, 53:1743, 1984.

[67] D.A. Spong et al. Global linear gyrokinetic simulation of energetic particle-driven instabilities in the LHD stellarator. *Nuclear Fusion*, 57:086018, 2017.

[68] J.A. Romero et al. Magnetic configuration sweep control in heliac type stellarators. *Nuclear Fusion*, 54:043008, 2014.

[69] Á. Cappa et al. Impact of eccd on alfvén eigenmodes in the tj–ii stellarator. *45th EPS Conference on Plasma Physics, Prague, Czech Republic*, 42A:P4.1012, 2018.

[70] R.H. Fowler J.A. Rome and J.F. Lyon. Monte carlo studies of transport in stellarators. *Phys. Fluids*, 28:338, 1985.

[71] D.A. Spong S.P. Hirshman and J.C. Whitson. Monte carlo studies of transport in stellarators. *Plasma Physics Reports*, 23:483, 1997.

[72] A.H. Boozer and G. Kuo-Petravic. Monte carlo evaluation of transport coefficients. *Phys. Fluids*, 24:851, 1981.

[73] W.A. Cooper et al. Global external ideal magnetohydrodynamic instabilities in three-dimensional plasmas. *Theory of Fusion Plasmas, Proceedings of the Joint Varenna–Lausanne International Workshop, Valla Monastero, Varenna, Italy*, page 655, 1990.

[74] C. Nührenberg. Compressional ideal magnetohydrodynamics: Unstable global modes, stable spectra, and alfvén eigenmodes in wendelstein 7–x-type equilibria. *Physics of Plasmas*, 6:137, 1999.

[75] A. Bustos et al. Kinetic simulations of fast ions in stellarators. *Nuclear Fusion*, 51:083040, 2011.

[76] M. Rodríguez-Pascual et al. Simulations of fast ions distribution in stellarators based on coupled monte carlo fuelling and orbit codes. *Plasma Physics and Controlled Fusion*, 55:085014, 2013.

[77] M.K. Lilley B.N. Breizman and S.E. Sharapov. Destabilizing effect of dynamical friction on fast-particle-driven waves in a near-threshold nonlinear regime. *Physics Review Letters*, 102:195003, 2009.

[78] M.K. Lilley B.N. Breizman and S.E. Sharapov. Effect of dynamical friction on nonlinear energetic particle modes. *Physics of Plasmas*, 17:092305, 2010.

[79] V. Aslanyan S.E. Sharapov D.A. Spong and M. Porkolab. Two species drag/diffusion model for energetic particle driven modes. *Physics of Plasmas*, 24:122511, 2017.

[80] A. Rakha et al. Shear alfvén wave continuum spectrum with bifurcated helical core equilibria. *Accepted in Nuclear Fusion August 2019*, 2019.

[81] L. Chen and F. Zonca. Theory of alfvén waves and energetic particle physics in burning plasmas. *Nuclear Fusion*, 47:S727, 2007.

[82] L. Chen. Theory of magnetohydrodynamic instabilities excited by energetic particles in tokamaks. *Physics of Plasmas*, 1:1519, 1994.

[83] C.Z. Cheng L. Chen and M.S. Chance. High-n ideal and resistive shear alfvén waves in tokamaks. *Annals of Physics*, 161:21, 1985.

[84] A. Hasegawa and L. Chen. Plasma heating by alfvén-wave phase mixing. *Physics Review Letters*, 32:454, 1974.

[85] L. Chen and A. Hasegawa. Plasma heating by spatial resonance of alfvén wave. *Physics of Fluids*, 17:1399, 1974.

[86] A. Biancalani et al. Shear alfvén wave continuous spectrum within magnetic islands. *Physics of Plasmas*, 17:122106, 2010.

[87] R. Lorenzini et al. Self-organized helical equilibria as a new paradigm for ohmically heated fusion plasmas. *Nature Physics*, 5:570, 2009.

[88] W.A. Cooper et al. Bifurcated helical core equilibrium states in tokamaks. *Nuclear Fusion*, 53:073021, 2013.

[89] E. Joffrin et al. The 'hybrid' scenario in JET: towards its validation for ITER. *Nuclear Fusion*, 45:626, 2005.

[90] P.J. Bonofiglo et al. Fast ion transport in the quasi-single helical reversed-field pinch. *Physics of Plasmas*, 26:022502, 2019.

[91] I.T. Chapman et al. Saturated ideal modes in advanced tokamak regimes in MAST. *Nuclear Fusion*, 50:045007, 2010.

[92] D. Pfefferlé et al. Nbi fast ion confinement in the helical core of MAST hybrid-like plasmas. *Nuclear Fusion*, 54:064020, 2014.

[93] E.A. Lazarus et al. A comparison of sawtooth oscillations in bean and oval shaped plasmas. *Plasma Physics and Controlled Fusion*, 48:L65, 2006.

[94] Y. Camenen et al. Current profile tailoring using localized electron cyclotron heating in highly elongated TCV plasmas. *Nuclear Fusion*, 47:586, 2007.

[95] Ph. Lauber et al. Kinetic alfvén eigenmodes at ASDEX upgrade. *Plasma Physics and Controlled Fusion*, 51:124009, 2009.

[96] D. Curran et al. Low-frequency alfvén eigenmodes during the sawtooth cycle at ASDEX upgrade. *Plasma Physics and Controlled Fusion*, 54:055001, 2012.

[97] F. Zonca L. Chen and R.A. Santoro. Kinetic theory of low-frequency alfvén modes in tokamaks. *Plasma Physics and Controlled Fusion*, 38:2011, 1996.

[98] Ph. Lauber. Super-thermal particles in hot plasmas: kinetic models, numerical solution strategies, and comparison to tokamak experiments. *Physics Reports*, 533:33, 2013.

[99] Ph. Lauber et al. LIGKA: a linear gyrokinetic code for the description of background kinetic and fast particle effects on the MHD stability in tokamaks. *Journal of Computational Physics*, 226:447, 2007.

[100] O.P. Fesenyuk Ya.I. Kolesnichenko H. Wobig and Yu.V. Yakovenko. Reduced MHD equations for alfvén eigenmodes in stellarators. *International Workshop "Innovative Concepts and Theory of Stellarators", Kyiv, Ukraine*, ISSN 1606-6723:105, 2001.

[101] Ph. Lauber et al. NBI-driven alfvénic modes at ASDEX upgrade. *Nuclear Fusion*, 52:094007, 2012.

[102] A. Wingen et al. Use of reconstructed 3d equilibria to determine onset conditions of helical cores in tokamaks for extrapolation to ITER. *Nuclear Fusion*, 58:036004, 2018.

[103] T. Kobuchi et al. Magnetic configuration dependence of the shafranov shift in the large helical device. *Plasma Physics and Controlled Fusion*, 48:789, 2006.

[104] H.J.C Oliver et al. Modification of the alfvén spectrum by 3d density inhomogeneities. *45th EPS Conference on Plasma Physics, Prague, Czech Republic*, 42A:P2.1056, 2018.